NASA-CR-172,284

NASA-CR-172284
19840011679

NASA Contractor Report CR-172284

TURBULENT TRANSPORT MODELS FOR SCRAMJET FLOWFIELDS

Final Report

M. M. Sindir and P. T. Harsha

CONTRACT NAS1-15988

FEBRUARY 1984

National Aeronautics and
Space Administration

Langley Research Center
Hampton, Virginia 23665

```
ENTER:
 24      1       1 RN/NASA-CR-172284
          DISPLAY 24/6/1
      84N19747*#   ISSUE 10   PAGE 1491   CATEGORY 34   RPT#: NASA-CR-172284 NAS
      1.26:172284   CNT#: NAS1-15988   84/02/00  91 PAGES   UNCLASSIFIED
      DOCUMENT
UTTL: Turbulent transport models for scramjet flowfields   TLSP: Final Report
AUTH: A/SINDIR, M. M.;  B/HARSHA, P. T.
CORP: Science Applications, Inc., Chatsworth, Calif.   CSS: (Combustion Science
      and Advanced Technology Dept.)    AVAIL.NTIS   SAP: HC A05/MF A01
MAJS: /*FLOW DISTRIBUTION/*SUPERSONIC COMBUSTION RAMJET ENGINES/*TRANSPORT
      PROPERTIES/*TURBULENT MIXING
MINS: / NUMERICAL ANALYSIS/ RECIRCULATIVE FLUID FLOW/ SWIRLING
ABA:  Author
```

1-094-00-809-80
SAI 8401 CHA

TURBULENT TRANSPORT MODELS
FOR
SCRAMJET FLOWFIELDS

Final Report

M.M. Sindir and P.T. Harsha
SCIENCE APPLICATIONS, INC.
Combustion Science and Advanced Technology Department
9760 Owensmouth Avenue
Chatsworth, California 91311

Prepared for:

NATIONAL AERONAUTICS AND SPACE ADMINISTRATION
Langley Research Center
Hampton, Virginia 23665

Under Contract NAS1-15988

February 1984

N84-19747#

TABLE OF CONTENTS

TABLE OF CONTENTS (Continued)

1.0 INTRODUCTION

In order to provide turbulence models useful for computations of the flowfields involved in advanced scramjet combustion systems, a number of features of these flowfields must be considered. These combustion systems involve supersonic flows with embedded subsonic regions and recirculation zones, and appropriate turbulence models for scramjet applications must address each of these. The geometry of advanced combustors is often three-dimensional, so that the effects of three-dimensionality in the flowfield on the turbulence characteristics must be taken into account. Moreover, the combustion process in a scramjet system is embedded within a highly turbulent flow, so that the effects of turbulence on chemical reaction rates must be considered; particularly, in the scramjet context, with respect to ignition phenomena. On the other hand, to be of maximum utility in scramjet combustor design, the turbulence modeling should be as simple and straightforward as is consistent with the requirements of overall accuracy. In this application, predictions of mean flowfield structure, the effects of heat release, and mean chemical reaction rates are of greatest importance: details of the turbulence structure itself can be approximated if the approximations introduced do not materially affect the prediction of overall mixing rate, chemical reaction rate, and parameters such as the wall skin friction distribution and flowfield pressure gradient. Since it can be expected that different effects may dominate in different regions of the flow: nonisotropy in recirculation regions; compressibility effects in high speed flow regions; and turbulence-chemistry interaction effects in regions in which fuel ignition is occurring, a modular approach may be the most efficient turbulence model overall. In such an approach, each module contains the turbulence model elements which best account for the dominant features of each region of the flowfield.

An assessment of turbulence models for scramjet applications was initiated in September 1979. During the first year of this work, as outlined in Ref. 1, the major effort involved the examination of the multiple dissipation length scale (MDLS) turbulence model, since this approach appeared to offer the potential for greater generality than existing models in the context of scramjet-related flowfields. In addition to this work, other efforts carried out during the first year of this program included the definition of a technique for the estimation of the initial conditions required by field-equation turbulence models (Ref. 1), an examination of the use of a modified dissipation rate equation with the basic k-ε two-equation turbulence model, and the development of a supersonic-flow compressibility correction to the dissipation rate equation in the two-equation (or MDLS) approach.

Although the results of Ref. 1 indicated that the MDLS model is slightly more general than the basic k-ε model, the gain did not appear worth the added cost of solving two additional equations. Furthermore, the flowfields considered in the analyses reported in Ref. 1, while fundamental to and underlying many of the structures found in scramjet flows, did not involve large scale recirculation regions. Accordingly, the focus of the second year's work shifted to an assessment of the performance of a variety of turbulence models in low-speed and high-speed recirculating flows. This work, described in Ref. 2, involved the application of several turbulence models to a variety of recirculating flows including axisymmetric and planar sudden-expansions. The turbulence mdoels studied included the basic two-equation model and the algebraic stress model, in both cases with and without modifications to the dissipation rate equation designed to enhance the model's sensitivity to streamline curvature. Results of this work indicated that the algebraic stress model was the most generally applicable in regions of strong recirculation, and that the modification to the dissipation rate equation, while important in the region surrounding the recirculation zone, had a deleterious effect on the overall level of predictions in the region downstream of the recirculation zone. On the other hand, the results described in Ref. 2 were felt to be inconclusive, since only in planar subsonic recirculating flows could clear model differences be discerned.

A further observation made in the course of carrying out the work described in Ref. 2 was that in complex flowfields it is difficult to separate some aspects of the turbulence modeling problem from the numerical problems inherent in different computational approaches for solving the governing equations describing the flow. These aspects include the treatment of wall boundary conditions, the algorithms used to generate the finite-difference form of the equations, and the algorithms used to provide the finite-difference solution of the governing equations for the particular turbulence model chosen. While not an integral part of the work plan for the program, several such problems were encountered and were discussed in Ref. 2. Work in this area continued during the program described in this document, with particular emphasis on the minimization of numerical diffusion problems in turbulence model assessment.

The work described in this report completes the assessment of turbulence models for scramjet applications. Axisymmetric subsonic recirculating flows were considered to complete the k-ε model and ASM model comparisons initiated in the prior program. Swirling flows, while not themselves of direct interest in scramjet applications, were found to be stringent tests of turbulence modeling so that assessment of the various turbulence models was extended to these flowfields. Considerable care was taken to minimize the effects of numerical diffusion which, if not carefully minimized, can all but swamp differences between turbulence models. Further efforts to incorporate higher-order turbulence models in both the time-split and time-unsplit MacCormack predictor-corrector schemes were carried out. These efforts were unsuccessful: the introduction of stiff equations renders the basic solution algorithm unstable, and this result points up the need for turbulence model development and numerical solution algorithm development to proceed in parallel. Just as there is no completely general turbulence model, neither does a general numerical solution algorithm exist. Finally, methods of modeling scalar transport which do not invoke the Boussinesq gradient diffusion hypothesis were investigated. Each of these areas is described in detail in this work.

Although, as noted above, no completely general turbulence model exists for scramjet applications, the work described in this report and in Refs. 1 and 2 indicates that the algebraic stress formulation is the method of choice. This conclusion results from the greater generality of the approach, compared with the two-equation model, and from its ability, when coupled with appropriate numerical resolution, to model details of the flow such as counter-rotating vortices in a sudden expansion recirculation region. In regions of relatively simple flow (i.e., jets and shear layers) the basic two-equation approach remains applicable, and it is easily arranged to transition from the ASM to the k-ε approach since the turbulence kinetic energy and dissipation rate equations are fundamental parts of the ASM formulation. Finally, solution of the equation for transport of the turbulent species flux, in the same general way as the ASM solution proceeds, appears to be a viable method for generalizing these results to more complex flows with species and energy transport. However, further model development work is required in the latter area, and such model development work is recommended as an outgrowth of the work described in this report.

2.0. ASSESSMENT OF TURBULENCE MODELS FOR SCRAMJET APPLICATIONS

Three major areas were addressed in this phase of the assessment of turbulence models for scramjet applications carried out under this program. These areas included assessment of models for subsonic, axisymmetric, swirling and nonswirling recirculating flows and the development of the k-ε and the algebraic stress model approaches for the prediction of supersonic recirculating flows. The k-ε model relates the Reynolds stresses to the mean rate of strain through the definition of an isotropic turbulent viscosity, whereas the more advanced algebraic stress model calculates the stresses from implicit algebraic relationships containing the stresses themselves, the mean rate of strain, and the turbulent kinetic energy and its dissipation rate. Modified versions of the models employ a new dissipation rate equation whose production term was made more sensitive to streamwise curvature effects. A new nonequilibrium wall-function treatment was also incorporated into each model. These models are discussed in detail in Ref. 2. Swirling flows were investigated because of the demands they place on models with respect to accurate predictions of a wider variety of flowfield features than nonswirling flows and their incorporation of multiple shear stress components. In the area of supersonic recirculating flows, problems of turbulence model application were encountered which highlight the interaction between turbulence modeling and numerical solution techniques.

The assessment of turbulence models for axisymmetric sudden expansion flows reported in Ref. 2 was inconclusive since only one diameter ratio was calculated using a relatively coarse grid. In this year's program a follow-up study covering different diameter ratios and using a finer mesh was conducted as the final step in the assessment of turbulence models in subsonic flows.

Most computational studies to date fail to separate the effects of numerics from the influence of turbulence models in assessing their results. Current literature therefore abounds with discrepancies in the predictions of flowfields with the same turbulence models but different numerical techniques. A preliminary study was conducted to address this problem, considering the following four areas:

1. Selection of test cases
2. Determination of the solution domain length
3. Determination of convergence criteria
4. Reduction of numerical diffusion through grid refinement.

2.1 SELECTION OF TEST CASES

Surprisinly there are very few experimental (or numerical) studies of mean and turbulence flowfields in axisymmetric sudden expansions. The only applicable study that has detailed velocity and turbulence measurements is the Chaturvedi case (Ref. 3). Back and Roschke (Ref. 4) report reattachment length measurements in laminar and low Reynolds number turbulent flows ($R_e \leqslant 4000$ based on inlet diameter) for 2.6:1 diameter ratio sudden expansions. Studgess and Syed (Ref. 5) provide some centerline velocity data, originally obtained by Lipstein and described in a General Electric Co. corporate report only. These data are for diameter ratios of 1.6:1, 2.5:1 and 4:1. Finally, heat and mass transfer measurements in axisymmetric sudden expansions are reported in Refs. 6, 7, and 8. For this work, diameter ratios of 1.33:1, 2:1 and 3:1 were selected as representative values of the range of diameter ratios encountered in practical and research oriented applications. Comparisons with experiments are presented for the 2:1 diameter ratio case.

2.2. DETERMINATION OF THE SOLUTION DOMAIN LENGTH

Specification of the solution domain length is an important consideration in computational work. Too short a length causes the exit boundary condition to affect the rest of the flowfield more strongly than is physically realistic, and an excessively long solution domain results in poor resolution or a waste of grid points. Thus a study was conducted to determine a realistic solution domain length for turbulent axisymmetric sudden expansion flow calculations. For this purpose the 2:1 diameter ratio geometry of Chaturvedi (Ref. 3) was chosen as the test case, using the k-ε turbulence model. This grid refinement study consisted of increasing the length of the solution domain while maintaining a fixed mesh spacing. More nodes were added in the streamwise direction to allow these increases -- a necessary step to exclude effects due to changes in grid spacing. The value at which the reattachment length, the flow parameter chosen to be tested, ceased to vary with further increases was taken as the lower limit for the solution domain length. The results of this study, presented in Figure 2.1a, indicate a value of 11 step heights or more as the recommended length for the k-ε model predictions of this geometry. A solution domain length of sixteen (16) step heights

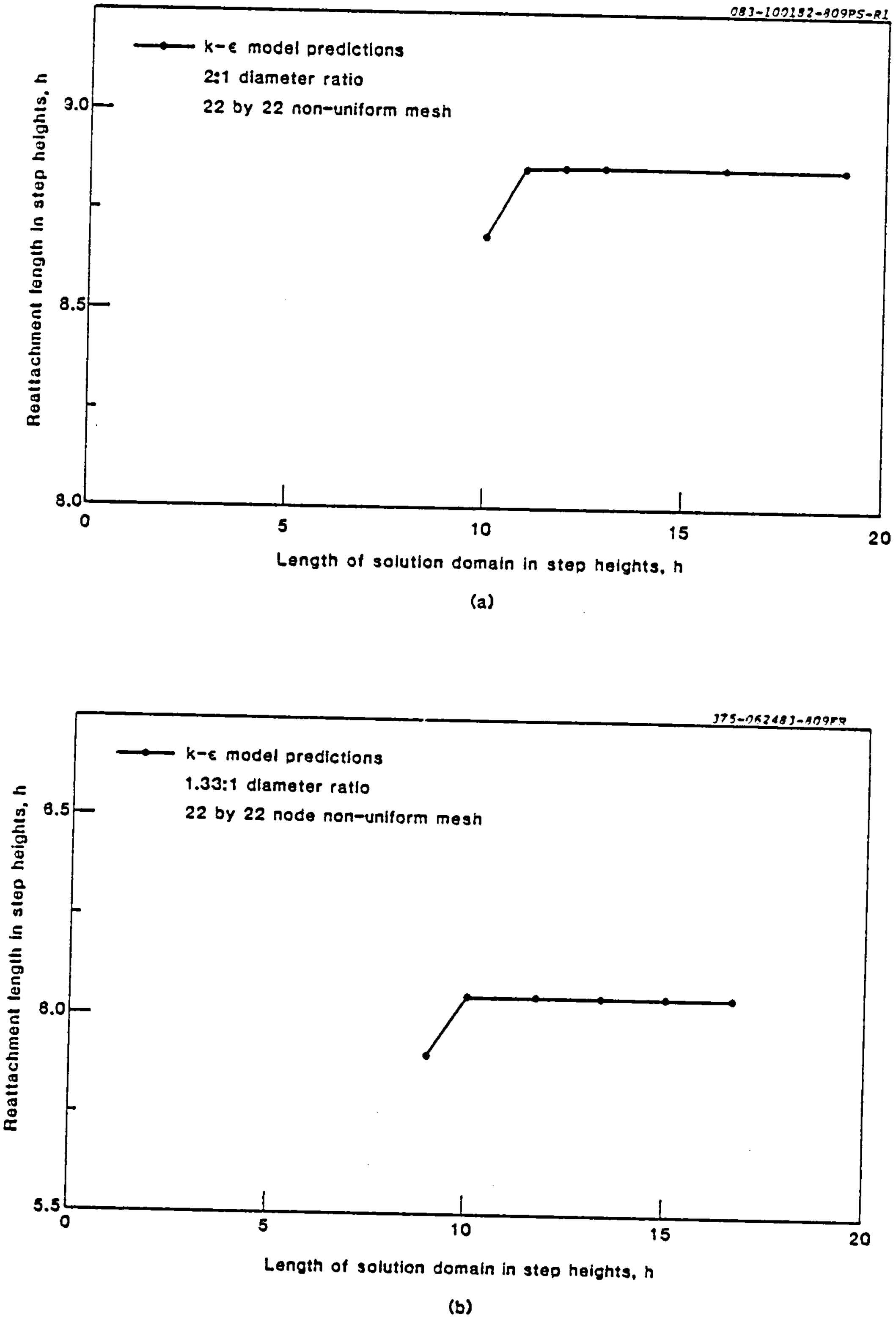

(a)

(b)

Figure 2.1. Variation of reattachment length with length of solution domain.

was adopted for subsequent computations to accommodate anticipated differences in reattachment length predictions for the different turbulence models investigated. Results of a similar study for the 1.33:1 diameter ratio, given in Figure 2.1b, also confirm these observations with respect to solution domain length.

2.3. DETERMINATION OF CONVERGENCE CRITERIA

In iterative codes the convergence criterion is a measure of the degree to which a computed solution satisfies the finite-difference equations. For the STEP family of programs (Ref. 9) this criterion is the level of the residual sources (SORMAX). A study was conducted, again using the k-ε turbulence model, to determine a realistic convergence criterion for the test cases considered in this work. This study was carried out by sequentially decreasing the level of SORMAX until the change in the reattachment length, the flow parameter tested, was less than 1 percent for an order of magnitude reduction in SORMAX. For all three area ratios, a satisfactory convergence criterion was determined to be 0.001.

2.4 REDUCTION OF NUMERICAL DIFFUSION THROUGH GRID REFINEMENT

It is a well-known fact that all upstream or hybrid-upstream* based finite differencing techniques, although computationally very stable, introduce numerical diffusion into the formulation. Unless the effects of this artificial viscosity are removed, the solution thus obtained does not satisfy the governing partial differential equations and can be in serious error. The source of this problem is the truncation error in the one-sided first difference used in upstream differencing

$$-u \frac{\phi_i - \phi_{i-1}}{\Delta x} = -u \left[\left(\frac{\partial \phi}{\partial x}\right)_i - \frac{1}{2} \frac{\partial^2 \phi}{\partial x^2} \Delta x + \mathrm{HOT}\right] \qquad (1)$$

or

$$-u \frac{\phi_{i+1} - \phi_i}{\Delta x} = -u \left[\left(\frac{\partial \phi}{\partial x}\right)_i + \frac{1}{2} \frac{\partial^2 \phi}{\partial x^2} \Delta x + \mathrm{HOT}\right] \qquad (2)$$

Note that the leading-order discretization term is equivalent to a physical diffusion term with an effective diffusion coefficient of

---

*Hybrid upstream finite differencing techniques (currently used in many codes including the STEP family) use upstream differencing for $|Pe_{cell}|>2$ and central differencing for $-2 \leq Pe_{cell} \leq 2$. Pe_{cell} is the cell Peclet number defined in Eq. 4.

$$\Gamma_{\text{Numerical}} = \pm \frac{u\Delta x}{2} \tag{3}$$

This term is one explanation of the stability of upstream differencing techniques. By choosing (1) when $u > 0$ and (2) when $u < 0$, the discretization error terms are always stabilizing. However, they also introduce a numerical diffusivity that may dominate the physical diffusion terms. The appropriate parameter is the cell Peclet number, defined as the ratio of discretized convection terms to discretized diffusion terms

$$Pe_{\text{cell}} = \frac{u\Delta x}{\Gamma} \tag{4}$$

where Γ is the effective (laminar or turbulent) diffusion coefficient. This parameter can also be interpreted as

$$Pe_{\text{cell}} = 2\,\frac{\Gamma_{\text{Numerical}}}{\Gamma} \tag{5}$$

Therefore, when $Pe_{\text{cell}} = 2$, numerical and physical diffusion are of the same size. Computationally, if $Pe_{\text{cell}} \lesssim 1$ the flow is diffusion dominated and the form of finite differencing used in the convection (first derivative) terms does not affect the results. For $|Pe_{\text{cell}}| > 2$, central differencing of the convection terms becomes potentially wiggly, and for convection dominated flows ($|Pe_{\text{cell}}| > 5$), upstream differencing can produce numerical diffusivities that can interfere with and completely dominate physical diffusion terms.

It is usually quite difficult to accurately quantify numerical viscosity effects in multi-dimensional flows. Nevertheless, a good estimate of the magnitude of the numerical diffusion coefficient in two-dimensional cases can be obtained from Ref. 10 as

$$\Gamma_{\text{Numerical}} = \frac{U_R \Delta x \Delta y \sin 2\theta}{4(\Delta y \sin^3\theta + \Delta x \cos^3\theta)} \tag{6}$$

where U_R is the resultant velocity, Δx and Δy are the grid spacings in the x- and y-directions, respectively, and θ is the angle (between 0^0 and 90^0) the velocity vector makes with the x-direction. Several key observations about the nature of numerical diffusion can be made in terms of this expression:

1. Numerical diffusion vanishes when the streamlines are perpendicular to the mesh, i.e., when the flow is along one of the sets of grid lines ($\theta = 0^o$ or 90^o). On the other hand, numerical diffusion increases with streamline curvature becoming most serious when the velocity vector makes an angle of 45^o with the grid lines.
2. There is no numerical diffusion when the gradient of the dependent variable normal to the direction of the flow is zero.
3. Numerical diffusion gets larger with increasing Reynolds number and could become serious in convection dominated flows.
4. Effects of numerical diffusion can be removed by realigning the grid with the flow direction (reducing θ), by changing the size of the mesh (reducing Δx and Δy) or by using both techniques.

Recirculating flows are especially susceptible to numerical diffusion even if the grid is aligned with the primary flow direction. The presence of large regions with strong streamline curvature, such as in the reverse flow zone, creates local regions where numerical diffusion effects can be substantial.

Current techniques for the reduction of numerical diffusion involve the use of grid refinement (or grid-independency) studies in which the number of grid points to be used, to minimize the effects of numerical diffusion, is determined separately in each coordinate direction. In this work grid-independency was determined in the following manner. First, the number of points in the r-direction (NJ) was fixed and the number in the x-direction (NI) was increased in increments for a fixed-length computation domain. The same procedure was then repeated for a fixed NI and variable NJ. The flow parameter tested as a function of grid spacing was the reattachment length x_R. The number of mesh points for grid-independent results was taken as the value of NI and NJ where the reattachment length curve appeared to approach an asymptotic limit. A separate grid refinement study of this nature was conducted for the 2:1 and 1.33:1 diameter ratios. Since the 3:1 diameter ratio expansion represents a flow in which diffusive effects are smaller than in the lower diameter ratio test cases, no separate grid refinement study was conducted for this case, and the grid determined for the 2:1 diameter ratio geometry was used in the definitive calculations of this flow. The results of this work are reviewed below.

2:1 Diameter Ratio Grid Refinement Study

The results of this study are presented in Figure 2.2. For the x-direction, an asymptotic limit for the reattachment length was achieved at values of NI equal to 72 or greater as shown in Figure 2.2a. A slightly different behavior was observed in the r-direction grid refinement study in Figure - 2.2b. The reattachment length initially increases with the number of cross-stream grid points, reaching a peak at an NJ of 28. The curve then monotonically decreases approaching an asymptotic limit at values of NJ exceeding 52. This behavior is probably due to the non-equilibrium wall-function treatment that requires y^{+*} values of 40 to 100 for plausible near-wall results. This range of values for y^+ is approached only at the higher NJ values as shown in Table 2.1.

TABLE 2.1. Variation of y^+ Values

GRID SIZE		
NI	NJ	y^+
22	22	250
22	24	218
22	28	181
22	32	161
22	36	144
22	42	125
22	52	103

Comparison of velocity profiles provides more insight into the effects of numerical diffusion. Figure 2.3 presents the axial velocity profiles

---

[*] $y^+ = \frac{k_v^{1/2} y_p}{\nu}$ where k_v is the turbulent kinetic energy at the edge of the viscous sublayer, y_p is the distance of the node to the wall and ν is the kinematic viscosity.

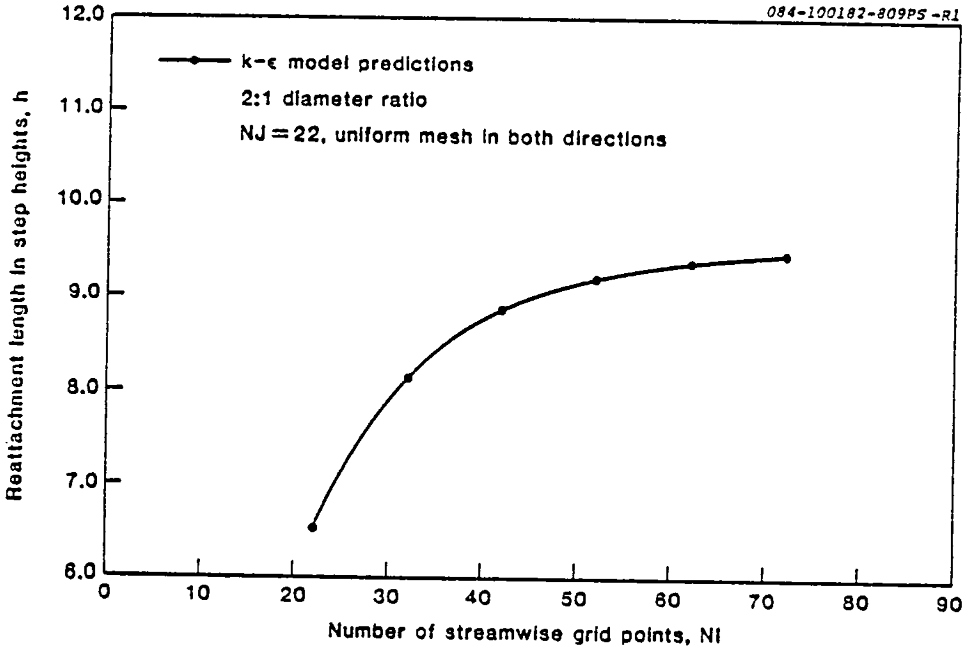

(a) x - direction study

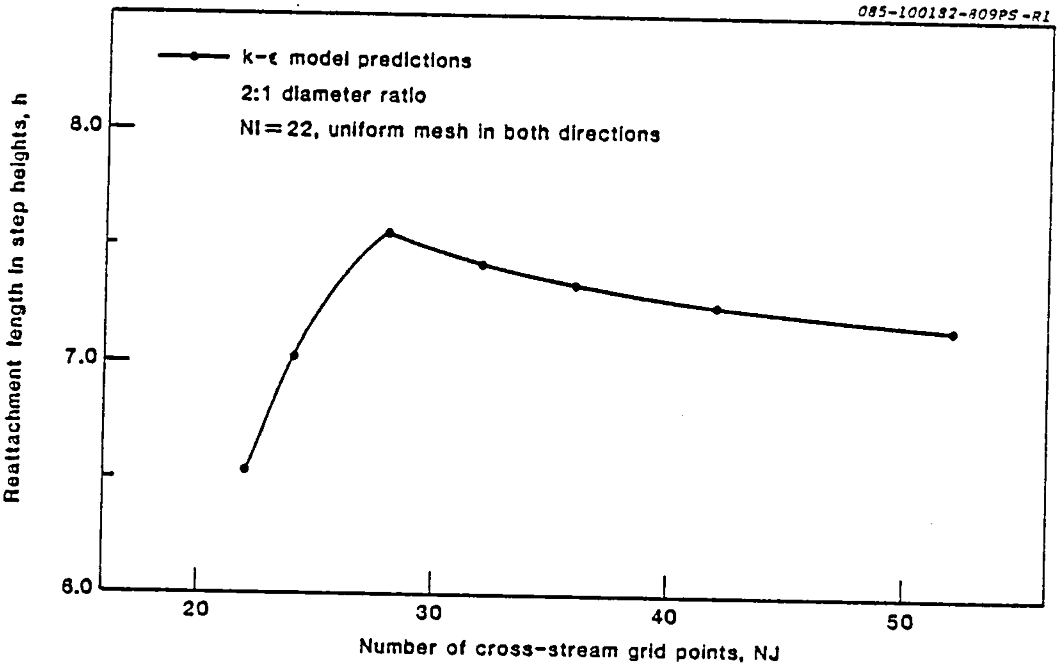

(b) r - direction study

Figure 2.2. Grid-independency studies

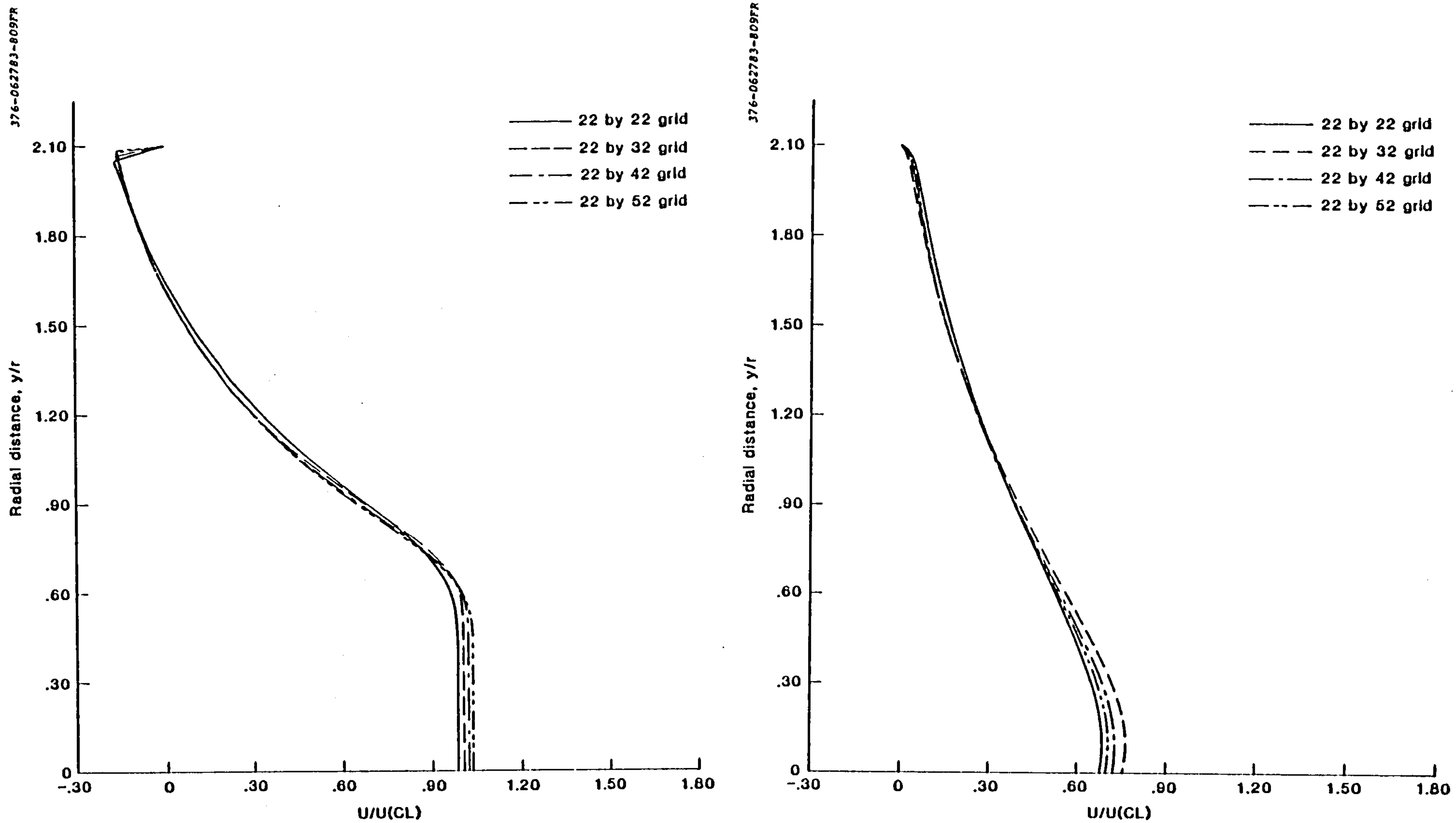

(a) x/h = 2.0

(b) x/h = 3.0

FIGURE 2.3. Axial Velocity Profiles, 2:1 Diameter Ratio. Sudden Expansion. As a Function of Grid Refinement. k-ε Turbulence Model.

at x/h locations of 2 and 8, as predicted using 22 by 22, 22 by 32, 22 by 42, and 22 by 52 node grids. The main differences between the profiles are in their behavior near the wall, and across the separated shear layer towards the centerline. Excluding the coarsest 22 by 22 mesh, the differences between the predictions for the remaining grids are small. This is consistent with the reattachment length computations reported in Figure 2.2b which also show a relatively small variation of x_R with the number of cross-stream grid points for meshes finer than 22 by 32. Axial velocity predictions carried out using 22 by 22, 32 by 22, 42 by 22, and 52 by 22 node grids are reported in Figure 2.4 at x/h locations of 2 and 8. The differences between these velocity profiles are more pronounced than those observed with increasing number of grid points in the radial direction since the reattachment length changes significantly with the number of streamwise grid points, as shown in Figure 2.2a.

This study shows that practically numerical diffusion free and fully-converged results can be obtained for a 2:1 diameter ratio axisymmetric sudden expansion, with the STEP code (Ref. 9), by using a 72 by 52 node mesh (uniform in each coordinate direction) for a solution domain length of 16 step heights and a convergence criterion of a residual source level of 0.001. However, it is possible to obtain acceptable results by using a smaller number of carefully nonuniformly distributed grid points, as demonstrated in Figure 2.1, where a nonuniform 22 by 22 node mesh resulted in reattachment length predictions in excess of 8.8 step heights, reasonably close to the ultimate value reached in the grid refinement study just described. Thus, the second phase of this grid refinement work involved establishing a nonuniform grid which minimized numerical diffusion effects through comparison with the results obtained using the 72 by 52 node mesh determined previously. Nonuniform 22 by 22 and 59 by 43 node grids were devised by studying measurements and coarse mesh calculations of the given geometry to identify the regions of sharp gradients, and adjusting grid spacing accordingly for efficient node distribution. The baseline 72 by 52 node mesh computations were then matched with the predictions obtained using these two nonuniform grids for both the standard and "modified" versions of the k-ε and the ASM models. The goals of this study were to document the effects of numerical diffusion in terms of reattachment length, velocity, turbulent kinetic energy, and Reynolds shear stress predictions.

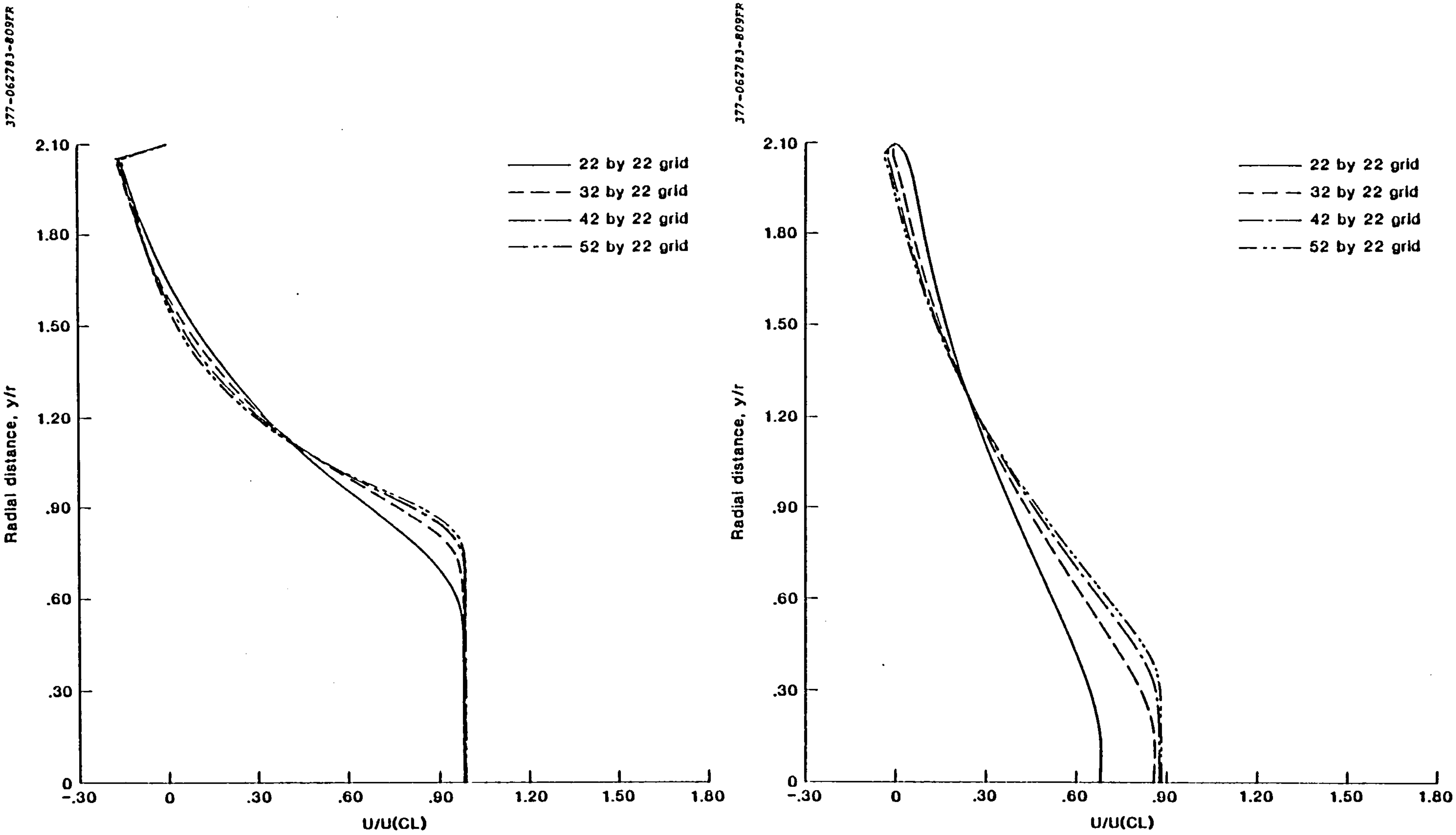

(a)

x/h = 2.0

(b)

x/h = 8.0

FIGURE 2.4. Axial Velocity Profiles, 2:1 Diameter Ratio Sudden Expansion, as a Function of Grid Refinement. k-ε Turbulence Model.

Calculations of this geometry were carried out for a solution domain length of 16.471 step heights, with a residual source convergence criterion of 0.001. A sketch of the computational domain is shown in Figure 2.5. For all three grids, the same inlet velocity profile extracted from the Chaturvedi data (Ref. 3) was used at $x/h = -0.471$ to start the computations, and the inlet turbulent kinetic energy and dissipation rates were calculated from this profile using Prandtl's mixing length hypothesis.

Reattachment Length Predictions

In Table 2.2 the reattachment length predictions obtained using the 22 by 22 and 59 by 43 node grids with the 72 by 52 node baseline results for all four models are compared. These results indicate that the reattachment length predictions with the 22 by 22 grid do indeed suffer from numerical diffusion. The reattachment length increases by 16.9%, 16.2%, 14.7%, and 5.0%, respectively, for the k-ε, "modified" k-ε, algebraic stress and "modified" algebraic stress models when the grid is further refined to the baseline 72 by 52 mesh. The relatively small change in the "modified" algebraic stress model predictions may be explained in terms of two counteracting phenomena. The fine grid reduces numerical diffusion so that the computed separated shear layer spreads less rapidly which in turn produces a larger recirculation region. On the other hand, the better resolution provided by the fine mesh enhances the sensitivity of the model to the secondary strains created by the curvature of the flowfield. Thus, the net result is a smaller increase in the reattachment length than that observed for the other models. Predictions made with the 59 by 43 node are in excellent agreement with the baseline results indicating a good node distribution within the mesh. The danger associated with not separating the effects of numerics from the performance of turbulence models is especially apparent for this case. Note that the numerically diffusive 22 by 22 grid predictions seem to agree very favorably with the experiment, giving a false impression of the predictive capability of the models at this diameter ratio.

Velocity, Turbulent Kinetic Energy and Reynolds Shear Stress Predictions

The effects of grid refinement on the velocity, turbulent kinetic energy and Reynolds shear stress predictions are discussed below. The results are

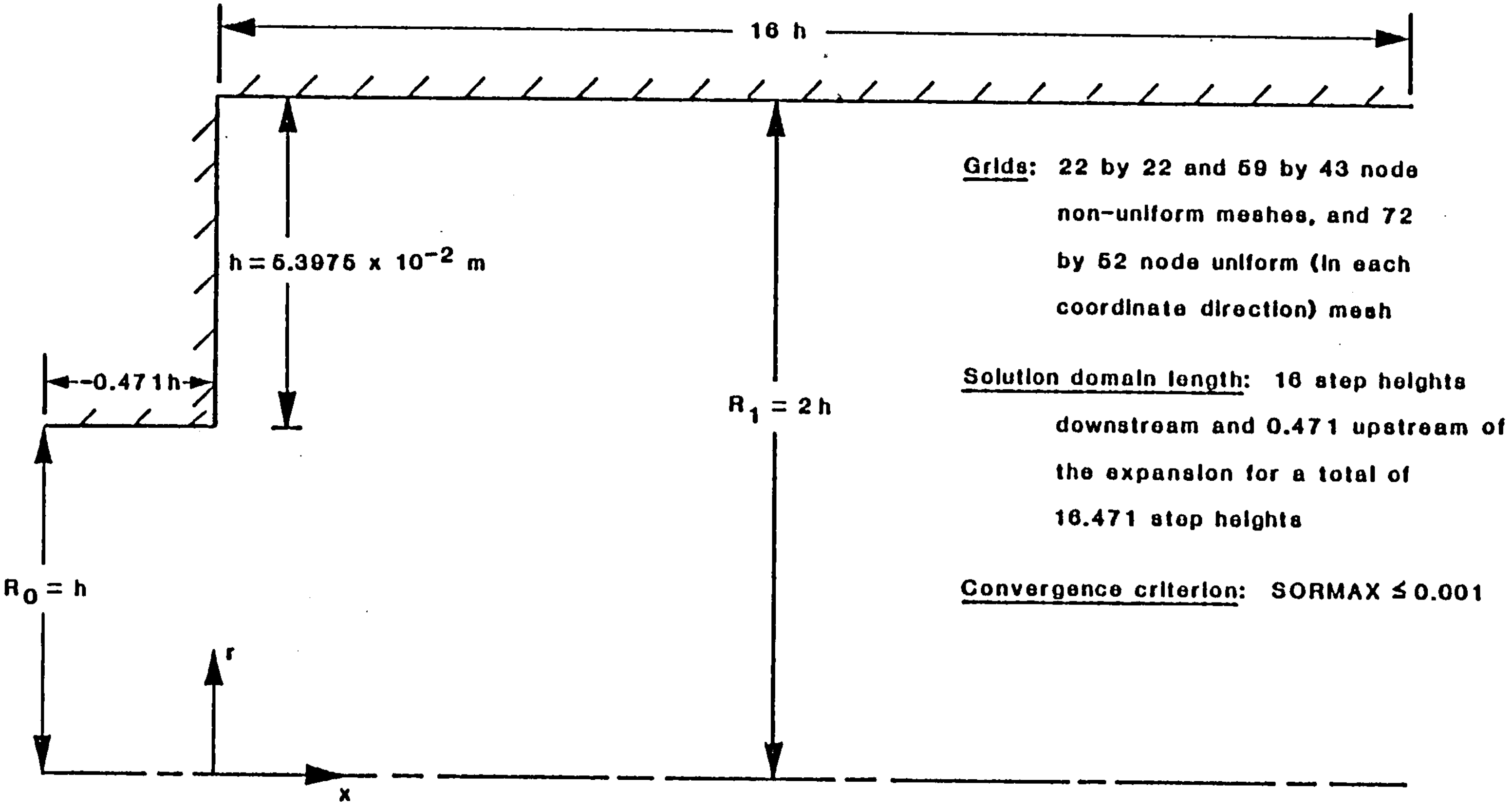

Grids: 22 by 22 and 59 by 43 node non-uniform meshes, and 72 by 52 node uniform (in each coordinate direction) mesh

Solution domain length: 16 step heights downstream and 0.471 upstream of the expansion for a total of 16.471 step heights

Convergence criterion: SORMAX $\leq$ 0.001

Figure 2.5. Solution domain used in the Chaturvedi (2:1 diameter ratio) predictions

TABLE 2.3. Reattachment Length Predictions

MODEL	GRID	REATTACHMENT LENGTH IN STEP HEIGHTS
k-ε	72 x 52	9.53
	59 x 43	9.57
	22 x 22	8.15
M. k-ε	72 x 52	9.62
	59 x 43	9.68
	22 x 22	8.28
ASM	72 x 52	9.30
	59 x 43	9.34
	22 x 22	8.11
M. ASM	72 x 52	10.22
	59 x 43	10.21
	22 x 22	9.73
Data, Ref. 3		9.4 ± 1*

---

* The uncertainty in the Chaturvedi 2:1 diameter ratio reattchment length measurements is estimated to be ± 1 step height.

presented at an x/h location of 5 for the 22 by 22, 59 by 43 and 72 by 52 node grids.

Figures 2.6 and 2.7 present the U, k and uv predictions for the k-ε and "modified" k-ε models, respectively. Similar results are reported in Figures 2.8 and 2.9, respectively, for the standard and "modified" versions of the algebraic stress model. The following conclusions can be drawn on the effects of numerical diffusion in the Chaturvedi predictions from these results:

1. The qualitative effects of numerical diffusion are the same for all models. Quantitatively, the "modified" algebraic stress model predictions appear to be the least sensitive to grid refinement. However, this may be the result of the two counteracting phenomena discussed in the preceding section.

2. The agreement between the baseline results and the 59 by 43 grid predictions is excellent for all variables and models.

3. The differences between the 22 by 22 grid results and the baseline predictions are significant, and these should be viewed in conjunction with the reattachment length computations.
    a. The main effect of numerical diffusion is a more rapid predicted rate of spread for the separated shear layer, and consequently a shorter reattachment length.
    b. These effects can be seen in the progressively faster rate of decay of the centerline velocity. Also higher levels of kinetic energy and shear stress are predicted, indicating a shorter yet more intense recirculation zone.
    c, A subsequent drop in the levels of these quantities, typical for the recovery region, signals reattachment of the separated shear layer and beginning of the relaxation regime.

Summary

The results of this study showed that the nonuniform 59 by 43 node grid does indeed match the baseline predictions extremely well and can be

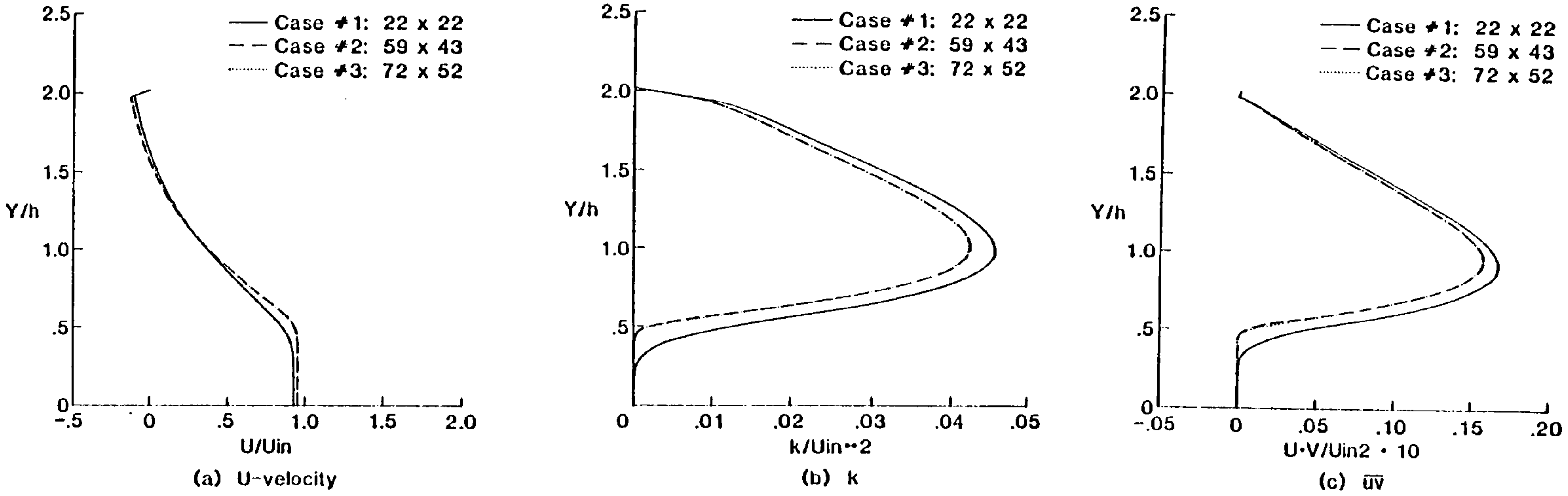

(a) U-velocity

(b) k

(c) $\overline{uv}$

Figure 2.6. U-velocity, k, and $\overline{uv}$ predictions at $X/h = 5.0$, k-ϵ

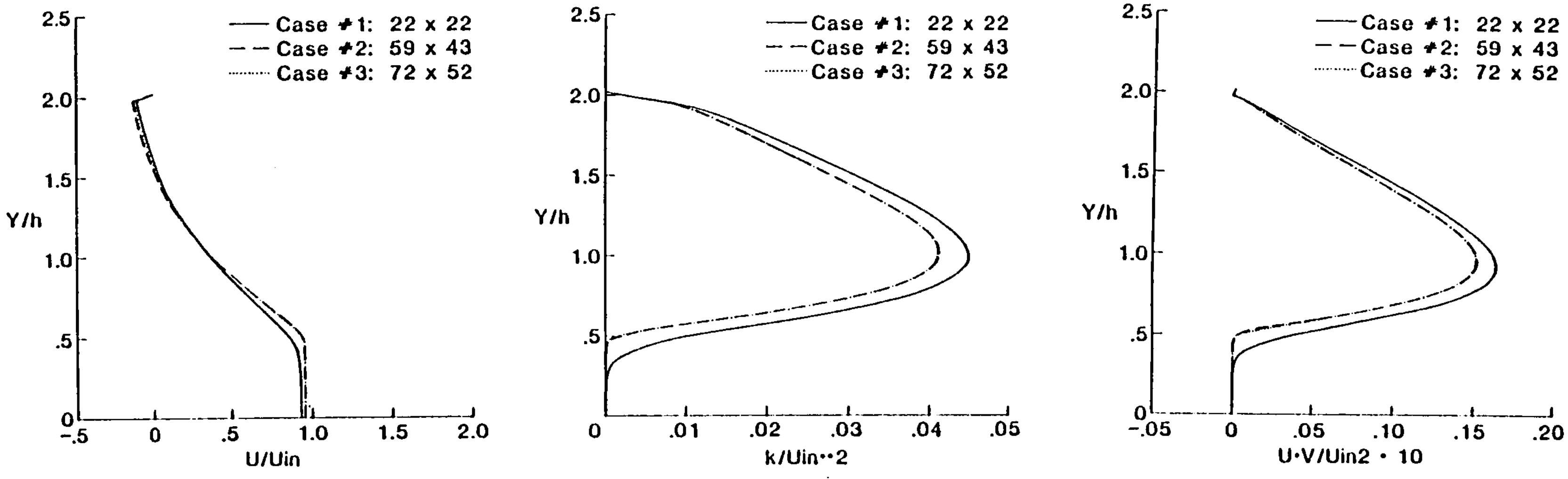

(a) U-velocity (b) k (c) $\overline{uv}$

Figure 2.7. U-velocity, k, and $\overline{uv}$ predictions at X/h = 5.0, M. k-ε

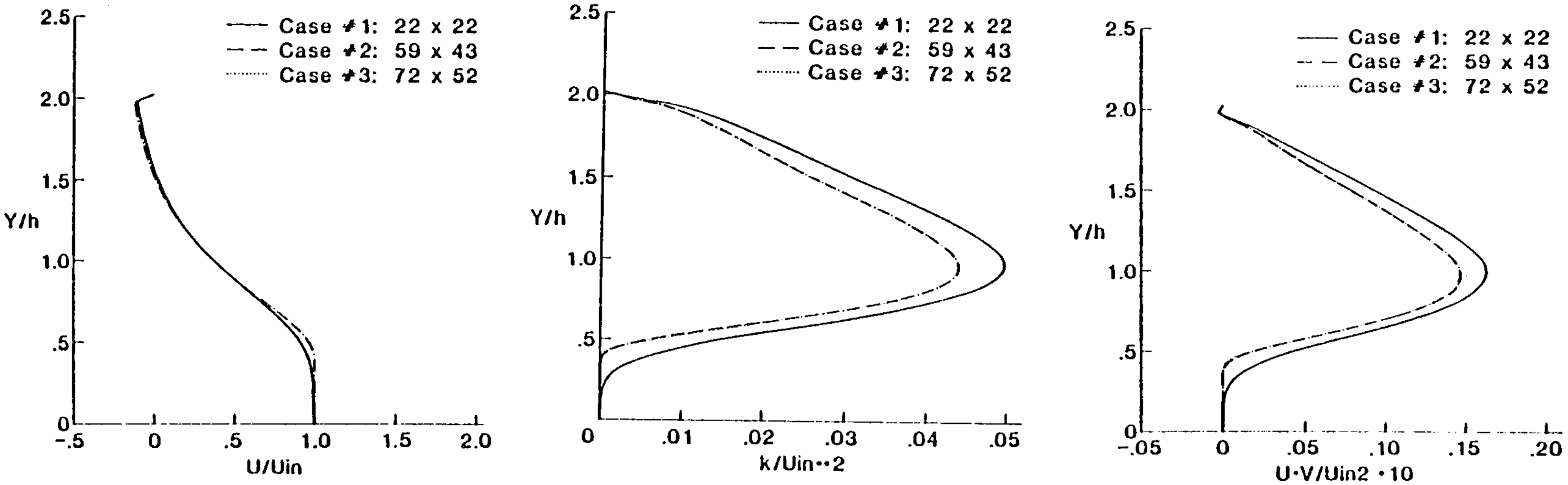

(a) U-velocity (b) k (c) $\overline{uv}$

Figure 2.8. U-velocity, k, and $\overline{uv}$ predictions at X/h = 5.0, ASM.

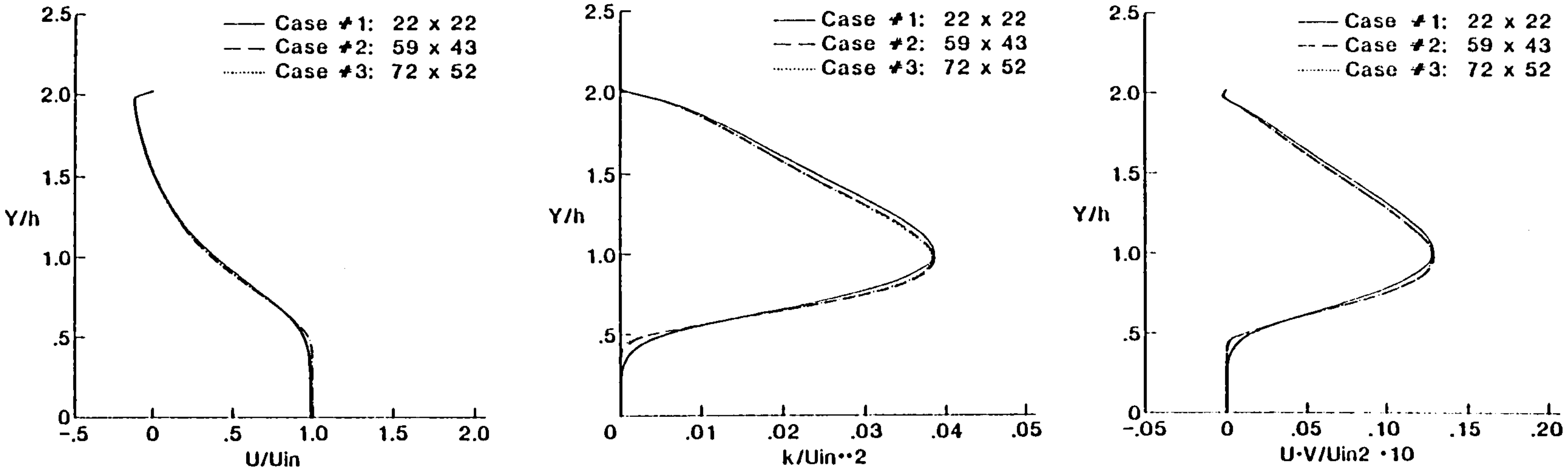

(a) U-velocity (b) k (c) $\overline{uv}$

Figure 2.9. U-velocity, k, and $\overline{uv}$ predictions at X/h = 5.0, M. ASM.

used in definitive numerical diffusion free predictions of the Chaturvedi geometry at substantial savings ($\approx 40\%$) over the 72 by 52 node baseline grid. The nonuniform 22 by 22 node grid suffers from the effects of numerical diffusion, and thus, grids of this coarseness should be used mainly in preliminary computations or to establish qualitative flow trends. In addition, this study confirmed the role of the reattachment length as a sensitive index of the degree of numerical diffusion in both the k-ε and algebraic stress model predictions. Hence, parametric studies of reattachment lengths as a function of grid spacing are sufficient in constructing nonuniform grids to minimize numerical diffusion. This important observation was used in the subsequent studies.

1.33:1 Diameter Ratio Grid Refinement Study

The computational domain length and convergence criteria for this geometry were established as 16 step heights and SORMAX = 0.001, respectively, based on the 2:1 diameter ratio results already discussed. The flow geometry and solution domain are shown in Figure 2.10. The grid refinement work proceeded in the same manner as that already described: the number of points in the r-direction (NJ) was first fixed, and the number in the x-direction (NI) was increased in installments for the fixed length computational domain until further changes in predicted recirculation zone length no longer occurred. The same procedure was then repeated for a fixed NI and variable NJ. The number of mesh points for grid independent results would have been taken as the value of NI and NJ where the reattachment length curve appeared to approach an asymptotic limit. However, within the NI (22-78) and NJ (22-82) values studied, this limit was not reached. Therefore, as shown in Figure 2.11 the reattachment length curves were extrapolated to their asymptotic limits using the reported x_R values. These results showed that a mesh of at least 108 by 130 nodes of uniform spacing was needed to obtain grid independent predictions of this geometry.

The next step was to devise and test nonuniform grids employing fewer, but nonuniformly distributed grid points against the reattachment length predictions reported in Figure 2.11. Nonuniform meshes of 22, 32, 42, 52,

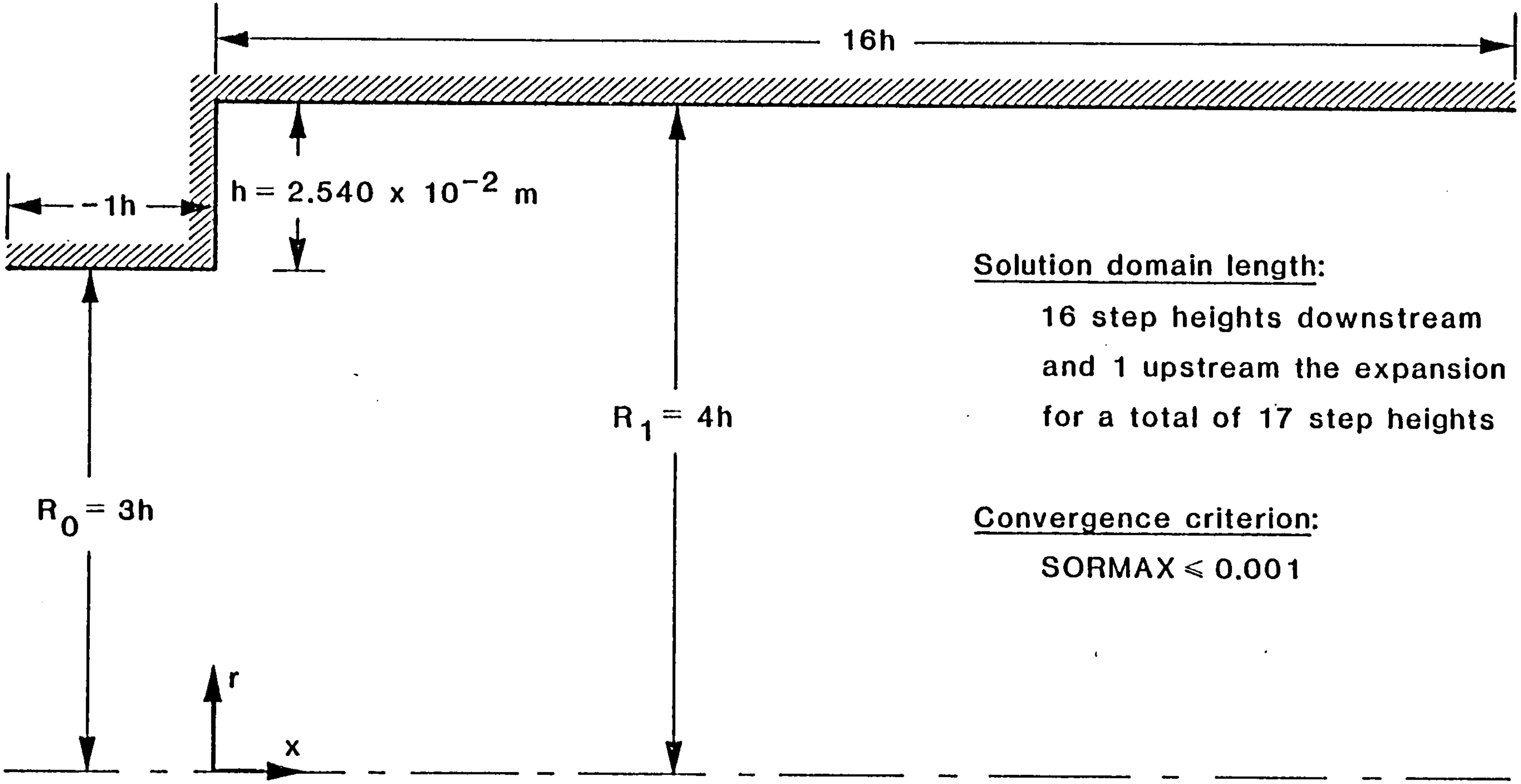

<u>Solution domain length</u>:

16 step heights downstream and 1 upstream the expansion for a total of 17 step heights

<u>Convergence criterion</u>:

SORMAX $\leq$ 0.001

Figure 2.10. Solution domain for the 1.33:1 diameter ratio axisymmetric sudden-expansion geometry.

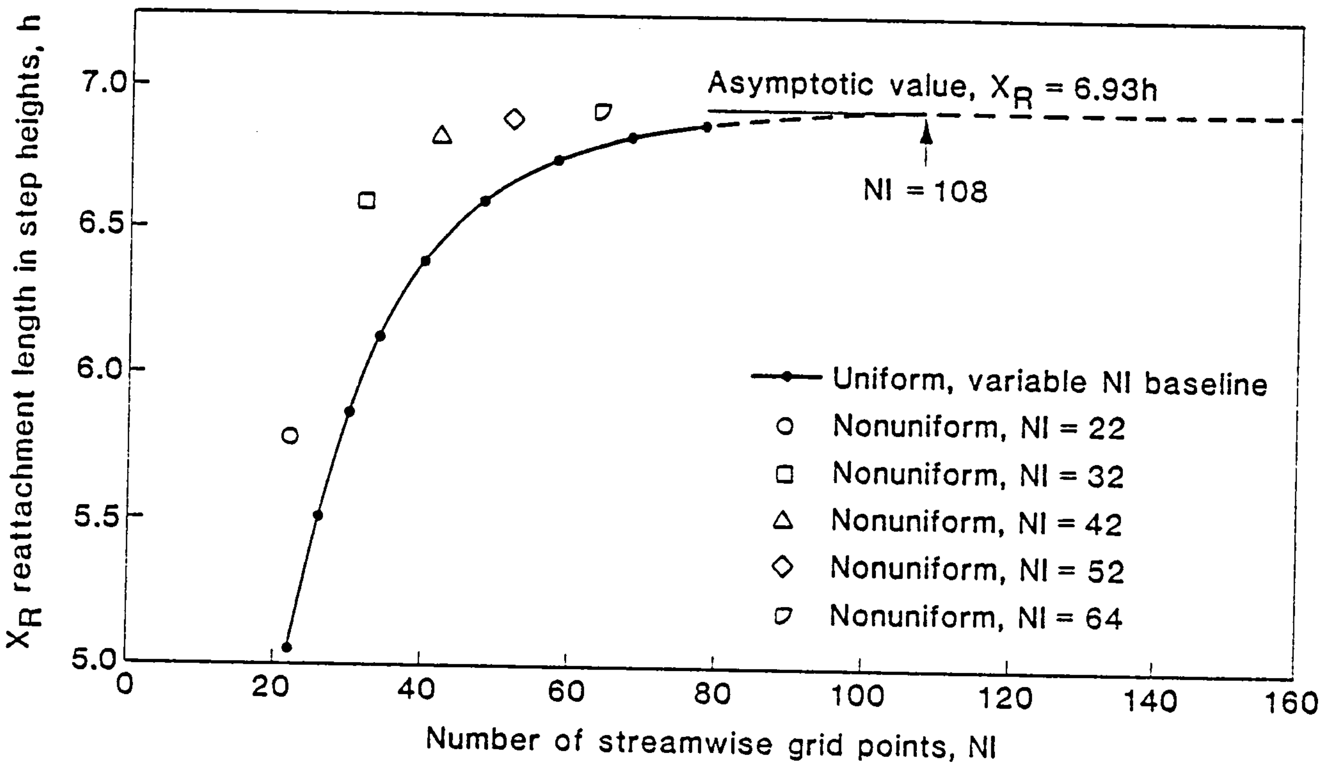

(A) NJ held fixed at 22

383-062783-809FR

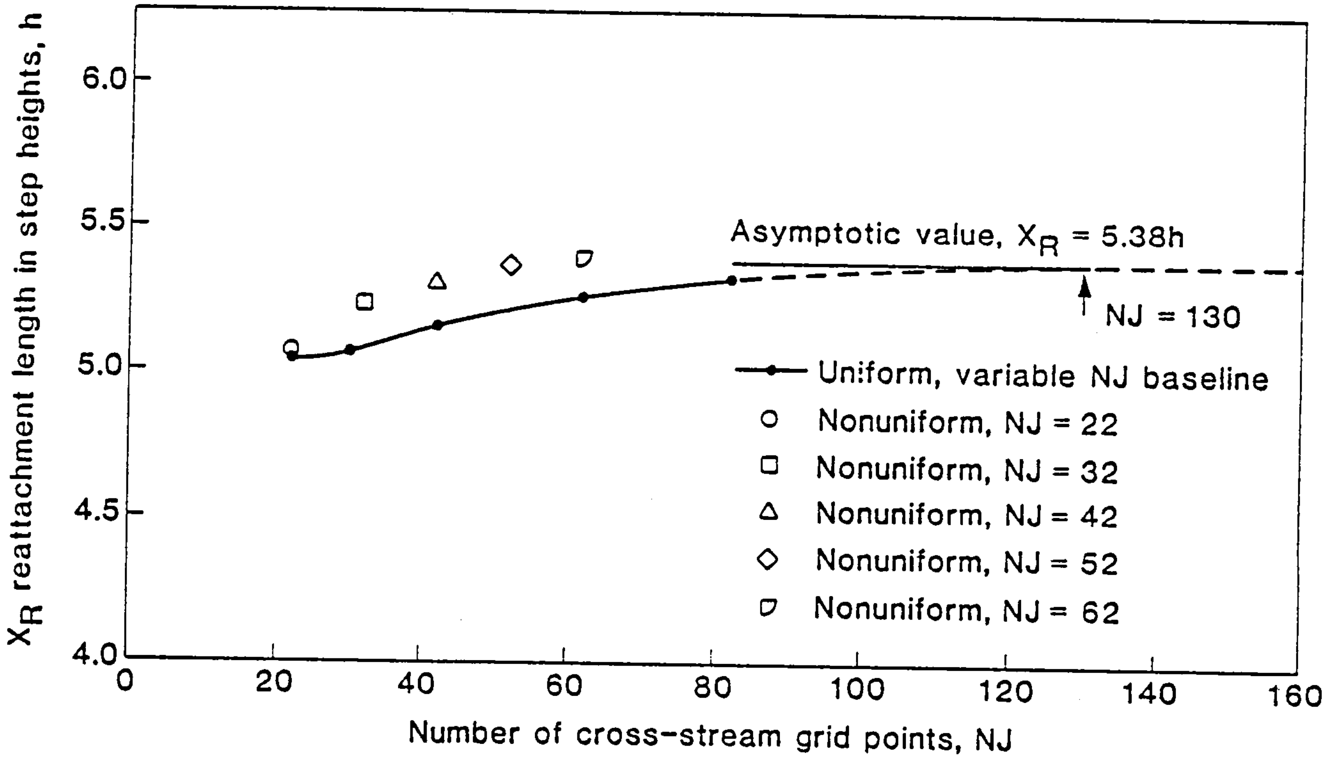

(B) NI held fixed at 22

Figure 2.11. 1.33:1 diameter ratio axisymmetric sudden-expansion streamwise (NJ = 22) and radial (NI = 22) direction studies.

and 64 nodes in the streamwise direction coupled with 22 uniformly-spaced nodes in the radial direction were matched against the asymptotic reattachment length predictions in Figure 2.11(a). A similar study, Figure 2.11(b), was also conducted using 22, 32, 42, 52, and 62 nonuniformly-spaced nodes in the radial direction and 22 nodes with constant spacing in the streamwise direction. These tests produced the 64 by 62 nonuniform grid that was used in the definitive numerical diffusion free calculations of this geometry with the k-ε, "modified" k-ε, ASM, and "modified" ASM models.

This work again emphasizes the need for grid refinement and related studies before model evaluations are undertaken. The difference in the reattachment length predictions alone varies by as much as 1.2 step heights between the finest (62 by 22) and the coarsest (22 by 22) grids tested. It is interesting to note that nonuniform grids simply shift the reattachment length curve to higher values at a given value of NI or NJ. The variation of reattachment length with grid spacing is remarkably smooth in both coordinate directions and by and large displays the desired behavior.

3:1 Diameter Ratio Grid Refinement Study

Since this diameter ratio represents numerically a less diffusive flow than the 2:1 diameter ratio case, the 59 by 43 node grid determined for the 2:1 diameter ratio expansion was also used for this diameter ratio. The computation domain length and convergence criteria were again taken as 16 step heights, and 0.001, respectively. The flow geometry and the solution domain are shown in Figure 2.12.

Summary

This phase of the work involved a parametric study to assess the effects of numerics on the accuracy of flowfield predictions. Solution domain length, convergence criteria and numerical diffusion were all considered. A study of this nature is essential in most computational work to separate the effects of numerics from the influence of analytical models in assessing the predictions. The results of the present study, which provided the solution domain length, convergence criteria and the mesh size to be used in the definitive test case calculations, are summarized in Table 2.3.

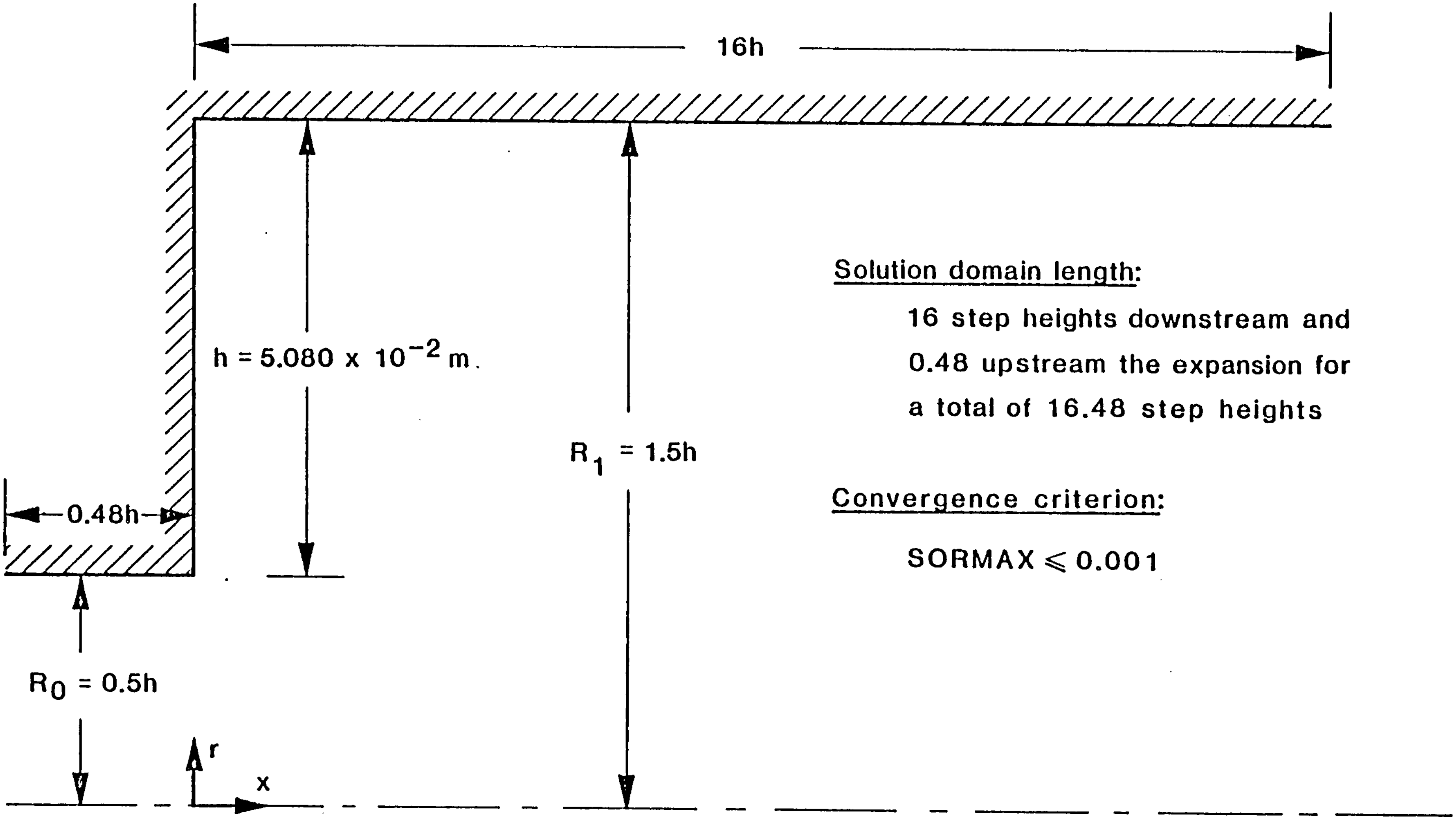

Solution domain length:

16 step heights downstream and 0.48 upstream the expansion for a total of 16.48 step heights

Convergence criterion:

SORMAX $\leqslant$ 0.001

Figure 2.12. Solution domain for the 3:1 diameter ratio axisymmetric sudden-expansion geometry.

TABLE 2.3. Summary of Results.

DIAMETER RATIO	GRID SIZE	SOLUTION DOMAIN LENGTH, Step Height	CONVERGENCE CRITERIA
1.33:1	64 by 62	16	0.001
2:1	59 by 43	16	0.001
3:1	59 by 41	16	0.001

It was also shown that the reattachment length is indeed a sensitive index of the degree of numerical diffusion for both k-ε and algebraic stress model predictions.

2.5 ASSESSMENT OF MODELS FOR AXISYMMETRIC SUDDEN EXPANSION FLOWS AT DIFFERENT DIAMETER RATIOS

This phase of the study included the definitive prediction of the 1.33:1, 2:1, and 3:1 diameter ratio cases with the standard and the "modified" versions of the k-ε and the algebraic stress models for the computation domain length, convergence criteria and the mesh size specified in Section 2.1.1. Assessment of model performance and the effects of diameter ratio on sudden expansion flow predictions are discussed next in terms of reattachment length, mean velocity and Reynolds stress calculations.

Reattachment Length Predictions

The reattachment length predictions for the different diameter ratios investigated are shown in Table 2.4 and Figure 2.13. Here the "primary" recirculation zone is that which forms downstream of the step along the outer wall of the sudden expansion; the "secondary" recirculation zone is a counter-

TABLE 2.4. Reattachment Length Predictions

DIAMETER RATIO	REATTACHMENT LENGTHS IN STEP HEIGHTS								
	PRIMARY RECIRCULATION ZONE					SECONDARY RECIRCULATION ZONE			
	KEM	M.KEM	ASM	M.ASM	MEASUREMENTS	KEM	M.KEM	ASM	M.ASM
1.33:1	7.40	7.60	7.73	8.82		0.19	0.18	0.55	0.51
2:1	9.57	9.68	9.34	10.21	9.4 ± 1	0	0	0.44	0.41
3:1	8.61	8.66	8.20	8.37		0	0	0	0

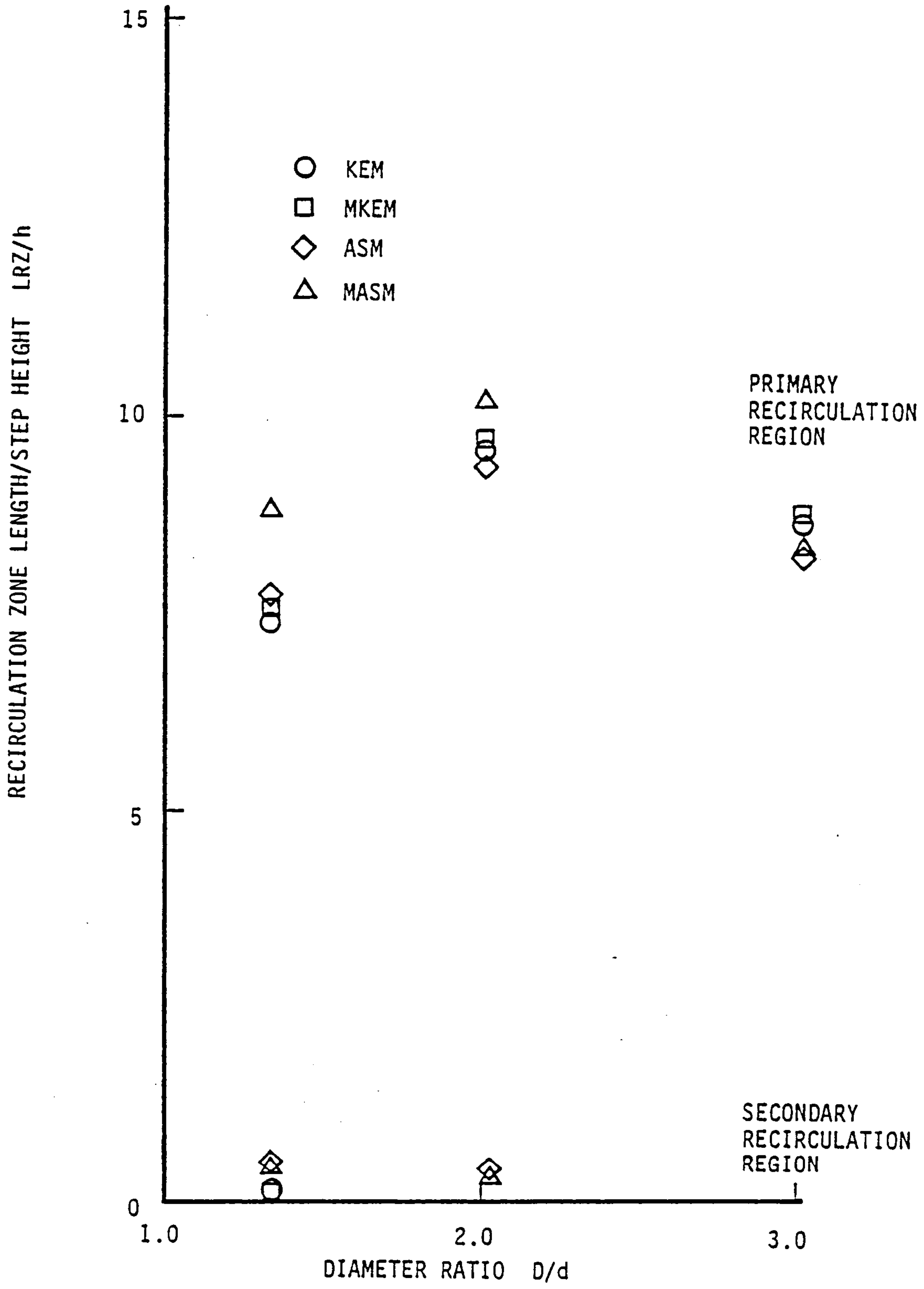

FIGURE 2.13. Turbulence Model Predictions of Primary and Secondary Recirculation Zone Length as a Function of Diameter Ratio.

rotating eddy which, with some turbulence models, is predicted to exist in the corner between the step and the outer wall. The physical presence of this eddy is somewhat controversial; however certain indirect evidence points to its existence. Note from the tabulated data and Figure 2.13 that all models predict the existence of a counterrotating eddy at small diameter ratios and that the predictions indicate that the size of the eddy decreases as the sudden-expansion diameter ratio increases. Prediction of the location and size of the counterrotating eddy is a function of both turbulence model and grid resolution, providing again evidence of the need for fine grid resolution in prediction of the details of turbulent reacting flows.

Note from Figure 2.13 the existence of a maximum in recirculation zone length (in step heights) as a function of diameter ratio. This is somewhat misleading, since step height also increases with diameter ratio, as $h = (D-d)/2$. In fact, the absolute length of the recirculation zone continues to increase as diameter ratio (or step height) increases, as shown in Figure 2.14. A data correlation obtained by Drewry (Ref. 11) from a variety of sources is also shown on Figure 2.14, and the predictions of all of the turbulence models examined are in reasonably good agreement with this correlation.

Several inferences can be drawn from this comparison of reattachment length predictions. First, compared with the differences observed as a function of grid spacing with a single turbulence model, the differences in zone length prediction between difference turbulence models in this sudden expansion flowfield are nearly negligible. Only at the lowest diameter ratio, where pressure gradient effects on the mixing process are smallest, do significant differences in results of the different models become evident, and in this case it is only the modified algebraic stress model which provides significantly different results. The difference in results zone length between the modified ASM and other turbulence models is consistent with the results for planar separated flows described in Ref. 2; however, it must be noted that at a diameter ratio of 2.0, where the Chaturvedi data (Ref. 3) is available, the recirculation zone length experimentally measured does not agree with the modified ASM result (Table 2.4). It might also be noted that the computational results (and Chaturvedi's data) are not fully in agreement with the correlation band shown in Figure 2.14 and, indeed,

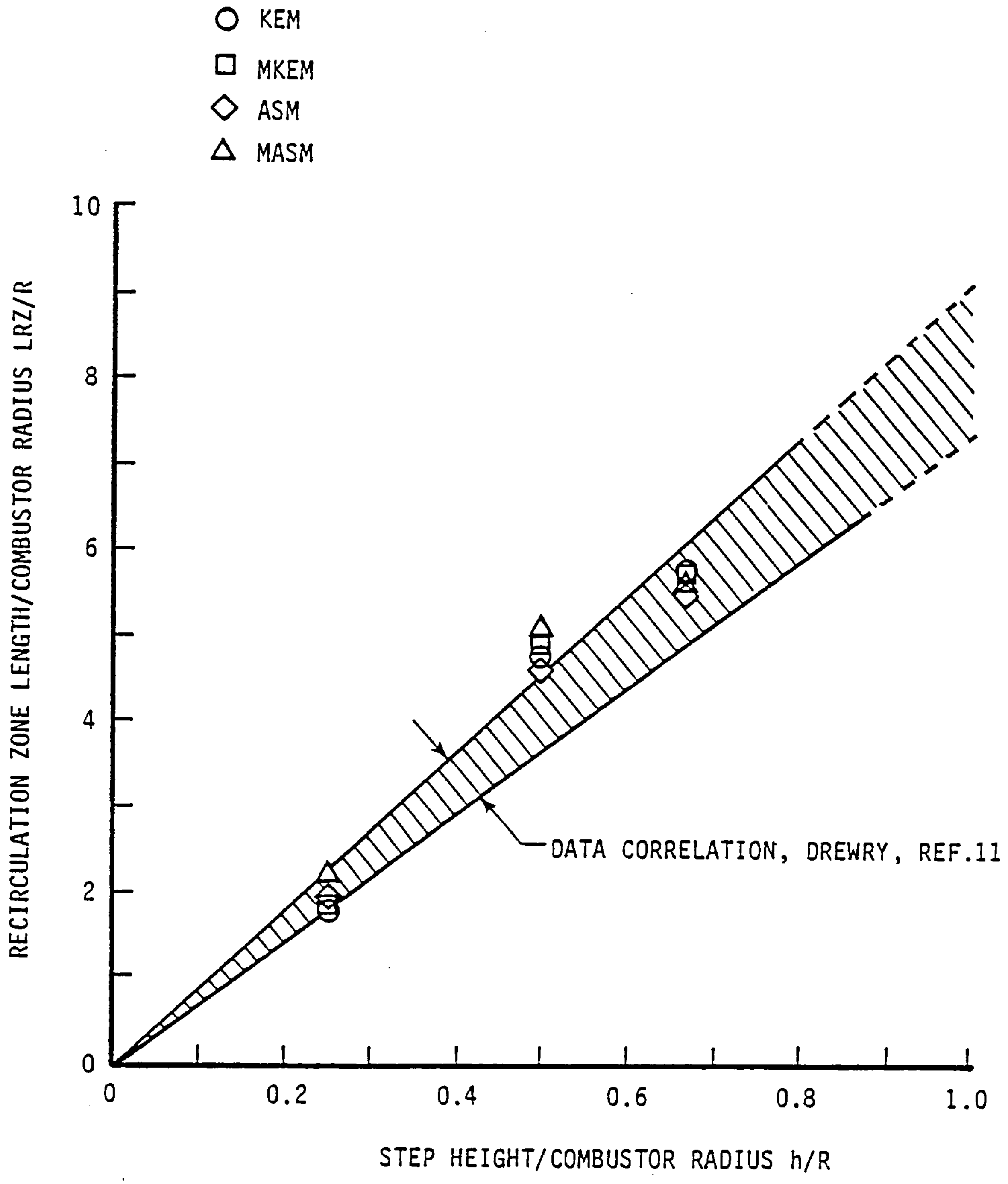

FIGURE 2.14. Comparison of Predicted Recirculation Zone Lengths with Experimental Data Correlation.

the computed results indicate that the linear relationship between recirculation zone length and step height obtained by Drewry may not, in fact, exist.

Velocity and Shear Stress Profile Comparisons, Diameter Ratio = 2.0

Figure 2.15 presents a comparison of the axial velocity profiles as predicted by the four turbulence models and Chaturvedi's experimental data (Ref. 3) at x/h values of 2, 4, 6, 8, and 12. Up to an x/h of 8, there are no significant differences between the profiles as predicted by the four models. In fact, referring to the results shown in Section 2.1.1, the differences observed throughout the flow are much smaller than differences induced by grid refinement. At the final two stations, the standard and "modified" versions of the ASM predict larger centerline velocities which correspond to a slower rate of spread of the separated shear layer toward the centerline. This behavior is more pronounced for the modified ASM, consistent with the larger recirculation zone this model predicts.

Agreement between the measurements and the predictions is generally acceptable but by no means perfect in the recirculation and near-centerline regions. Across the separated shear layer, predictions consistently fall short of the data indicating a more slowly developing shear layer. KEM and "modified" KEM display better agreement with the measurements near and downstream of the reattachment point. All models seem to do equally well further upstream.

Predicted and measured profiles of the axial Reynolds stress component are presented in Figure 2.16 for x/h values of 2, 4, 6, 8, and 12. All four models compute similar $\overline{u_x u_r}$ profiles along the duct which only differ in magnitude. Up to an x/h of 8, the KEM, "modified" KEM and ASM predictions are hardly distinguishable. In this region the "modified" ASM predictions show the most rapid decrease in shear stress level. Beyond x/h = 8, the KEM and modified KEM predictions of shear stress decay rate increase and eventually these models predict lower shear stress levels than both the modified and standard ASM. The behavior of the measured stress profiles is successfully predicted by all models. The computed stress levels however are generally higher, except at the first station, than the measured values. In the recirculation region the "modified" ASM shows the better agreement with the data. Further downstream, KEM and "modified" KEM predictions appear to be more successful in this respect.

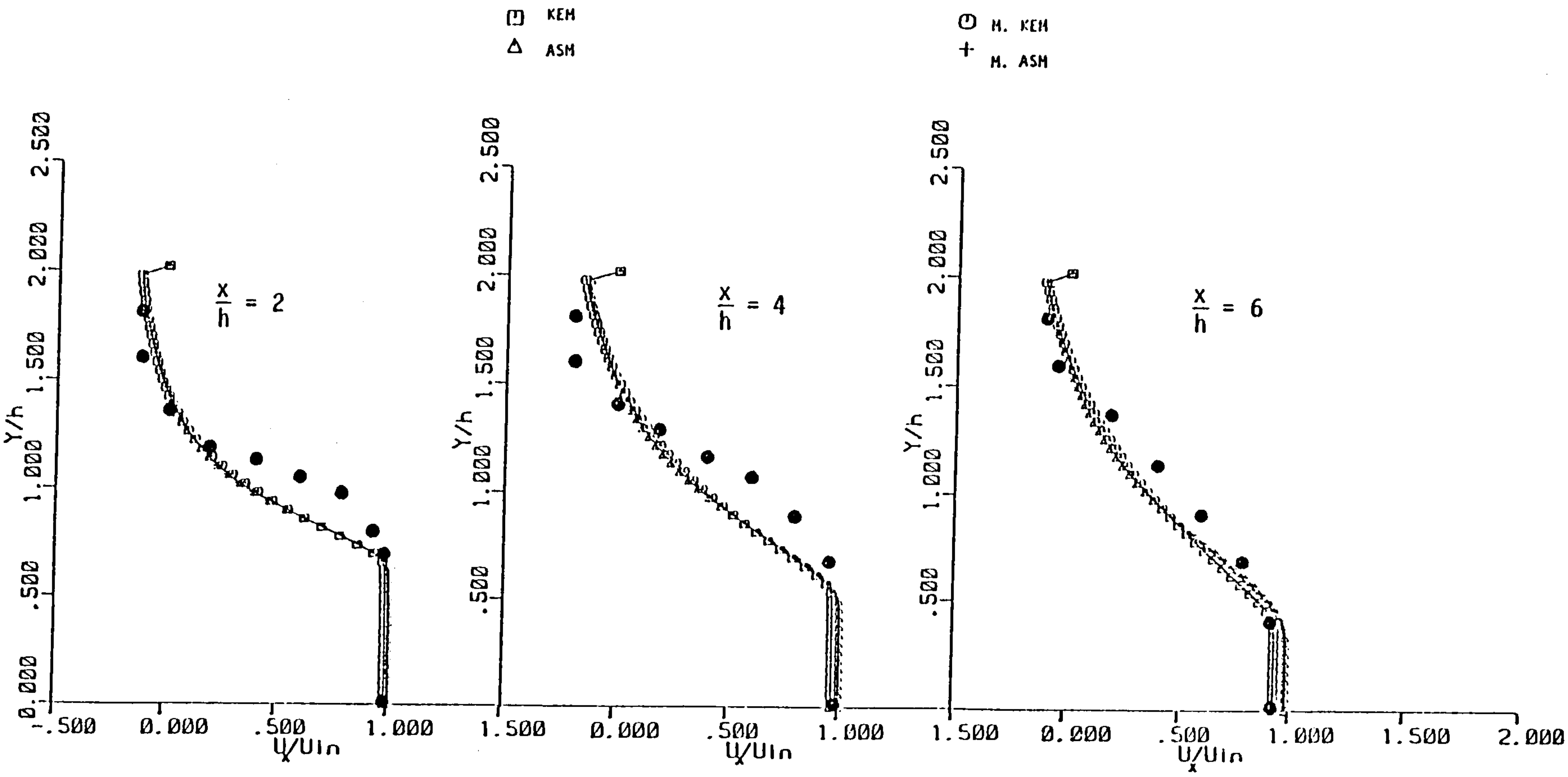

FIGURE 2.15. Comparison of Turbulence Model Predictions of Axial Velocity, Diameter Ratio 2.0 Sudden Expansion. Data from Ref. 3.

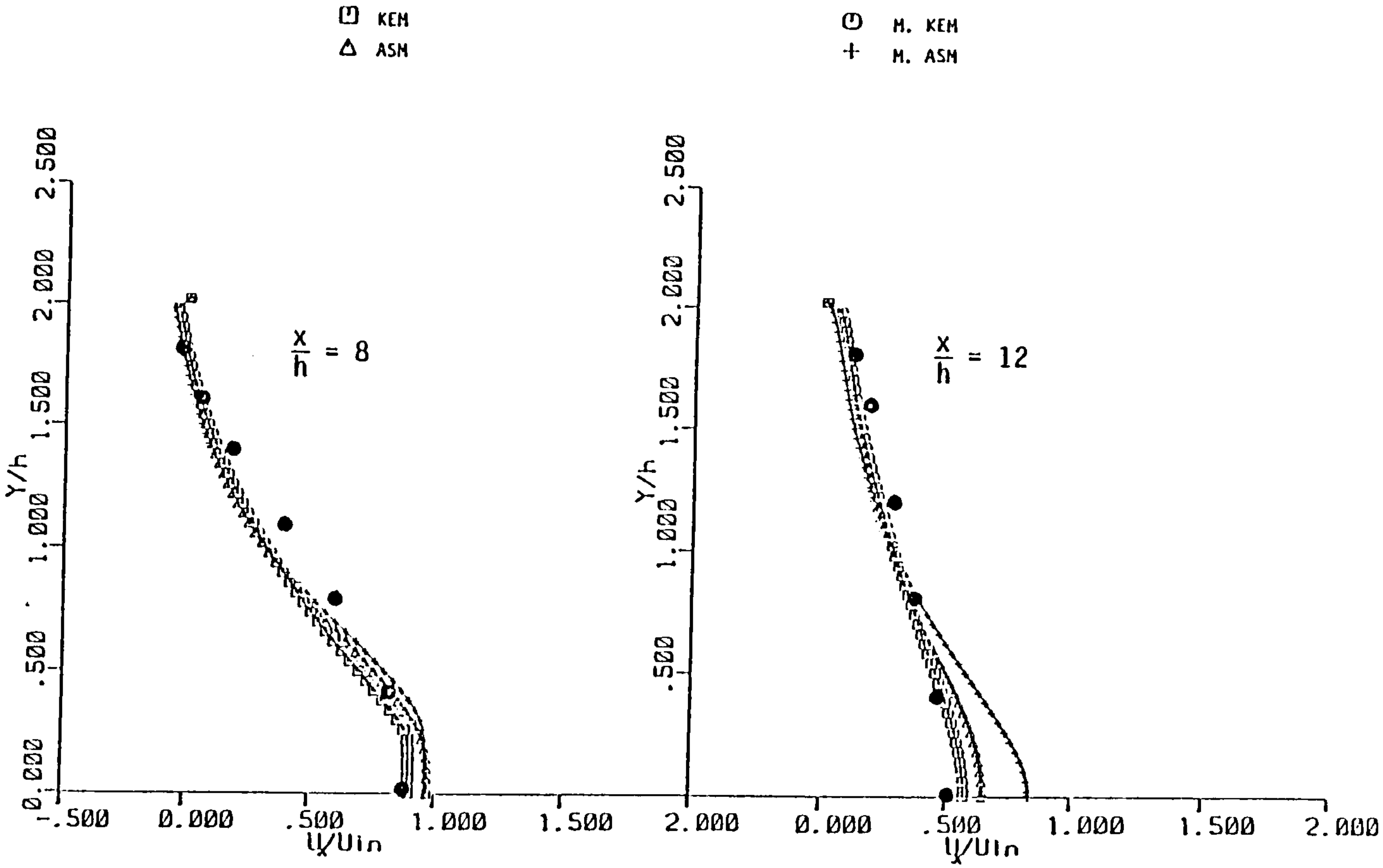

FIGURE 2.15, concluded. Comparison of Turbulence Model Predictions of Axial Velocity, Diameter Ratio 2.0 Axisymmetric Sudden Expansion. Data from Ref. 3.

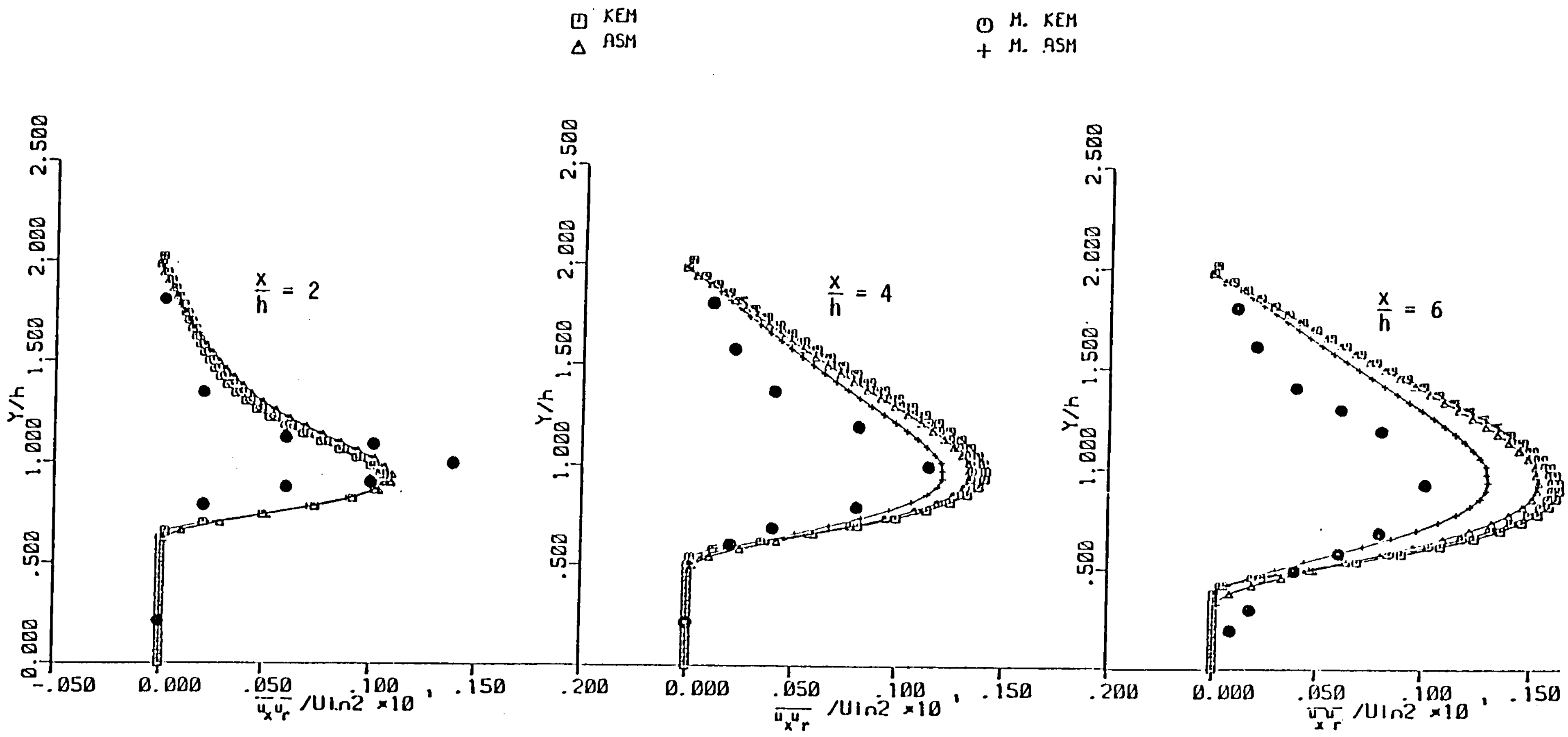

FIGURE 2.16. Comparison of Turbulence Model Predictions of Axial Reynolds Stress, Diameter Ratio 2.0 Symmetric Sudden Expansion. Data from Ref. 3.

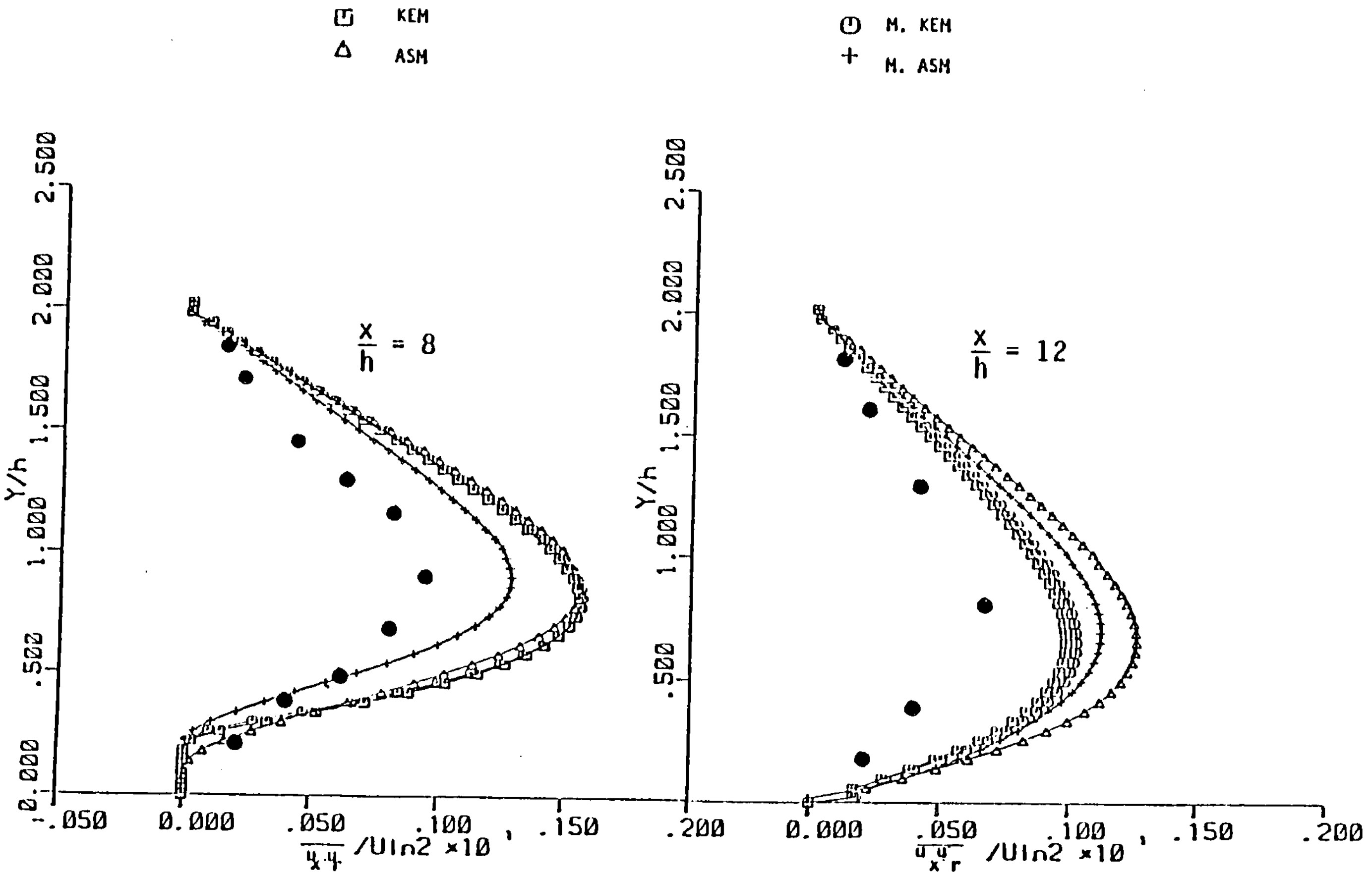

FIGURE 2.16, concluded. Comparison of Turbulence Model Predictions of Axial Reynolds Stress. Diameter Ratio 2.0 Axisymmetric Sudden Expansion. Data from Ref. 3.

Velocity and Shear Stress Profile Comparisons, Diameter Ratio = 1.33

At this diameter ratio, effects of pressure forces can be expected to be smaller than at a diameter ratio of 2.0 relative to the details of the turbulent mixing process, so that more substantial differences between turbulence model results than was evident in the diameter ratio 2.0 calculation may be expected.

The axial velocity profiles predicted by the four turbulence models considered in this work in the 1.33 diameter ratio case are shown in Figure 2.17 for x/h values of 2, 4, 6, 8, 10, and 14. There are no experimental data available for this diameter ratio. Within the recirculation region, excluding the immediate vicinity of the reattachment point, there appears to be no significant differences between the profiles as predicted by the four models. Beyond the recirculation region, the standard and "modified" versions of the ASM predict slightly larger centerline velocities which correspond to a slower rate of spread of the separated shear layer toward the centerline. This behavior is more pronounced for the "modified" ASM consistent with the larger recirculation zone this model predicts.

Similarly, small differences in model predictions are observed when the axial Reynolds shear stress component $\overline{u_x u_r}$ is examined, Figure 2.18. All four models predict similar $\overline{u_x u_r}$ profiles along the duct which only differ in magnitude. In the recirculation region, up to an x/h of 4, the highest stress levels are predicted by the KEM models. Here, the "modified" ASM predicts approximately 15% lower peak stress levels. Further downstream, the stress levels begin to decay. In this region, the standard and "modified" KEM models experience a more rapid decay, and eventually predict stress levels lower than both the "modified" and standard ASM. These results are also consistent with the $\overline{u_x u_r}$ predictions for the 2:1 diameter ratio.

Results for the diameter ratio 3.0 case are completely consistent with those already discussed for diameter ratios of 1.33 and 2.0 and are not presented herein.

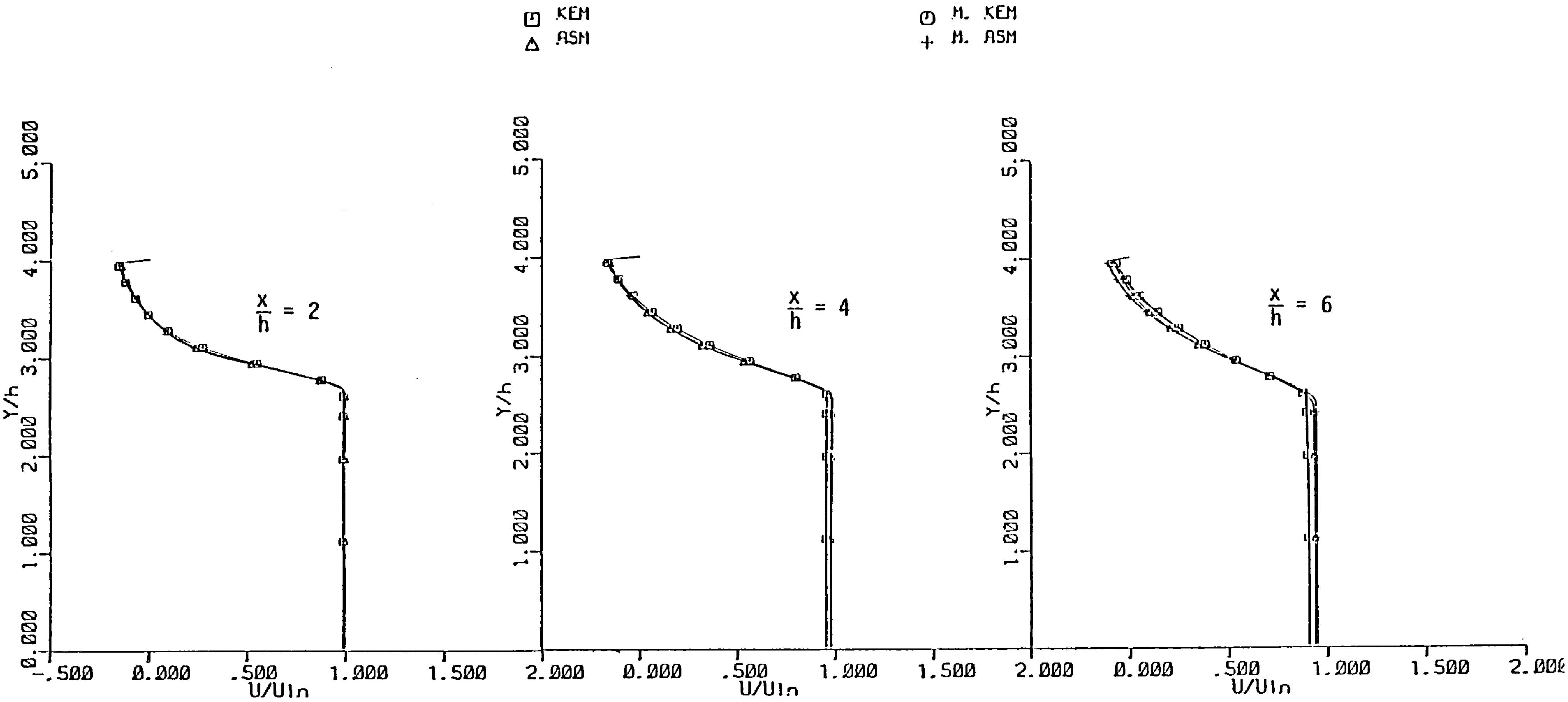

FIGURE 2.17. Comparison of Turbulence Model Predictions of Axial Velocity, Diameter Ratio 1.33 Axisymmetric Sudden Expansion.

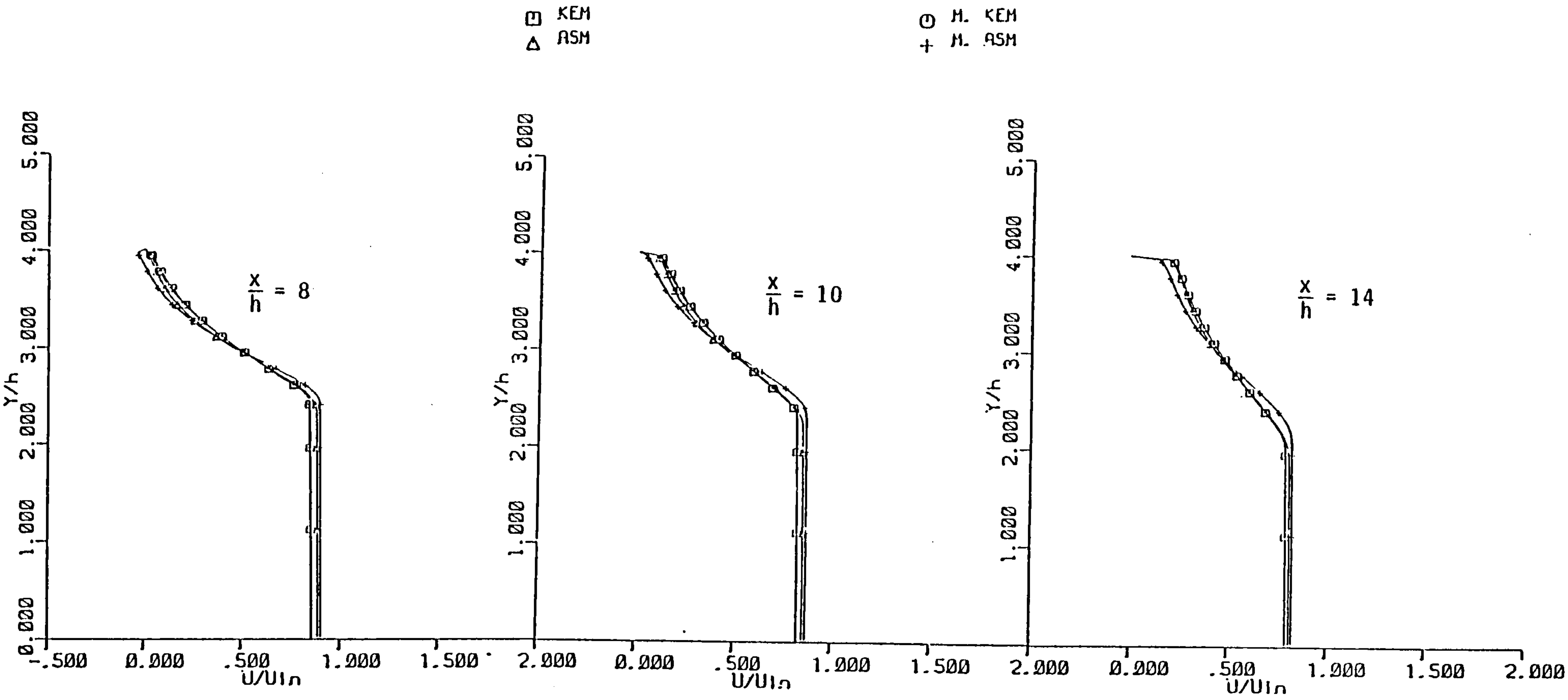

FIGURE 2.17, concluded. Comparison of Turbulence Model Predictions of Axial Velocity, Diameter Ratio 1.33 Sudden Expansion.

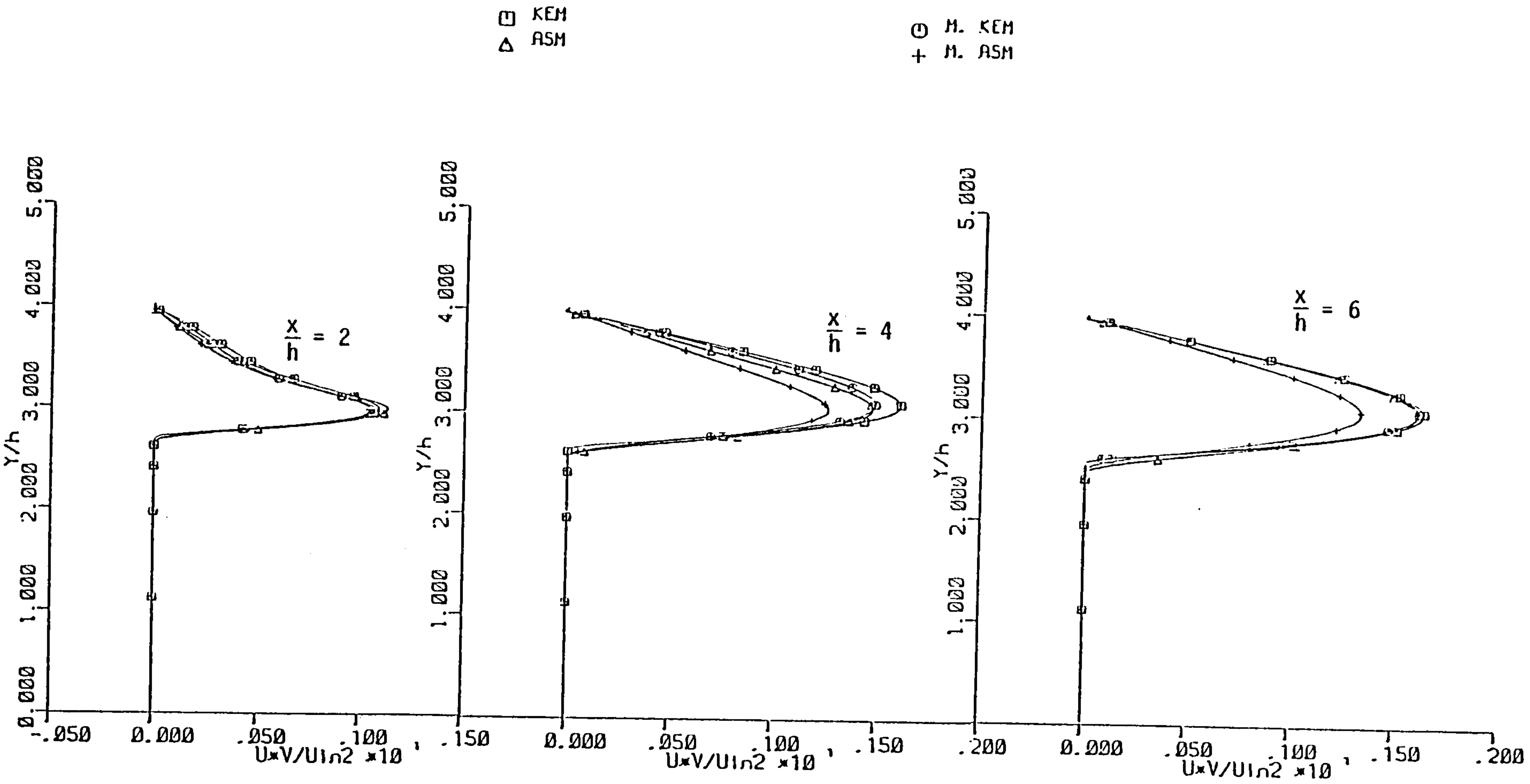

FIGURE 2.18. Comparison of Turbulence Model Predictions of Axial Reynolds Stress Component. Diameter Ratio 1.33 Axisymmetric Sudden Expansion.

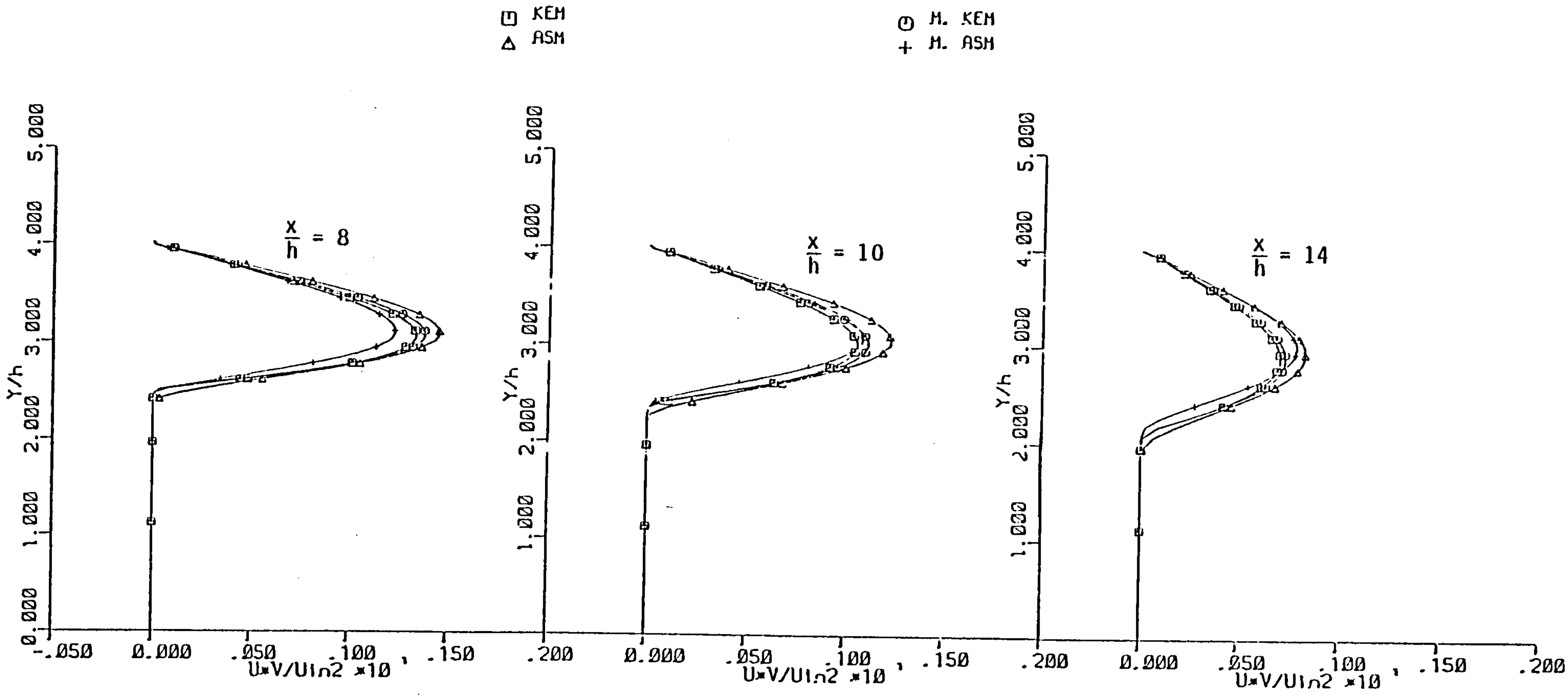

FIGURE 2.18, concluded. Comparison of Turbulence Model Predictions of Axial Reynolds Stress Component. Diameter Ratio 1.33 Axisymmetric Sudden Expansion.

Summary

The results of this assessment can be summarized as follows:

1, The mean velocity and turbulence field predictions do not change significantly with different turbulence models.

2. In these pressure dominated flows, simple k-ε model predictions appear to be comparable to the more sophisticated ASM computations.

3. At the lower diameter ratio, predictions seem to be more sensitive to modeling effects; however pressure forces still dominate the flowfield. The influence of these pressure forces can be appreciated by comparing the axisymmetric and planar reattachment length predictions at the same effective expansion ratio.

4. Performance of the "modified" ASM is consistent in both axisymmetric and planar sudden expansion flows. This model is, however, more sensitive to grid refinement in low diameter ratio axisymmetric flows. An increase in reattachment length of 15% is observed in axisymmetric flows over the standard version of the model as compared with a 28% increase in planar backward-facing step flows of the same expansion ratio.

3.0. ASSESSMENT OF TURBULENCE MODELS FOR SUBSONIC SWIRLING FLOWS

The results of comparisons of turbulence model predictions in axisymmetric sudden expansion do not produce a clear-cut choice among the turbulence models tested. This is partially due to the domination of the flowfield by the pressure forces, which reduces the sensitivity of the calculations to the turbulence models used, and partially to the lack of detailed experimental data for model evaluation. A more stringent test of model performance is the calculation of swirling axisymmetric sudden expansion flows where the swirl-induced flow anisotropy combined with the pressure forces generated by swirl create a more complicated flowfield for turbulence model assessment. While detailed experimental data are again lacking, and swirl flows are not of great interest in scramjet applications, assessment of model performance in highly swirling flows can provide some information on model behavior which can be of use in selecting a generally-useful model for scramjet applications. Thus modifications to the governing equations and the turbulence models for swirling flows were derived and implemented in the STEP codes. Fine grid calculations of a swirling flow of the constant angle type for a given swirl number were then carried out using the k-ε and algebraic stress models. The selection of the k-ε and algebraic stress models for this study is significant in that the algebraic stress model represents the only general purpose turbulence model outside a full Reynolds stress closure (where a differential transport equation has to be solved for each stress component) that does <u>not</u> use an isotropic turbulence viscosity concept.

3.1. GOVERNING EQUATIONS AND TURBULENCE MODEL FORMULATIONS FOR SWIRLING FLOWS

The governing equations of motion for turbulent axisymmetric swirling flows are

Conservation of Mass

$$\frac{\partial \rho}{\partial t} + \rho \left\{ \frac{\partial U}{\partial x} + \frac{1}{r} \frac{\partial}{\partial r} (rV) \right\} = 0 \qquad (1)$$

x-Momentum

$$\rho \frac{\partial U}{\partial t} + \rho U \frac{\partial U}{\partial x} + \rho V \frac{\partial U}{\partial r} = - \frac{\partial P}{\partial x} + \frac{\partial}{\partial x}\left[2\mu \frac{\partial U}{\partial x} - 2/3\mu\emptyset - \rho\overline{u^2}\right]$$

$$+ \frac{1}{r}\frac{\partial}{\partial r}\left[r\left\{\mu\left(\frac{\partial U}{\partial r} + \frac{\partial V}{\partial x}\right) - \rho\overline{uv}\right\}\right] \qquad (2a)$$

r-Momentum

$$\rho \frac{\partial V}{\partial t} + \rho U \frac{\partial V}{\partial x} + \rho V \frac{\partial V}{\partial r} - \rho \frac{W^2}{r} = - \frac{\partial P}{\partial r} + \frac{\partial}{\partial x}\left[\mu\left(\frac{\partial U}{\partial r} + \frac{\partial V}{\partial x}\right) - \rho\overline{uv}\right]$$

$$+ \frac{1}{r}\frac{\partial}{\partial r}\left[r\left\{2\mu \frac{\partial V}{\partial r} - 2/3\mu\emptyset - \rho\overline{v^2}\right\}\right]$$

$$- \frac{1}{r}\left[2\mu \frac{V}{r} - 2/3\mu\emptyset - \rho\overline{w^2}\right] \qquad (2b)$$

o-Momentum

$$\rho \frac{\partial W}{\partial t} + \rho U \frac{\partial W}{\partial x} + \rho V \frac{\partial W}{\partial r} + \rho \frac{VW}{r} = \frac{\partial}{\partial x}\left[\mu \frac{\partial W}{\partial x} - \rho\overline{uw}\right]$$

$$+ \frac{1}{r^2}\frac{\partial}{\partial r}\left[r^2\left\{\mu r \frac{\partial}{\partial r}\left(\frac{W}{r}\right) - \rho\overline{vw}\right\}\right] \qquad (2c)$$

$$\emptyset \equiv \frac{\partial U}{\partial x} + \frac{1}{r}\frac{\partial}{\partial r}(rV)$$

where U, V, W are the axial, radial and tangential components of the mean velocity, P is the pressure, ρ and μ are the fluid density and dynamic viscosity, respectively, and $\overline{u^2}$; $\overline{v^2}$; $\overline{w^2}$; $\overline{uv}$, $\overline{uw}$, $\overline{vw}$ are the Reynolds stresses. This set of equations, however, is not "closed" due to the appearance of the Reynolds stress tensor $\overline{u_i u_j}$ which introduces six additional unknowns to raise the total number of variables in the four equations to ten (U_i, P, $\overline{u_i u_j}$).

The k-ε and the algebraic stress models are used in this context to express $\overline{u_i u_j}$ in terms of known or calculable variables to "close" these equations.

k-ε Model

The k-ε model achieves closure by relating the Reynolds stresses to the mean strain rate through the Boussinesq approximation

$$- \rho \, \overline{u_i u_j} = \mu_t \left(\frac{\partial U_i}{\partial x_j} + \frac{\partial U_j}{\partial x_i} \right) - 2/3 \, \delta_{ij} \, \rho k \qquad (3)$$

The effective (turbulent or eddy) viscosity appearing above, μ_t, is defined in terms of a characteristic length and velocity. If this length is taken as the turbulence length scale, $k^{3/2}/\varepsilon$, and the velocity as $k^{\frac{1}{2}}$, μ_t can be expressed as

$$\mu_t \equiv c_\mu \rho \, k^2/\varepsilon \qquad (4)$$

where k is the turbulence kinetic energy, ε is the dissipation rate and c_μ is a constant of proportionality. The Reynolds stresses are then defined as

$$- \rho \, \overline{u^2} = 2\mu_t \frac{\partial U}{\partial x} - 2/3 \rho k \qquad (5)$$

$$- \rho \, \overline{v^2} = 2\mu_t \frac{\partial V}{\partial r} - 2/3 \rho k \qquad (6)$$

$$- \rho \, \overline{w^2} = 2\mu_t \frac{W}{r} - 2/3 \rho k \qquad (7)$$

$$- \rho \overline{uv} = \mu_t \left(\frac{\partial U}{\partial r} + \frac{\partial V}{\partial x} \right) \qquad (8)$$

$$- \rho \overline{uw} = \mu_t \frac{\partial W}{\partial x} \qquad (9)$$

$$- \rho \overline{vw} = \mu_t \, r \frac{\partial}{\partial r} \left(\frac{W}{r} \right) \qquad (10)$$

for swirling axisymmetric flows. Note that the same single value of μ_t appears in all of the Reynolds stress relationships: this is the isotropic viscosity assumption.

Algebraic Stress Model

A complete second-order closure of the Reynolds-averaged governing equations would require the solution of a transport equation for each of the stress components. Even for two-dimensional flows this can be a formidable task, since, in addition to the mean flow equations (equations (1) and (2)), eight other transport equations (for $\overline{u}$, $\overline{v}$, $\overline{w}$, $\overline{uv}$, $\overline{uw}$, $\overline{vw}$, k, and ε) need to be solved. Under the assumption that the convection and diffusion of each Reynolds stress component can be related to the convection and diffusion of turbulent kinetic energy, however, the stress transport equations can be reduced to a set of implicit algebraic expressions for the stresses in terms of the mean strain rate, turbulent kinetic energy, dissipation rate, and the stresses themselves. The equation for the algebraic stress model for a swirling flow, including the near-wall correction terms are

$$\overline{u_i u_j} = \frac{k}{(P-\varepsilon)} \left(P_{ij} - \frac{2}{3} \delta_{ij}\varepsilon + \phi_{ij,1} + \phi_{ij,2} + \phi'_{ij,1} + \phi'_{ij,2} \right) \qquad (11)$$

where

$P = -\overline{u_i u_k} \dfrac{\partial U_i}{\partial x_k}$, the production rate of kinetic energy

$P_{ij} = -\left(\overline{u_i u_k} \dfrac{\partial U_j}{\partial x_k} + \overline{u_j u_k} \dfrac{\partial U_i}{\partial x_k} \right)$, the production rate of individual Reynolds stresses

$\phi_{ij,1} = -c_1 \varepsilon/k \left(\overline{u_i u_j} - 2/3\, \delta_{ij}\, k \right)$, the modeled form of the contribution of fluctuating quantities to the pressure-strain correlation

$\phi_{ij,2} = -c_2 \left(P_{ij} - 2/3\, \delta_{ij}\, P \right)$, the modeled form of the contribution of mean strain effects to the pressure-strain correlation

$\phi'_{ij,1} = c'_1\, \varepsilon/k \left(\overline{u_k u_m}\, n_k n_m\, \delta_{ij} - 3/2\, \overline{u_k u_j}\, n_k n_i - 3/2\, \overline{u_k u_i}\, n_k n_j \right) \; f\left(\dfrac{\ell}{n_i r_i} \right)$, wall correction to $\phi_{ij,1}$

$$\phi'_{ij,2} = c'_2 \left(\phi_{km,2}\, n_k n_m\, \delta_{ij} - 3/2\, \phi_{ik,2}\, n_k n_j - 3/2\, \phi_{jk,2}\, n_k n_i \right) f\left(\ell / n_i r_i\right),$$

wall correction to $\phi_{ij,2}$

$f\left(\dfrac{\ell}{n_i r_i}\right)$ is the length scale function.

Equation (11) is the version of the algebraic stress model used in this study. The details of the derivation and the underlying assumptions for the model are discussed in Ref. 2.

For axisymmetric swirling flows the algebraic stress model representation of the Reynolds stresses become

$$\begin{aligned}
-\rho\overline{u^2} = \Gamma\Big[& \left(2 + 4a_{1x} + a_{1r}\right)\left(e_u + 2/3\right) \frac{\partial U}{\partial x} + 3a_{2x}\left(e_u + 2/3\right) \\
& - \left(1 + 2a_{1x} + 2a_{1r}\right)\left(e_v + 2/3\right) \frac{\partial V}{\partial r} - 1.5a_{2r}\left(e_v + 2/3\right) \\
& - \left(1 + 2a_{1x} - a_{1r}\right)\left(e_w + 2/3\right) \frac{V}{r} \\
& + \left(2 + 4a_{1x} + a_{1r}\right)\left(e_{uv}\right) \frac{\partial U}{\partial r} - \left(1 + 2a_{1x} + 2a_{1r}\right)\left(e_{uv}\right) \frac{\partial V}{\partial x} \\
& - \left(1 + 2a_{1x} - a_{1r}\right)\left(e_{uw}\right) \frac{\partial W}{\partial x} \\
& - \left(1 + 2a_{1x} - a_{1r}\right)\left(e_{vw}\right)\left(\frac{\partial W}{\partial r} - \frac{W}{r}\right) \Big] - 2/3\,\rho k
\end{aligned} \qquad (12)$$

$$\begin{aligned}
-\rho\overline{v^2} = \Gamma\Big[& -\left(1 + 2a_{1x} + 2a_{1r}\right)\left(e_u + 2/3\right) \frac{\partial U}{\partial x} - 1.5a_{2x}\left(e_u + 2/3\right) \\
& + \left(2 + a_{1x} + 4a_{1r}\right)\left(e_v + 2/3\right) \frac{\partial V}{\partial r} + 3a_{2r}\left(e_v + 2/3\right) \\
& - \left(1 - a_{1x} + 2a_{1r}\right)\left(e_w + 2/3\right) \frac{V}{r} \\
& - \left(1 + 2a_{1x} + 2a_{1r}\right)\left(e_{uv}\right) \frac{\partial U}{\partial r} + \left(2 + a_{1x} + 4a_{1r}\right)\left(e_{uv}\right) \frac{\partial V}{\partial x} \\
& - \left(1 - a_{1x} + 2a_{1r}\right)\left(e_{uw}\right) \frac{\partial W}{\partial x} \\
& - \left(1 - a_{1x} + 2a_{1r}\right)\left(e_{vw}\right)\left(\frac{\partial W}{\partial r} - \frac{W}{r}\right) \Big] - 2/3\,\rho k
\end{aligned} \qquad (13)$$

$$\begin{aligned}
-\rho\overline{w^2} = \Gamma \Big[& -\left(1 + 2a_{1x} - a_{1r}\right)\left(e_u + 2/3\right)\frac{\partial U}{\partial x} - 1.5\left(e_u + 2/3\right)a_{2x} \\
& -\left(1 - a_{1x} + 2a_{1r}\right)\left(e_v + 2/3\right)\frac{\partial V}{\partial r} - 1/5\left(e_v + 2/3\right)a_{2r} \\
& +\left(2 + a_{1x} + a_{1r}\right)\left(e_w + 2/3\right)\frac{V}{r} \\
& -\left(1 + 2a_{1x} + a_{1r}\right)\left(e_{uv}\right)\frac{\partial U}{\partial r} - \left(1 - a_{1x} + 2a_{1r}\right)\left(e_{uv}\right)\frac{\partial V}{\partial x} \\
& +\left(2 + a_{1x} + a_{1r}\right)\left(e_{uw}\right)\frac{\partial W}{\partial x} \\
& +\left(2 + a_{1x} + a_{1r}\right)\left(e_{vw}\right)\left(\frac{\partial W}{\partial r} - \frac{W}{r}\right)\Big] - 2/3\,\rho k
\end{aligned} \qquad (14)$$

$$\begin{aligned}
-\rho\overline{uv} = \; & \Gamma\Big[1.5\left(1 + 1.5a_{1x} + 1.5a_{1r}\right)\left(e_u + 2/3\right)\frac{\partial V}{\partial x} \\
& + 1.5\left(1 + 1.5a_{1x} + 1.5a_{1r}\right)\left(e_v + 2/3\right)\frac{\partial U}{\partial r} \\
& - 1.5\left(1 + 1.5a_{1x} + 1.5a_{1r}\right)\left(e_{uv}\right)\frac{V}{r} + 2.25\left(a_{2x} + a_{2r}\right)\left(e_{uv}\right)\Big]
\end{aligned} \qquad (15)$$

$$\begin{aligned}
-\rho\overline{uw} = \; & \Gamma\Big[1.5\left(1 + 1.5a_{1x}\right)\left(e_u + 2/3\right)\frac{\partial W}{\partial x} \\
& + 1.5\left(1 + 1.5a_{1x}\right)\left(e_{uv}\right)\left(\frac{\partial W}{\partial r} - \frac{W}{r}\right) \\
& + 1.5\left(1 + 1.5a_{1x}\right)\left(e_{uw}\right)\left(\frac{\partial U}{\partial x} + \frac{V}{r}\right) + 2.25\left(a_{2x}\right)\left(e_{uw}\right) \\
& + 1.5\left(1 + 1.5a_{1x}\right)\left(e_{vw}\right)\frac{\partial U}{\partial r}\Big]
\end{aligned} \qquad (16)$$

$$\begin{aligned}
-\rho\overline{vw} = \; & \Gamma\Big[1.5\left(1 + 1.5a_{1r}\right)\left(e_v + 2/3\right)\left(\frac{\partial W}{\partial r} - \frac{W}{r}\right) \\
& + 1.5\left(1 + 1.5a_{1r}\right)\left(e_{uv}\right)\frac{\partial W}{\partial x} \\
& + 1.5\left(1 + 1.5a_{1r}\right)\left(e_{uw}\right)\frac{\partial V}{\partial x} \\
& + 1.5\left(1 + 1.5a_{1r}\right)\left(e_{vw}\right)\left(\frac{\partial V}{\partial r} + \frac{V}{r}\right) + 2.25\left(a_{2r}\right)\left(e_{vw}\right)\Big]
\end{aligned} \qquad (17)$$

where

$$\Gamma_1 \equiv 2/3\ \lambda k/\varepsilon \qquad \Gamma \equiv 2/3\ \rho\lambda k^2/\varepsilon$$

$$\lambda \equiv (1 - c_2)\ /\ ((c_1 - 1)\ + P/\varepsilon\ )$$

$$a_{1x} \equiv c_2 c_2'\ \zeta_x/\ (1 - c_2) \qquad a_{1r} \equiv c_2 c_2'\ \zeta_r/(1 - c_2)$$

$$a_{2x} \equiv c_1'\ \varepsilon/k\ \zeta_x/(1 - c_2) \qquad a_{2r} \equiv c_1'\ \varepsilon/k\ \zeta_r/(1 - c_2)$$

$$f_x \equiv \frac{k^{3/2}/\varepsilon}{K/a^{3/2}x} \qquad f_r \equiv \frac{k^{3/2}/\varepsilon}{K/a^{3/2}r}$$

c_1, c_2, c_1', and c_2' are constants defined in Table 2.6, K is the von Karman constant (0.4187) and "a" is the near-wall value of $-\overline{uv}/k$ (generally taken as 0.25).

TABLE 3.1 Recommended Values for Turbulence Model Constants

K	$= 0.4187$	c_k	$= 0.22$
c_μ	$= 0.09$	c_{ε_3}	$= 0.36\ (c_{\varepsilon_2} - c_{\varepsilon_1})$
σ_k	$= 1.00$	c_1	$= 1.8$
σ_ε	$= k^2/(c_{\varepsilon_2} - c_{\varepsilon_1})c_{\mu-}^{1/2}$	c_2	$= 0.6$
c_{ε_1}	$= 1.44$	c_1'	$= 0.5$
c_{ε_2}	$= 1.92$	c_2'	$= 0.3$

k and ε Transport Equations

Both the k-ε eddy viscosity and the algebraic stress model require evaluation of the turbulent kinetic energy and its dissipation rate to define turbulent time and length scales. The high Reynolds number forms of the k and ε transport equations used in this study are

$$\rho \frac{\partial k}{\partial t} + \rho U \frac{\partial k}{\partial x} + \rho V \frac{\partial k}{\partial r} = \rho P - \rho \varepsilon + \frac{\partial}{\partial x} D_{k_x} + \frac{1}{r} \frac{\partial}{\partial r} \left(r D_{k_r} \right) \tag{18}$$

$$\rho \frac{\partial \varepsilon}{\partial t} + \rho U \frac{\partial \varepsilon}{\partial x} + \rho V \frac{\partial \varepsilon}{\partial r} = \rho\, \varepsilon / k \left(c_{\varepsilon_1} P - c_{\varepsilon_2} \varepsilon \right) + \frac{\partial}{\partial x} D_{\varepsilon_x} + \frac{1}{r} \frac{\partial}{\partial r} \left(r D_{\varepsilon_r} \right) \tag{19}$$

where

k-ε Model

$$D_{k_x} = \left(\frac{\mu_t}{\sigma_k} + \mu \right) \frac{\partial k}{\partial x} \tag{20}$$

$$D_{k_r} = \left(\frac{\mu_t}{\sigma_k} + \mu \right) \frac{\partial k}{\partial r} \tag{21}$$

$$D_{\varepsilon_x} = \left(\frac{\mu_t}{\sigma_\varepsilon} + \mu \right) \frac{\partial \varepsilon}{\partial x} \tag{22}$$

$$D_{\varepsilon_r} = \left(\frac{\mu_t}{\sigma_\varepsilon} + \mu \right) \frac{\partial \varepsilon}{\partial r} \tag{23}$$

$$\begin{aligned} P \equiv\; & \frac{\mu_t}{\rho} \left[2 \left\{ \left(\frac{\partial U}{\partial x} \right)^2 + \left(\frac{V}{r} \right)^2 + \left(\frac{\partial V}{\partial r} \right)^2 \right\} + \left(\frac{\partial U}{\partial r} + \frac{\partial V}{\partial x} \right)^2 \right. \\ & \left. + \left(r \frac{\partial}{\partial r} \left(\frac{W}{r} \right) \right)^2 + \left(\frac{\partial W}{\partial x} \right)^2 \right] - 2/3\, k \left[\frac{\partial U}{\partial x} + \frac{V}{r} + \frac{\partial V}{\partial r} \right] \end{aligned} \tag{24}$$

σ_k and σ_ε are turbulent Prandtl numbers for k and ε respectively. These are defined in Table 2.6 with model constants c_{ε_1} and c_{ε_2}.

Algebraic Stress Model

$$\mathcal{D}_{k_x} = c_k \frac{k}{\varepsilon} \left\{ \overline{u^2}\frac{\partial k}{\partial x} + \overline{uv}\frac{\partial k}{\partial r} \right\} + \mu \frac{\partial k}{\partial x} \tag{25}$$

$$\mathcal{D}_{k_r} = c_k \frac{k}{\varepsilon} \left\{ \overline{v^2}\frac{\partial k}{\partial r} + \overline{uv}\frac{\partial k}{\partial x} \right\} + \mu \frac{\partial k}{\partial r} \tag{26}$$

$$\mathcal{D}_{\varepsilon_x} = c_{\varepsilon_3} \frac{k}{\varepsilon} \left\{ \overline{u^2}\frac{\partial \varepsilon}{\partial x} + \overline{uv}\frac{\partial \varepsilon}{\partial r} \right\} + \mu \frac{\partial \varepsilon}{\partial x} \tag{27}$$

$$\mathcal{D}_{\varepsilon_r} = c_{\varepsilon_3} \frac{k}{\varepsilon} \left\{ \overline{v^2}\frac{\partial \varepsilon}{\partial r} + \overline{uv}\frac{\partial \varepsilon}{\partial x} \right\} + \mu \frac{\partial \varepsilon}{\partial r} \tag{28}$$

$$\begin{aligned} \mathcal{P} \equiv & - \left\{ \overline{u^2}\frac{\partial U}{\partial x} + \overline{v^2}\frac{\partial V}{\partial r} + \overline{w^2}\frac{V}{r} + \overline{uv}\left(\frac{\partial U}{\partial r} + \frac{\partial V}{\partial x}\right) \right. \\ & \left. + \overline{uw}\frac{\partial W}{\partial x} + \overline{vw}\left[r \frac{\partial}{\partial r} \left(\frac{W}{r}\right)\right] \right\} \end{aligned} \tag{29}$$

c_k and c_{ε_3} are model constants given in Table 2.6.

Wall Function Treatment

Most turbulence models including the present versions of the algebraic stress and k-ε models are devices for high Reynolds number flows. However, in the vicinity of solid boundaries where the velocities are small, the low Reynolds number effects previously neglected become significant and should be accounted for. This can be accomplished either by solving the low Reynolds number form of the transport equations or by developing wall functions that introduce these effects into the existing high Reynolds number models. Chieng and Launder (Ref. 12) found that the first option required vast amounts of computer time due to the slow convergence characteristics of the low Reynolds number models. On the other hand a new wall function treatment proposed by the same authors was shown to incorporate these effects with practically no increase in computing time. An expanded version of this treatment is used in the present study. Details of this approach are given in Ref. 3.

3.2 MODEL ASSESSMENT IN SUBSONIC SWIRLING FLOWS

Model assessment for swirling flow computations was carried out through fine grid calculations of a constant angle swirl flow at a swirl number of 2. Swirling flows are usually characterized by defining a swirl number which is the ratio of the axial flux of tangential momentum to the axial flux of axial momentum times the inlet radius. The definition of the swirl number is then

$$S \equiv \frac{G_\phi}{G_x R_i} \tag{30}$$

where

$$G_\phi = \int_R^{R_i} (Wr)\, \rho U\, 2\pi r\, dr$$

$$G_x = \int_R^{R_i} (U\rho)\, U\, 2\pi r\, dr + \int_R^{R_i} P\, 2\pi r\, dr$$

U = Axial velocity component

W = Tangential velocity component

R = Inner radius (hubbed swirlers)

R_i = Inlet radius

ρ = Local density

P = Local static pressure

A number of flow phenomena are related to and affected by the presence of strong swirling in combustor flows. These phenomena are complexly interrelated and can have profound effects on performance parameters such as combustion efficiency, pressure losses, flammability limits, combustion flow stability, and nozzle thrust losses. While a swirl number of 2 is extremely high from the standpoint of practical combustor flows, assessment of turbulence models in high swirl number non-reacting swirling flows provides a useful step in developing turbulence modeling for complex flows, for at high swirl numbers the differences between models are maximized. This suggests the utility of experiments run at swirl numbers that would otherwise be of little interest from a propulsion system standpoint.

Two-equation (k-ε) model and algebraic stress model calculations were carried out for a uniform density flow in a 2:1 diameter ratio sudden expansion with and without swirl. The computational domain and flow parameters for these calculations were as shown in Figure 2.19: inlet swirl was of the constant-angle type. No separate grid-refinement tests were conducted for these calculations; however, based on the criteria given in Section 2.1.1, these results should not be significantly affected by numerical diffusion.

The effects of swirl on the overall flowfield at this swirl number is demonstrated by the streamfunction plots given in Figures 2.20 and 2.21. The formation of a large centerline recirculation zone and the enhanced radial mixing shown are both direct consequences of the axial momentum deficit created by the non-zero tangential component of the mean velocity. Significant differences between the k-ε and the algebraic stress models appear only in the swirling flow calculations. This supports the hypothesis noted earlier that the two models would show a different sensitivity to flow anisotropy, induced, in this case, by swirl. While detailed experimental data does not exist for this configuration, experiments such as those discussed in Ref. 13 indicate very large centerline recirculation regions at high swirl numbers, indirectly supporting the ASM prediction of the swirling flow. It might also be noted that a large recirculation region along the centerline such as seen in Figure 2.21 would be unstable to small disturbances (and thus would be subject to axial position fluctuations) (Ref. 13). Note further that near the wall the predicted flowfields are very similar, so that measurements of, for example, static pressure distribution would not necessarily reflect the large centerline differences between these flows. Thus detailed measurements within the flowfield will be required to provide data with which to directly test the models.

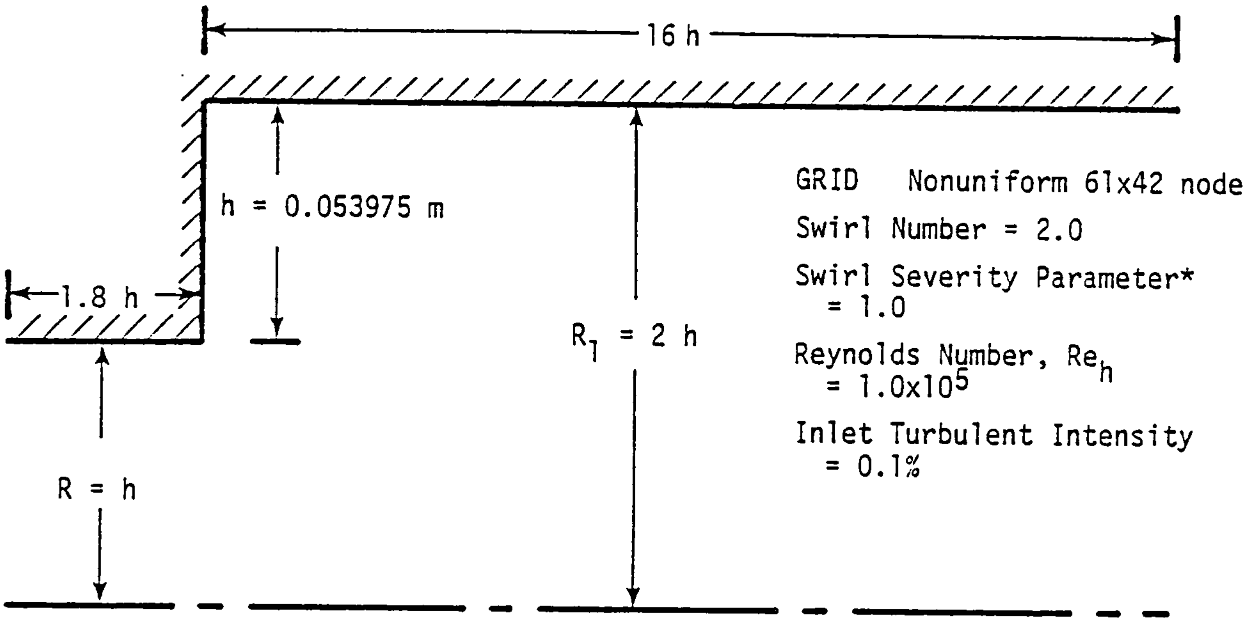

FIGURE 3.1. Computation Domain and Flow Parameter.

---

[*] Swirl severity parameter is the ratio of the maximum tangential velocity component to the maximum axial velocity component.

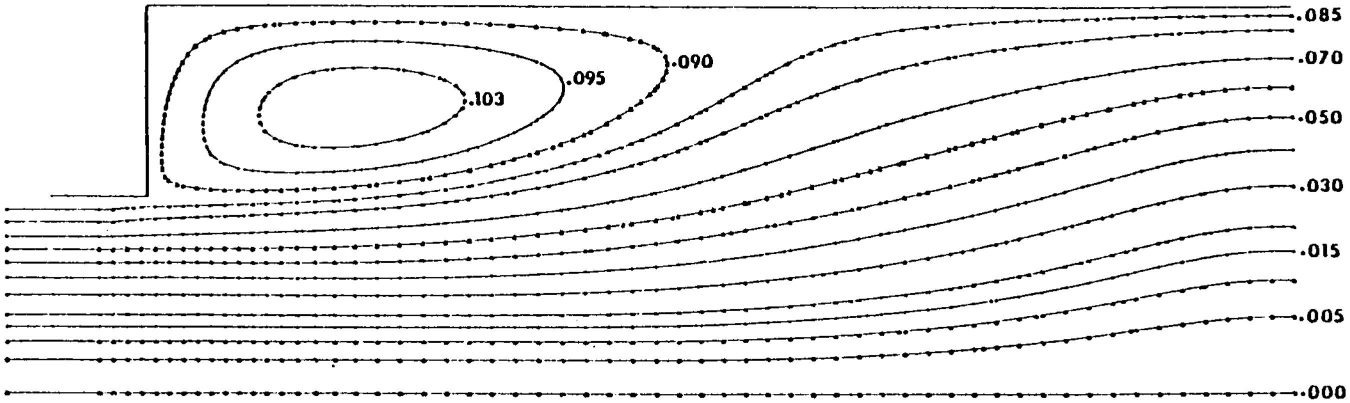

(a) no swirl

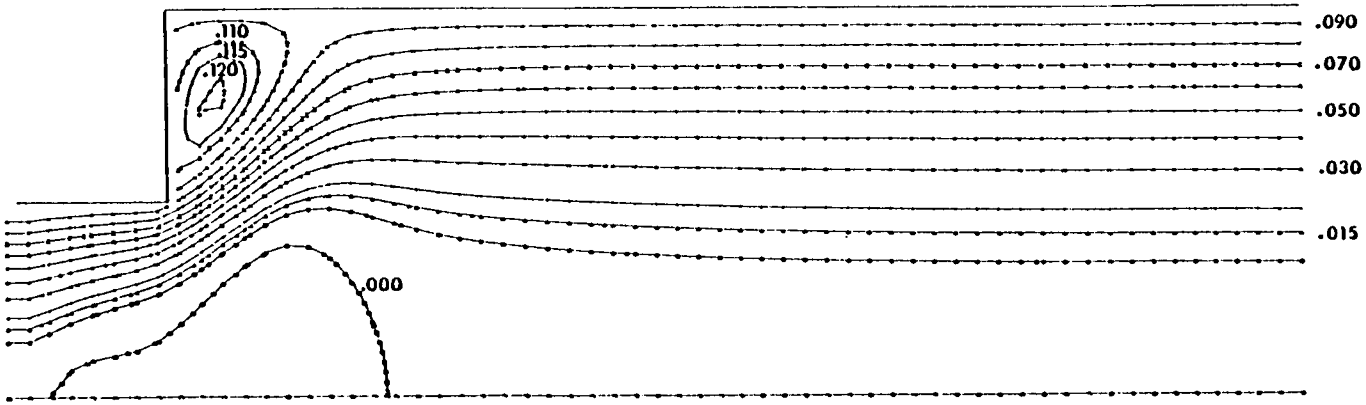

(b) constant angle swirl, S=2.0

FIGURE 3.2. Stream Function Calculations with the k-ε Model.

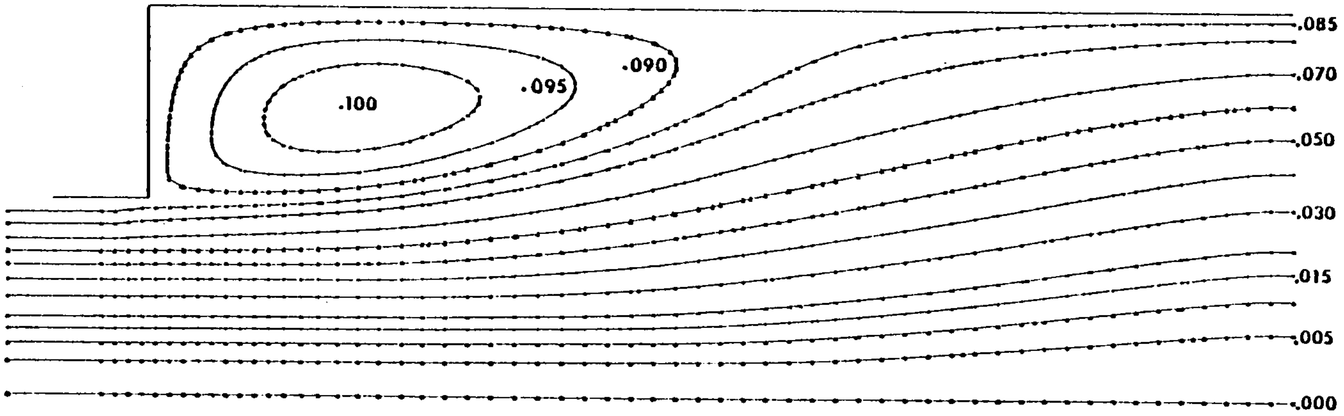

(a) no swirl

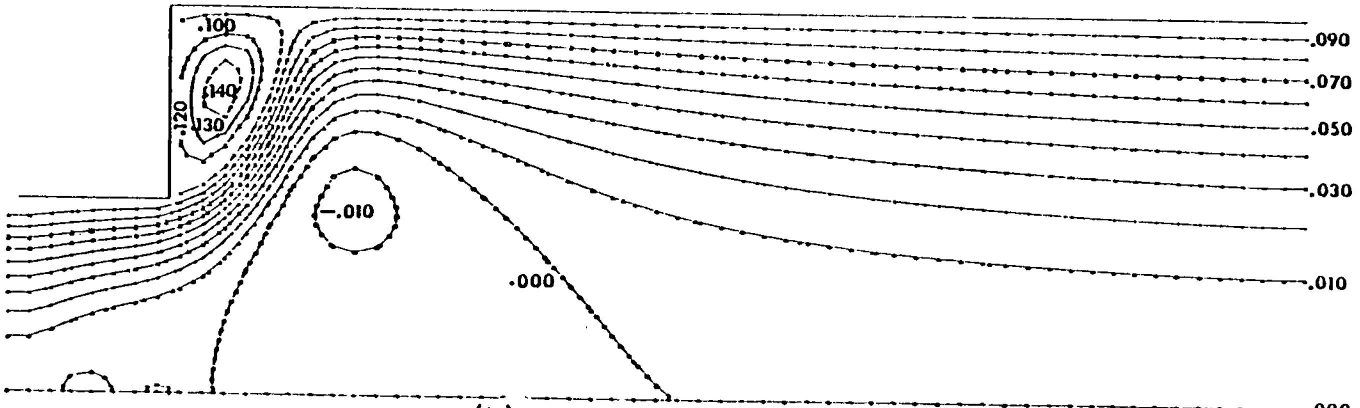

(b) constant angle swirl, S=2.0

FIGURE 3.3. Stream Function Calculations with the Algebraic Stress Model.

The axial velocity profiles shown by Figure 3.4 compare the swirl and the no swirl cases for the two models. The k-ε model predictions indicate a large (4.68 step heights long) irregularly shaped centerline recirculation region shown in Figue 3.2 that extends well into the inlet and appears to signal an eventual breakdown on the existing vortex at higher swirl intensities. The algebraic stress model calculations on the other hand show an actual breakdown of the centerline recirculation region into three discrete vortices -- two small eddies appear in the inlet and a large primary eddy (6.37 step heights long) is positioned roughly 0.76 step height downstream of the expansion plane (Figure 3.3). The tangential velocity profiles presented in Figure 3.5 show the same qualitative behavior for both models, however, the magnitude of the velocities are significantly lower for the algebraic stress model. The turbulent kinetic enery distributions plotted in Figure 3.6 also show roughly the same behavior for both models; here, however, the algebraic stress model predicts significantly higher levels of turbulence intensity along the combustor axis. The Reynolds shear stress profiles given in Figure 3.7 appear quite similar with the k-ε model, predicting slightly higher stress levels in the near-field flow and the algebraic stress model further downstream. These predictions are consistent with the flow pattern depicted in Figures 3.2 and 3.3.

Summary

The computations just described show that significant differences between the k-ε and ASM models exist in flows in which anisotropic viscosity effects can be expected. For flows in which there is only one major shear stress component, such as the conventional sudden expansion in regions away from the recirculation zone the additional complexity involved in the ASM formulation may not be warranted. Note, however, that even in simpler flows there are regions in which secondary shear stress components may be nonnegligible. Just such a region is the near-corner region, and it will be recalled that in this region the ASM formulation indicates a larger secondary eddy than does the k-ε approach.

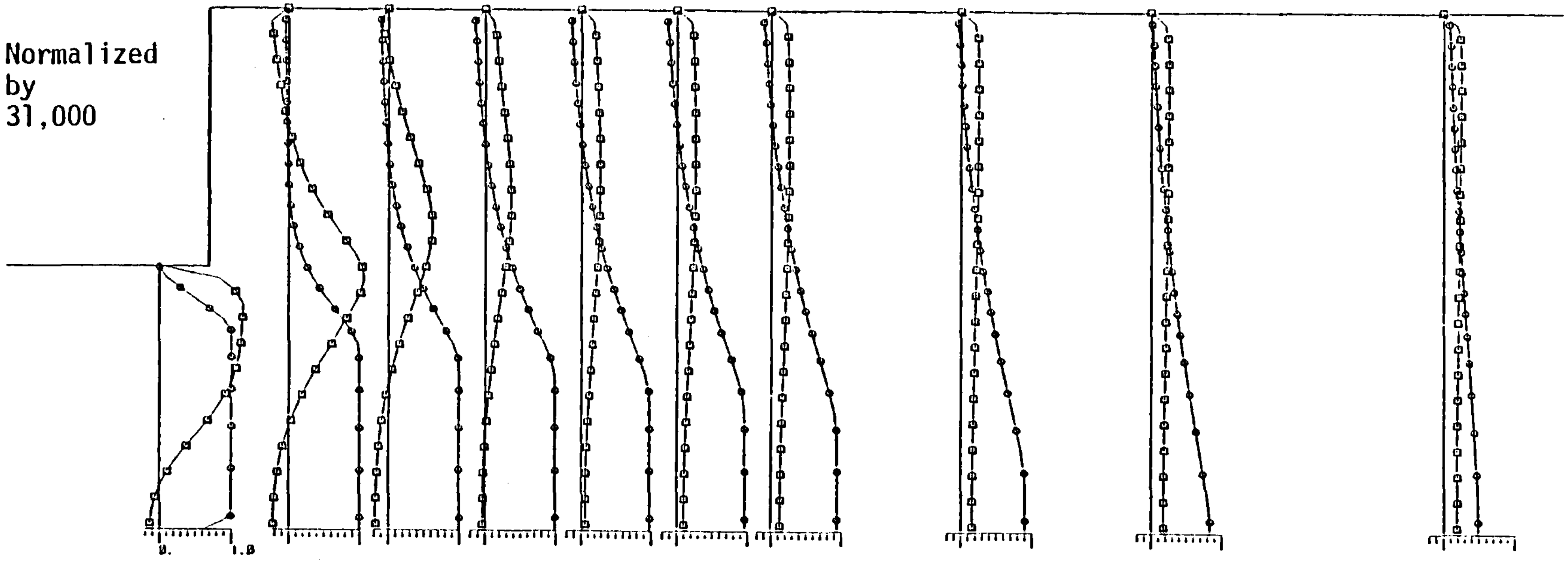

(a) KEM Predictions

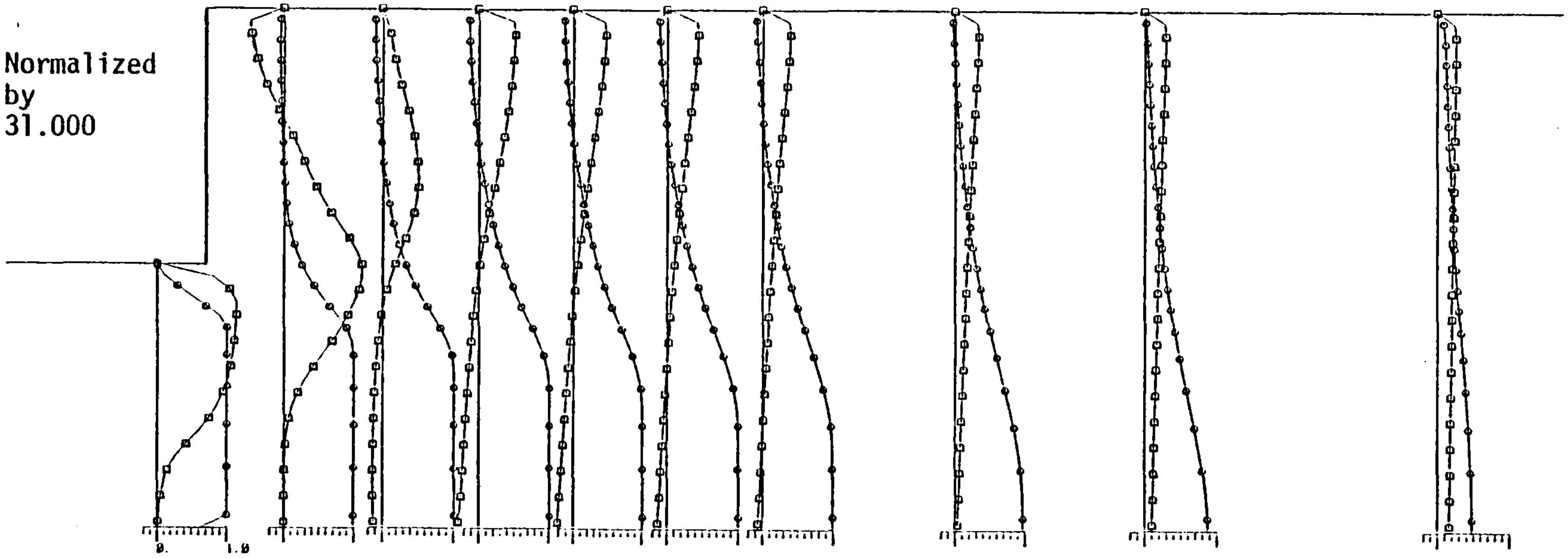

(b) ASM Predictions

FIGURE 3.4. U-Velocity Profiles.

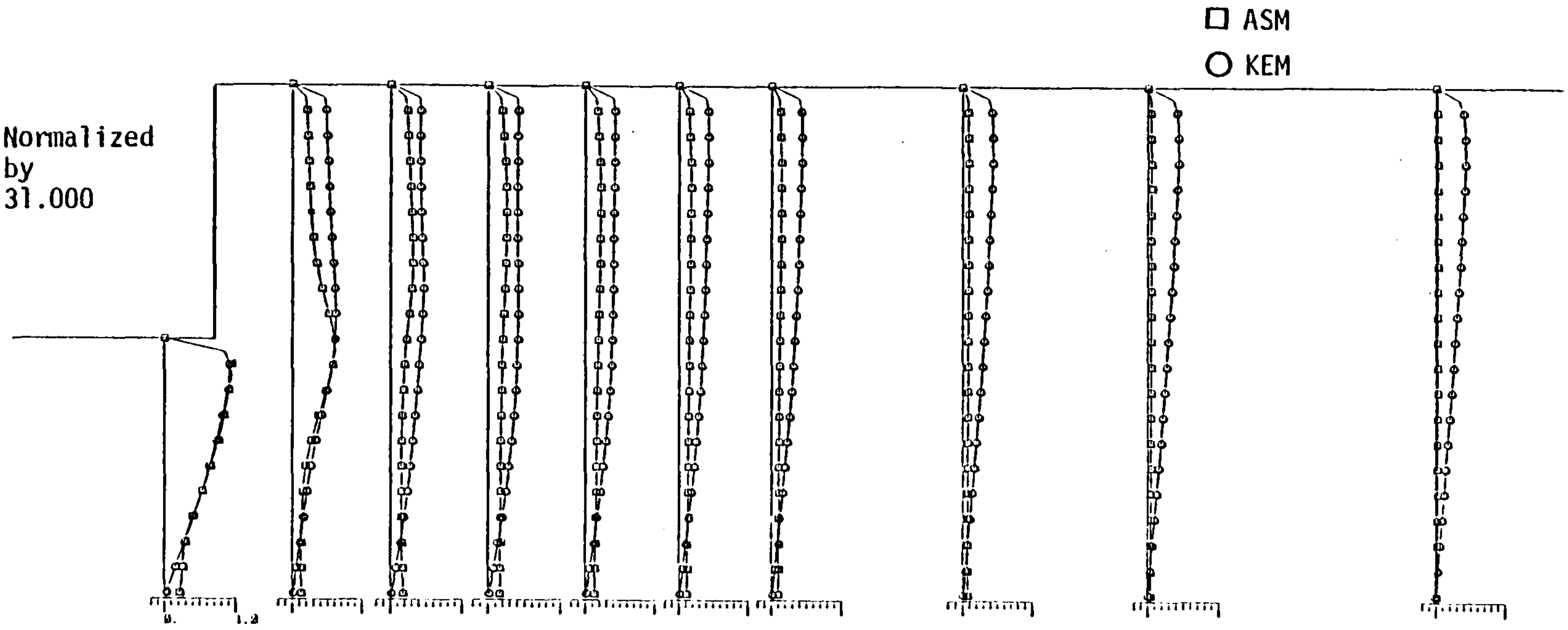

FIGURE 3.5. W-Velocity Profiles

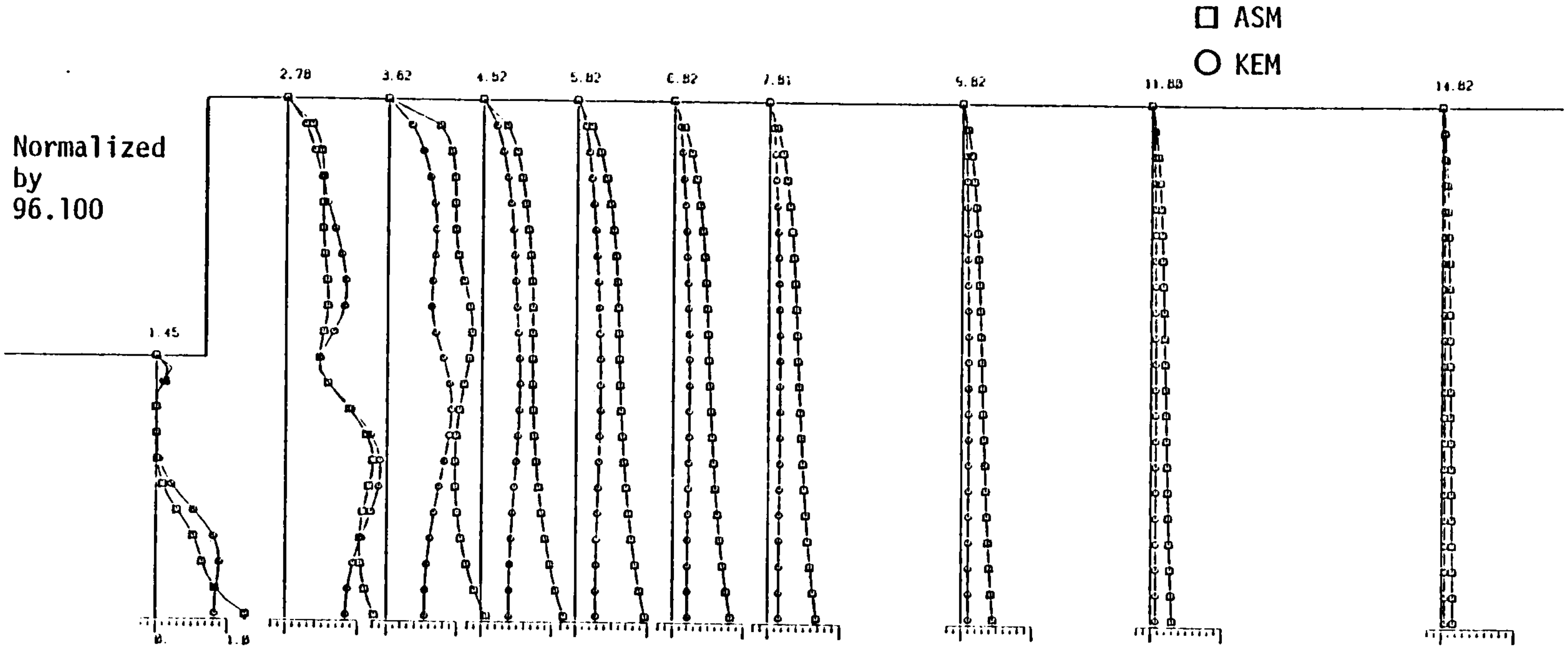

FIGURE 3.6. k Profiles.

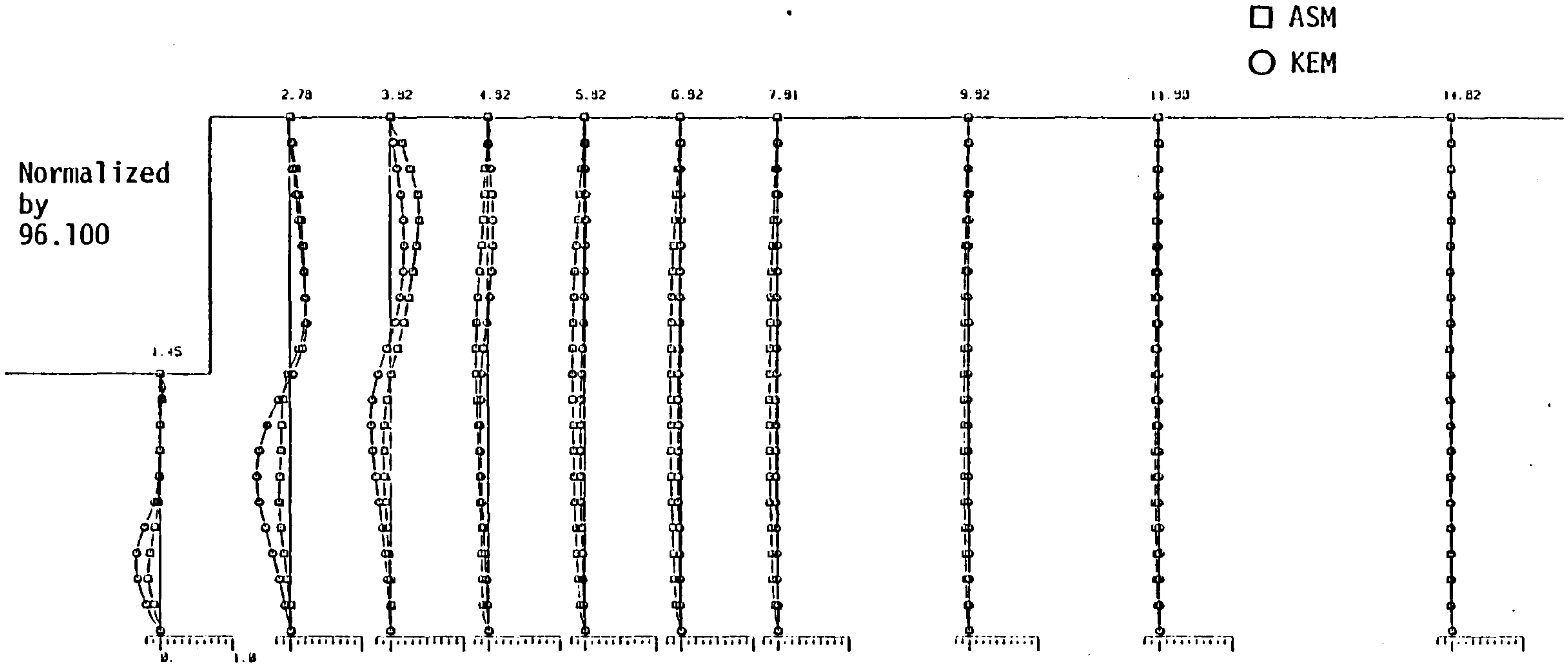

FIGURE 3.7. $\overline{uv}$ Profiles.

4.0. ASSESSMENT OF TURBULENCE MODELS FOR SUPERSONIC RECIRCULATING FLOWS

Previous efforts (Ref. 2) to incorporate the k-ε model in to the TWODLE code of J.P. Drummond (Ref. 14) for supersonic recirculating flow calculations were hindered by numerical stability problems. Eventually, a scheme was devised that appeared to be stable but required very small time steps due to the explicit nature of the technique. In addition, the fact that the k and ε transport equations were solved in the physical coordinates introduced inaccuracies for irregular geometries. Two options were available: modify this scheme so that the k and ε equations are solved implicity and simultaneously in the transformed coordinates, or implement the k-ε model in a new implicit version of the TWODLE code (Ref. 14) that does not use time-split finite differencing. The second option was investigated as part of this year's work.

4.1. GOVERNING EQUATIONS AND WALL FUNCTIONS

Mean Flow and Turbulence Equations

The mean flow and turbulence model equations for the k-ε model can be written as follows for two-dimensional elliptic planar flows:

Conservation of Mass

$$\frac{\partial \rho}{\partial t} + \frac{\partial}{\partial x} \rho U + \frac{\partial}{\partial x} \rho V = 0 \qquad (31)$$

x-Momentum

$$\begin{aligned}
&\frac{\partial}{\partial t} \rho U + \frac{\partial}{\partial x} \rho U^2 + \frac{\partial}{\partial y} \rho UV \\
&= - \frac{\partial P}{\partial x} + \frac{\partial}{\partial x}\left[2\mu_T \frac{\partial U}{\partial x} - 2/3\mu_T\left(\frac{\partial U}{\partial x} + \frac{\partial V}{\partial y}\right) - 2/3\rho k\right] + \frac{\partial}{\partial y}\left[\mu_T\left(\frac{\partial U}{\partial y} + \frac{\partial V}{\partial x}\right)\right]
\end{aligned} \qquad (32)$$

y-Momentum

$$\frac{\partial \rho V}{\partial t} + \frac{\partial}{\partial x}\rho UV + \frac{\partial}{\partial y}\rho V^2$$

$$= -\frac{\partial P}{\partial y} + \frac{\partial}{\partial x}\left[\mu_T\left(\frac{\partial U}{\partial y} + \frac{\partial V}{\partial x}\right)\right] + \frac{\partial}{\partial y}\left[2\mu_T\frac{\partial V}{\partial y} - 2/3\mu_T\left(\frac{\partial U}{\partial x} + \frac{\partial V}{\partial y}\right) - 2/3\rho k\right] \tag{33}$$

k Transport Equation

$$\frac{\partial \rho k}{\partial t} + \frac{\partial}{\partial x}\rho Uk + \frac{\partial}{\partial y}\rho Vk$$

$$= \rho P - \rho\varepsilon + \frac{\partial}{\partial x}\left[\left(\frac{\mu_t}{\sigma_k} + \mu\right)\frac{\partial k}{\partial x}\right] + \frac{\partial}{\partial y}\left[\left(\frac{\mu_t}{\sigma_k} + \mu\right)\frac{\partial k}{\partial y}\right] \tag{34}$$

ε Transport Equation

$$\frac{\partial \rho\varepsilon}{\partial t} + \frac{\partial}{\partial x}\rho U\varepsilon + \frac{\partial}{\partial y}\rho V\varepsilon$$

$$= c_{\varepsilon_1}\rho\frac{\varepsilon}{k}P - c_{\varepsilon_2}\frac{\varepsilon^2}{k} + \frac{\partial}{\partial x}\left[\left(\frac{\mu_t}{\sigma_\varepsilon} + \mu\right)\frac{\partial\varepsilon}{\partial x}\right] + \frac{\partial}{\partial y}\left[\left(\frac{\mu_t}{\sigma_\varepsilon} + \mu\right)\frac{\partial\varepsilon}{\partial y}\right] \tag{35}$$

where

U = streamwise mean velocity component

V = transverse mean velocity

P = pressure

k = turbulence kinetic energy

ε = turbulence kinetic energy dissipation rate

ρ = density

μ = dynamic viscosity

P = production rate of k, $\frac{\mu_t}{\rho}\left\{2\left[\left(\frac{\partial U}{\partial x}\right)^2 + \left(\frac{\partial V}{\partial x}\right)^2\right] + \left(\frac{\partial U}{\partial y} + \frac{\partial V}{\partial x}\right)^2 - \frac{2}{3}\left(\frac{\partial U}{\partial x} + \frac{\partial V}{\partial y}\right)^2\right\} - 2/3k\left(\frac{\partial U}{\partial x} + \frac{\partial V}{\partial y}\right)$

$$\mu_T \;=\; \mu_t + \mu \text{ (total viscosity)}$$

$$\mu_t \;=\; c_\mu \rho \frac{k^2}{\varepsilon} \text{ (turbulent viscosity)}$$

σ_k and σ_ε are the Prandtl numbers for k and ε, respectively, and c_{ε_1}, c_{ε_2} and c_μ are constants.

Following Ref. 12 these equations can be put in TWODLE form by defining the $\vec{U}$, $\vec{F}$, $\vec{G}$ and $\vec{H}$ vectors as

$$\frac{\partial \vec{U}}{\partial t} + \frac{\partial \vec{F}}{\partial x} + \frac{\partial \vec{G}}{\partial y} = \vec{H} \tag{36}$$

where

$$\vec{U} = \left\{ \begin{array}{l} \rho \\ \rho U \\ \rho V \\ \rho k \\ \rho \varepsilon \end{array} \right.$$

$$\vec{F} = \left\{ \begin{array}{l} \rho U \\ \rho UU + \sigma_x \\ \rho UV + \tau_{xy} \\ \rho UK + D_{k_x} \\ \rho U \;\; + D_{\varepsilon_x} \end{array} \right.$$

$$\vec{G} = \left\{ \begin{array}{l} \rho V \\ \rho UV + \tau_{yx} \\ \rho VV + \sigma_y \\ \rho Vk + D_{k_y} \\ \rho V \;\; + D_{\varepsilon_y} \end{array} \right.$$

$$\vec{H} = \left\{ \begin{array}{l} 0 \\ 0 \\ 0 \\ \rho(P - \varepsilon) \\ \rho\varepsilon/k(c_{\varepsilon_1} P - c_{\varepsilon_2}\varepsilon) \end{array} \right.$$

and

$$\sigma_x = P + 2/3\mu_T D - 2\mu_T \frac{\partial U}{\partial x} + 2/3\rho k$$

$$\tau_{xy} = \tau_{yx} = -\mu_T \left(\frac{\partial U}{\partial y} + \frac{\partial V}{\partial x}\right)$$

$$\sigma_y = P + 2/3\mu_T D - 2\mu_T \frac{\partial V}{\partial y} + 2/3\rho k$$

$$D_{k_x} = -\left(\frac{\mu_t}{\sigma_k} + \mu\right) \frac{\partial k}{\partial x}$$

$$D_{\varepsilon_x} = -\left(\frac{\mu_t}{\sigma_\varepsilon} + \mu\right) \frac{\partial \varepsilon}{\partial x}$$

$$D_{k_y} = -\left(\frac{\mu_t}{\sigma_k} + \mu\right) \frac{\partial k}{\partial y}$$

$$D_{\varepsilon_y} = -\left(\frac{\mu_t}{\sigma_\varepsilon} + \mu\right) \frac{\partial \varepsilon}{\partial y}$$

$$\mu_t = \rho c_\mu \frac{k^2}{\varepsilon}$$

$$\mu_T = \mu_t + \mu$$

$$P = \frac{\mu_t}{\rho}\left\{2\left[\left(\frac{\partial U}{\partial x}\right)^2 + \left(\frac{\partial V}{\partial y}\right)^2\right] + \left(\frac{\partial U}{\partial y} + \frac{\partial V}{\partial x}\right)^2 - \frac{2}{3}D^2\right\} - 2/3kD$$

$$\sigma_k = 3/2\,\frac{c_\mu}{c_{k_1}}$$

$$\sigma_\kappa = \frac{\kappa^2}{(c_{\varepsilon_2} - c_{\varepsilon_1})c_\mu^{1/2}}$$

$$D = \begin{cases} \dfrac{\partial U}{\partial x} + \dfrac{\partial V}{\partial y} & \text{compressible flows} \\ 0 & \text{incompressible flows} \end{cases}$$

Currently recommended values for the constants are

$c_\mu = 0.09$

$c_{k_1} = 0.22$

$c_{\varepsilon_1} = 1.44$

$c_{\varepsilon_2} = 1.92$

$K = 0.4187$

with these values σ_k and σ_ε become

$\sigma_k{}^\dagger \simeq 1.0$

$\sigma_\varepsilon \simeq 1.217$

Wall Functions

The near-wall low Reynolds number effects are incorporated to the k-ε model using the non-equilibrium wall functions of Chieng and Launder (Ref. 12). However, since TWODLE uses nodal values rather than control volume averages,[††] some changes were made in implementing these wall functions. A typical near wall region is shown in Figure 4.1. Here it is assumed that node w is at the wall, and w + 1 is in the fully turbulent region

$$\frac{y_{w+1}\, k_v{}^{\frac{1}{2}}}{\nu} > 20 \qquad (37)$$

where y_{w+1} is the distance from node w + 1 to the wall and k_v is the turbulent kinetic energy at the edge of the viscous-sublayer. The level of k_v is obtained by extrapolating the line through k_{w+1} and k_{w+2} to $y=y_v$, hence

---

[†] σ_k actually becomes 0.614, however a value of 1 is more common in the literature. There are no significant differences in the predictions obtained with these two values.

[††] Chieng and Launder wall functions use near-wall cell integration to calculate mean production and dissipation rates for those cells.

$$k_v = k_{w+1} + \frac{y_{w+1} - y_v}{y_{w+2} - y_{w+1}} (k_{w+2} - k_{w+1}) \qquad (38)$$

The thickness of the viscous sublayer, y_v, and the mean flow velocity at that location, U_v, were then calculated from

$$y_v = \nu \, Re_v / k_v^{\frac{1}{2}} \qquad (39)$$

and

$$U_v = Re_v \, (\tau_w/\rho)/k_v^{\frac{1}{2}}. \qquad (40)$$

Re_v[†] is assumed to be 20, and the wall shear stress τ_w is given by

$$\tau_w = K^* \rho \, U_{w+1} \, k_v^{\frac{1}{2}} \Big/ \left(\ln E^* \, \frac{y_{w+1} \, k_v^{\frac{1}{2}}}{\nu} \right) \qquad (41)$$

where $K^* = 0.4187 \, c_\mu^{\frac{1}{2}}$ and $E^* = e^{K^* Re_v}/Re_v$. The production rate of k at w+1 is then calculated as

$$P_{w+1} = \nu_{t_{w+1}} \left(\frac{U_{w+1} - U_v}{y_{w+1} - y_v} \right)^2 \qquad (42)$$

and the near-wall dissipation rates are expressed, following Spalding (Ref. 15) and Pope and Whitelaw (Ref. 16), respectively, as

$$\varepsilon_{w+1} = k_{w+1}^{3/2} / c_\ell y_{w+1} \qquad (43)$$

and

$$\varepsilon_w = 2 \nu \frac{k_v}{y_v^2} . \qquad (44)$$

[†] The universal viscous sublayer thickness constant, $\frac{y_v k_v^{\frac{1}{2}}}{\nu}$.

4.2 MODEL IMPLEMENTATION AND TEST CALCULATIONS

Model Implementation

The k-ε model and the associated wall functions discussed in Section 2.3.1 were implemented into the solution procedure of the code in such a way as to set up a sequential calculation of the velocity and turbulence fields. In this scheme, the density and velocity fields are obtained first. The turbulent kinetic energy equation is solved next in the same way as for the velocity field. Then the dissipation rate equation is integrated, using the latest density, velocity and turbulent kinetic energy fields. Finally, the turbulent viscosity is updated and the source and sink terms for the k and ε equations are calculated. This scheme introduces three additional subroutines to the code:

1. MUKEM: Calculates the turbulent viscosity from its definition, $\mu_t \equiv c_\mu \rho k^2/\varepsilon$
2. PRODK: Calculates the production rate of turbulent kinetic energy,
$$P \equiv -\mu_t/\rho\left(\frac{\partial U_i}{\partial x_j}\right)^2$$
3. SOURCE: Calculates the source-sink terms for the k and ε transport equations, $\rho(P-\varepsilon)$ and $\rho\,\varepsilon/k\,(c_{\varepsilon_1}P - c_{\varepsilon_2}\varepsilon)$, respectively.

The solution procedure thus becomes

CALL INTEG	(ISS=1)	Solve for velocity and density fields
CALL INTEG	(ISS=2)	Solve for k field
CALL INTEG	(ISS=3)	Solve for ε field
CALL MUKEM		Calculate μ_t
CALL PRODK		Calculate P
CALL SOURCE		Calculate $\rho(P-\varepsilon)$ and $\rho\,\varepsilon/k\,(c_{\varepsilon_1}P - c_{\varepsilon_2}\varepsilon)$

Advance the time and repeat.

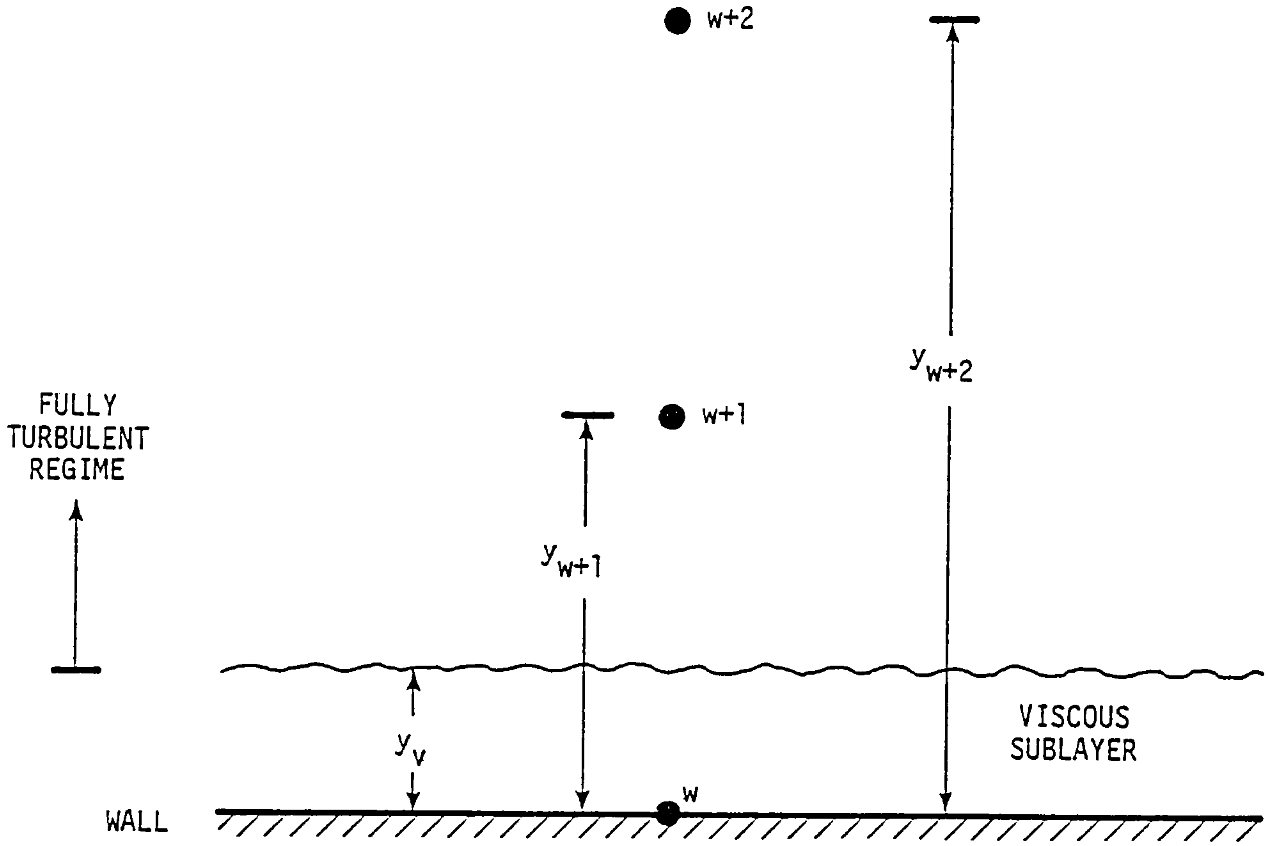

FIGURE 4.1. Typical Near-Wall Region.

There are, of course, many variations within any given scheme that can be tried to improve stability and/or numerical efficiency. This particular scheme was chosen for its proven stability characteristics in elliptic flow calculations with other computational techniques. The flow chart of the TWODLE code with the k-ε model is given in Figure 4.2.

Test Calculations

Initial testing entailed assessing the compatibility and the logic of the changes to the code with and without the k-ε model. The first step was to reproduce, with one of the existing algebraic viscosity models, previous predictions of the Mach 5 10^0 compression corner test case. Upon completion of this task, detailed assessments of the k-ε model in this application were to be undertaken. Preliminary calculations of the Mach 5 10^0 compression corner test case with this model showed severe stability problems. To track down the cause of the problem, it was decided to simplify the flow geometry further, to a Mach 5 flow between two parallel plates, and specifying a uniform grid by bypassing the coordinate transformation. This geometry represents possibly the simplest internal flow test case that still contains the features needed to evaluate the k-ε model. The use of a uniform grid eliminates any potential problems due to coordinate transformation and also simplifies the computation of the source-sink terms. Calculations of this geometry were done in stages to isolate and identify the source of the stability problems. The k and ε transport equations can be written in the following general form

$$\underbrace{\frac{\partial \rho\phi}{\partial t}}_{I} + \underbrace{\rho U \frac{\partial \phi}{\partial x} + \rho V \frac{\partial \phi}{\partial y}}_{II} = \underbrace{D_\phi}_{III} + \underbrace{S_\phi}_{IV} \tag{45}$$

where $\phi \equiv k \text{ or } \varepsilon$

$$D_\phi \equiv \left\{ \begin{array}{l} D_k = \frac{\partial}{\partial x}\left\{\left(\frac{\mu_t}{\sigma_k} + \mu\right)\frac{\partial k}{\partial x}\right\} + \frac{\partial}{\partial y}\left\{\left(\frac{\mu_t}{\sigma_k} + \mu\right)\frac{\partial k}{\partial y}\right\} \\ D_\varepsilon = \frac{\partial}{\partial x}\left\{\left(\frac{\mu_t}{\sigma_\varepsilon} + \mu\right)\frac{\partial \varepsilon}{\partial x}\right\} + \frac{\partial}{\partial y}\left\{\left(\frac{\mu_t}{\sigma_\varepsilon} + \mu\right)\frac{\partial \varepsilon}{\partial y}\right\} \end{array} \right.$$

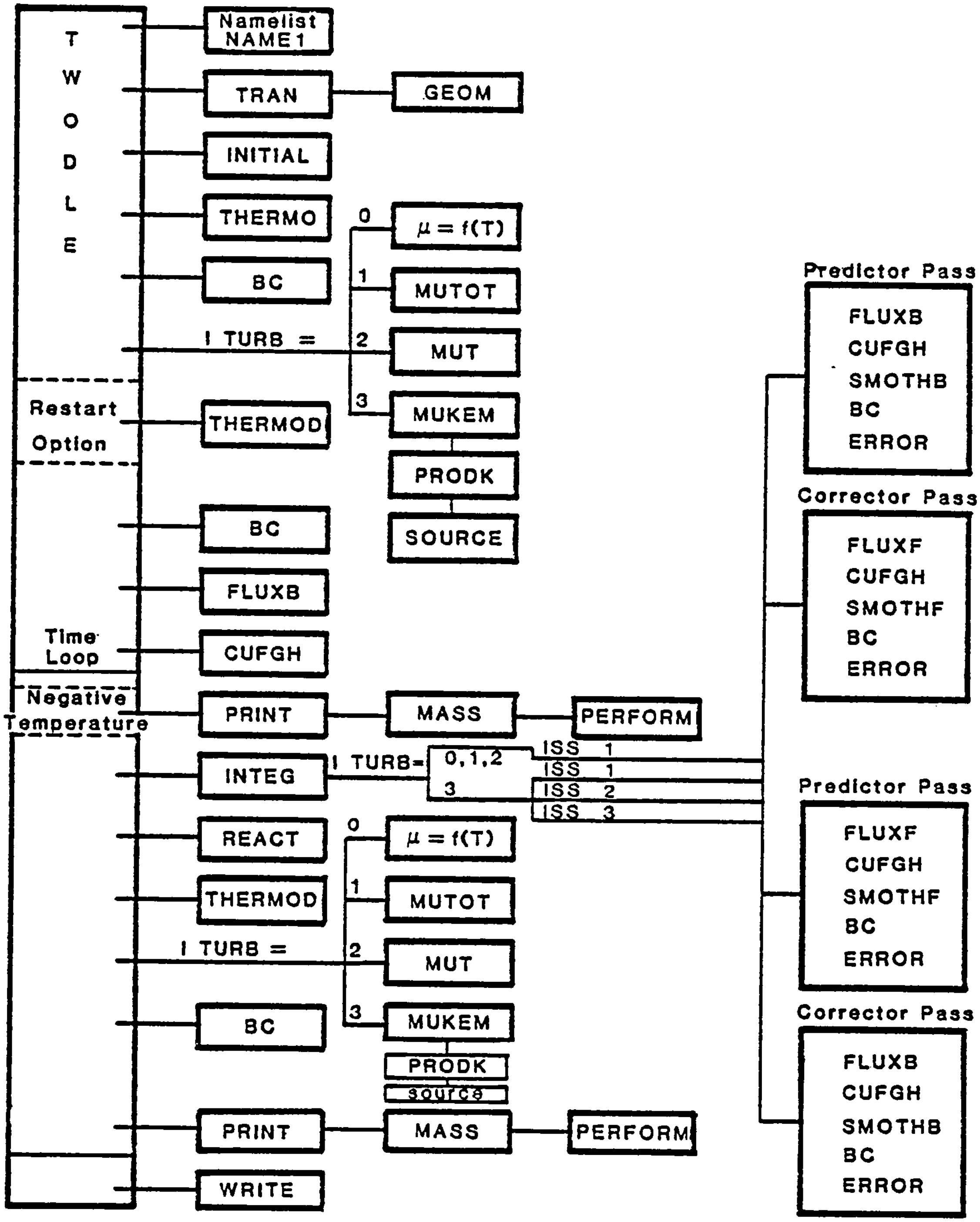

FIGURE 4.2 TWODLE Flow Chart.

$$P \equiv \begin{cases} \dfrac{\mu_t}{\rho} \left\{ 2\left[\left(\dfrac{\partial U}{\partial x}\right)^2 + \left(\dfrac{\partial V}{\partial y}\right)^2 \right] + \left(\dfrac{\partial U}{\partial y} + \dfrac{\partial V}{\partial x}\right)^2 - \right. \\ \left. \dfrac{2}{3} \left(\dfrac{\partial U}{\partial x} + \dfrac{\partial V}{\partial y}\right)^2 \right\} - \dfrac{2}{3} k \left(\dfrac{\partial U}{\partial x} + \dfrac{\partial V}{\partial y}\right) \end{cases}$$

$$S_\phi \equiv \begin{cases} S_k = (P-\varepsilon) \\ S_\varepsilon = \rho\varepsilon/k \, (c_{\varepsilon_1} P - c_{\varepsilon_2} \varepsilon) \end{cases}$$

$$\mu_t \equiv c_\mu \, \rho \, \frac{k^2}{\varepsilon}$$

Numerically, the transient, I, convective, II, and diffusive transport, III, terms are stabilizing in nature, whereas the source terms, IV, especially when stiff, can cause stability problems. The first step in the investigation was to set the source terms identically to zero and carry out the calculations with only the transient, and convective and diffusive transport terms activated. These calculations produced stable results for this initial/boundary value problem. The next step involved predictions with the complete transport equations for k and ε except that the production term, P, in the source terms was set to zero. These results also proved to be stable. The final test was calculations with the complete k and ε transport equations. These calculations, however, experienced stability problems almost immediately, leading to negative k and ε values and to eventual collapse of the solution scheme within 120 time steps. This clearly shows the adverse effects of the stiff source terms on the solution scheme. Changes in the wall boundary treatments, and variations in the relative order of calculations of the source terms within the solution scheme failed to improve the outcome.

These results, combined with previous experience, indicate severe stability problems in the solution of source-dominated (stiff) transport equations with both time-split and time-unsplit MacCormack predictor-corrector algorithms. This is a serious problem since most advanced turbulence (k-ε and higher-order closure schemes) and combustion kinetics models inherently contain stiff partial differential equations. The efforts in this respect described in this report were directed to investigate and devise stable implementation techniques for the k-ε model and its boundary conditions within the given solution scheme of the code. In other words, the goal was to tailor the model to fit the code. These efforts have failed due the inability of the solution algorithm to negotiate, in any direct way, the effects of the stiff source terms in the k and ε (or in any other source dominated) transport equations. Other researchers have also encountered similar stability problems with MacCormack predictor-corrector type block solution algorithms. These findings support the results described in Ref. 2, in which a compromise scheme that solves for the mean flow and the density fields with the MacCormack technique, and then evaluates the k and ε equations explicitly was recommended. Overall, this study raises two fundamental questions. One is the apparent lack of versatility of this widely used computational technique which seems to be severly restricted in its applicability to advanced turbulent fluid flow analysis. The second question is the relative merits of the current practice of separating the development of physical models from research in numerical analysis as opposed to a unified approach that closely coordinates developments in computational techniques with the advances in physical models to ensure compatibility in their eventual application to scientific and engineering problems.

5.0. ASSESSMENT OF MODELS FOR TURBULENT SCALAR TRANSPORT

Transport of a scalar mean quantity C (heat, species, etc) is described by the equation

$$\frac{\partial \rho C}{\partial t} + \rho U_i \frac{\partial C}{\partial x_i} = \frac{\partial}{\partial x_i}\left(\gamma \frac{\partial C}{\partial x_i} - \rho\overline{u_i c}\right) \qquad (46)$$

where U_i is the mean flow velocity, ρ is the density, γ is a molecular transport coefficient, and $\overline{u_i c}$ is the scalar flux correlation which is the turbulent scalar transport counterpart of the $\overline{u_i u_j}$ correlation of the momentum equations. Closure of the above equation requires either solution of a transport equation for $\overline{u_i c}$ or the modeling of this quantity in terms of known or calculable variables.

5.1. CLOSURE OF THE SCALAR TRANSPORT EQUATION

A transport equation for the scalar flux $\overline{u_i c}$ can be derived by multiplying the equation for the instantaneous value of the scalar $\tilde{C}$ (=C+c) by U_i and adding it to the x_i-component of the Navier-Stokes equations multiplied by c. Upon ensemble averaging, the results may be expressed as

$$\frac{D}{Dt}\overline{u_i c} = -\left\{ \overline{u_i u_j}\,\frac{\partial C}{\partial x_j} + \overline{u_j c}\,\frac{\partial U_i}{\partial x_j} \right\} + \frac{\overline{\rho' c}}{\rho} g_i$$

I.
Convective
Transport

II.
Generation of the
combined action of
mean velocity and
mean scalar gradients.

III.
Generation by
buoyant forces

$$- (\gamma+\nu)\,\overline{\frac{\partial c}{\partial x_j}\,\frac{\partial U_i}{\partial x_j}} \qquad + \qquad \overline{\frac{p}{\rho}\,\frac{\partial c}{\partial x_j}}$$

IV.
Dissipation

V.
Pressure-scalar-gradient
correlation

$$- \frac{\partial}{\partial x_j} \left(\overline{u_i u_j c} + \frac{\overline{pc}}{\rho} \delta_{ij} \right)$$

VI.
Diffusion Transport

(47)

This equation is valid for incompressible flows and where gradients in C are small enough for γ'/γ and ν'/ν to be entirely unimportant (γ' and ν' being the fluctuating parts of γ and ν) and for ρ'/ρ to be significant only in the gravitational term. The first and the second terms in this equation are exact and require no modeling. The buoyant generation term, III, is conveniently modified as follows

$$\frac{\overline{\rho' c}}{\rho} g_i = - \alpha \frac{\overline{c^2}}{C} g_i \tag{48}$$

where the dimensionless coefficient α is defined as*

$$\alpha \equiv - \left. \frac{\partial \rho}{\partial C} \right|_p \frac{C}{\rho}$$

The dissipation term, IV, is zero in isotropic turbulence and is negligible in non-isotropic turbulence provided that the turbulence Reynolds number is high. The pressure-scalar-gradient correlation, V, is the counterpart of the pressure-strain correlation in the stress equations. With direct dissipation negligible, this provides the mechanism which limits the growth of fluxes. Finally, term VI denotes the rate of spatial transport of $\overline{u_i c}$ due to velocity and pressure fluctuations. This level of closure corresponds to a full Reynolds stress formulation for momentum transport and requires modeling of the pressure-scalar-gradient correlation, V, and spatial transport, IV, terms. Modeling of these terms are discussed in some detail in Refs. 17 and 18.

---

* If C stands for temperature and the fluid is an ideal gas, α is unity.

Solution of transport equations for scalar flux components is both conceptually possible and economically feasible for most flowfields. Similar levels of closure however also exist and are widely used in computational work. These are discussed next.

5.2. ALGEBRAIC STRESS MODELS FOR SCALAR TRANSPORT

These schemes, the counterpart of the hydrodynamic algebraic stress models, employ algebraic stress modeling rather than a complete differential closure of equation (47). These models for the scalar fluxes, given here for the temperature field, generally have the following form (Ref. 18)

$$-\overline{u_iT'} = \Phi_T \frac{k}{\varepsilon}\overline{u_iu_k}\frac{\partial T}{\partial x_k} - \Phi'_T \frac{k}{\varepsilon} P_{i_T} \qquad (49)$$

where

$$\Phi_T \equiv \left[c_{1_T} + \tfrac{1}{2}(P/\varepsilon - 1) + \tfrac{1}{2}\, k/\varepsilon \frac{\varepsilon_T}{\overline{T'^2}} (P_T/\varepsilon_T - 1)\right]^{-1}$$

$$\Phi'_T \equiv \Phi_T (1 - c_{2_T})$$

$$P_{i_T} \equiv -\left\{ \overline{u_kT'} \frac{\partial U_i}{\partial x_k} + \frac{\alpha g_i}{T} \overline{T'^2} \right\} \sim \text{production rate of } \overline{u_iT'}$$

$$P_T \equiv -2\,\overline{u_kT'} \frac{\partial T}{\partial x_k} \quad \sim \text{production rate of } \overline{T'^2}$$

$$\varepsilon_T \equiv 2\gamma\, \overline{\left(\frac{\partial T'}{\partial x_k}\right)\left(\frac{\partial T'}{\partial x_k}\right)} \quad \sim \text{dissipation rate of } \overline{T'^2}$$

This form of the model requires solution of transport equations for $\overline{T'^2}$ and ε_T which can be derived in a similar fashion to the k and ε equations (Ref. 1). Further simplifications however are possible by relating ε_T to ε, k and $\overline{T'^2}$ by

$$\varepsilon_T = \frac{2}{c_T'}\, \varepsilon/k\, \overline{T'^2} \qquad (50)$$

and approximating $\overline{T'^2}$, when the dissipation and production rates of $\overline{T'^2}$ are nearly in balance, as

$$\overline{T'^2} = - c_T' \frac{k}{\varepsilon} \overline{u_k T'} \frac{\partial T}{\partial x_k} \tag{51}$$

The recommended values for the model constants c_{1_T}, c_{2_T} and c_T' are 3.2, 0.50, and 1.6, respectively. This model, first proposed 7 years ago, has yet to be tested in recirculating flows. Free shear flow predictions with this model (Ref. 18) however, exhibit the correct behavior of progressive collapse for horizontal buoyant mixing layers and surface jets as the mean Richardson number increases, and also show reasonably good agreement with published turbulent wake and plane jet thermal data. These models are yet to be applied to recirculating flow calculations. Further model development, refinement and testing is needed to explore the full potential of this level of closure.

5.3. GRADIENT DIFFUSION MODELS

These simpler models relate the scalar fluxes to the hydrodynamic turbulence properties and the mean scalar gradient

$$- \overline{u_i c} \propto \overline{u_i u_j} \frac{k}{\varepsilon} \frac{\partial C}{\partial x_j} \tag{52}$$

or in terms of an effective turbulent Prandtl number, G_t

$$- \overline{u_i c} = \frac{\nu_t}{G_t} \frac{\partial C}{\partial x_i} \tag{53}$$

where $\nu_t \equiv c_\mu k^2/\varepsilon$. This is the scalar-transport model that nearly all practical calculation schemes have adopted to date. Experiments suggest G_t is approximately two-thirds in many free shear flows but is some 50% higher in the vicinity of a wall. The biggest drawback of this model is that it is based, like the k-ε model, on an isotropic turbulent transport coefficient concept and thus is theoretically limited to free shear flow and some boundary layer calculations.

6.0 SUMMARY: TURBULENCE MODELS FOR SCRAMJET FLOWFIELDS

The overall objective of the work described in Refs. 1 and 2 and in this report has been to establish appropriate turbulence models to use in computations of scramjet flowfields. These combustors involve three-dimensional reacting flows with embedded recirculation regions, and the fuel-air mixing rate is critical to the overall performance of the combustor. Thus to be usable in design evaluation and data interpretation, turbulence models must be reasonably accurate over a broad range of conditions.

Based on the work reported in Refs. 1 and 2 and in this report, the recommended turbulence modeling approach for use in scramjet calculations is the algebraic Reynolds stress model. In regions of strong streamline curvature, this model should be used with the dissipation equation modification described in Ref. 2 which were designed to improve the sensitivity of the model to these effects. The algebraic Reynolds stress approach is particularly valuable where multiple stress components are important, such as in three-dimensional flows, since the basic two-equation k-ε model involves an assumption of effective viscosity isotropy that is not borne out by experimental results. Where only a single stress component is non-negligible, the two-equation approach provides good results, Since the algebraic Reynolds stress formulation involves the solution of the turbulent kinetic energy and dissipation rate equations, it is easily arranged to allow the algebraic stress formulations to relax to a two-equation model as the different stress components become negligible in a given calculation.

This work has also indicated the extreme importance of considering the interaction of the turbulence model and the numerical solution procedure as key parts of the development of scramjet combustor models. The interaction takes two forms: compatibility of the turbulence model and the solution procedure, and the interaction of the model-predicted diffusion with that generated artificially by the solution procedure itself. Compatibility issues arise because the models recommended in this study involves the solution of source-dominated, "stiff" transport equations. The numerical solution procedure must be able to accept stiff equations to be compatible with these models. Numerical diffusion is a feature of most numerical solution procedures and under some circumstances it can dominate the diffusion predicted by the turbulence model. This must be avoided by careful attention to grid size and location. Finally, establishment of the proper initial and wall boundary conditions is critical to proper use of turbulence models. This has been emphasized throughout this work, and the techniques reported herein and in Refs. 1 and 2 for establishing initial and boundary conditions are recommended for future scramjet modeling work.

7.0. CONCLUSIONS AND RECOMMENDATIONS

The conclusions reached as a result of the work outlined in this report can be summarized as follows:

7.1. SUBSONIC AXISYMMETRIC RECIRCULATING FLOWS

1. For diameter ratios of 2:1 and 3:1, in axisymmetric flows, mean velocity and turbulence field predictions do not change significantly with different turbulence models. This can be ascribed to the dominance of pressure forces over turbulence diffusion in these flowfields.
2. Axisymmetric sudden expansion flowfield predictions are especially sensitive to grid refinement. The numerical diffusion inherent in a coarse grid can produce effects on the predicted overall mixing process which are larger than those produced by variations in turbulence models.
3. The algebraic stress model produces results in axisymmetric flows at low diameter ratios (where pressure effects are reduced) which are consistent with its performance in planar backward-facing step flows. Thus the ASM with modifications introduced to increase the model's sensitivity to streamline curvature can be recommended in regions where strong recirculations exist, and the unmodified ASM in other regions.

7.2. SUBSONIC SWIRLING FLOWS

1. Although of little direct interest in scramjet applications, swirling flows at large swirl numbers are stringent tests of modeling: large differences between k-ϵ model and ASM model predictions are evident. This is due to the strong anisotropy of the stress components in swirling flows, which

is not adequately accounted for by the effective viscosity assumptions inherent in the k-ε model.

2. Comparison of model predictions with experimental results for strongly swirling flow could provide the means to further develop and improve the ASM model. Appropriate experimental data is not now available. The ability of the ASM to handle strongly nonisotropic flowfields is of potential value in the modeling of 3D flows in scramjet combustors, even in the absence of swirl.

7.3 SUPERSONIC RECIRCULATING FLOWS

1. Efforts, described in this report, to devise stable techniques for the implementation of the k-ε model and its boundary conditions in both the time-split and time-unsplit MacCormack predictor-corrector algorithms were unsuccessful. This result is apparently caused by the inability of the solution algorithm to negotiate, in any direct way, the effects of stiff source terms in the k and ε transport equations.

2. A more detailed study is needed to identify the required changes in the MacCormack solution scheme that will eliminate the drawbacks identified in this work. The present work raises fundamental questions with respect to the merits of separating the development of physical flowfield models from research in numerical analysis. Coordination is required to ensure that numerical schemes and physical models are ultimately compatible.

7.4. MODELING OF TURBULENT SCALAR TRANSPORT

1. Solution of the transport equations for scalar flux components is both conceptually possible and economically feasible. Schemes that employ the algebraic stress closure rather than a complete differential closure are appealing

in terms of consistency with the level of closure chosen for the hydrodynamic field.

2. Further work is required to assess the potential of algebraic scalar flux modeling in more complicated flowfields such as recirculating sudden-expansion flows.

REFERENCES

1. Fabris, G.; Harsha, P.T.; and Edelman, R.B.: Multiple-Scale Turbulence Modeling of Boundary Layer Flows for Scramjet Applications. NASA Contractor Report 3433, May 1981.

2. Sindir, M.M.; and Harsha, P.T.: Assessment of Turbulence Models for Scramjet Flowfields. NASA Contractor Report 3643, November 1982.

3. Chaturvedi, M.C.: Flow Characteristics of Axisymmetric Expansion, Journal of the Hydraulics Division, Proc. ASCE, vol. 39, no. HY3, May 1963, pp. 61-92.

4. Back, L.J.; and Roschke, E.J.: Shear-Layer Flow Regimes and Wave Instabilities and Reattachment Lengths Downstream of an Abrupt Circular Channel Expansion. J. Applied Mechanics, September 1972, pp. 677-681.

5. Sturgess, G.J.; and Syed, S.A.: Multi-Specie Isothermal Flow Calculations of Widely-Spaced Co-Axial Jets in a Confined Sudden Expansion, with the Central Jet Dominant. AIAA Paper 82-1156, Presented at the 18th Joint Propulsion Conference, June 21-23, 1982, Cleveland, Ohio.

6. Zemanick, P.P.; and Dougall, R.S.: Local Heat Transfer Downstream of Abrupt Circular Channel Expansion. ASME Journal of Heat Transfer, vol. 92, 1970, pp. 53-60.

7. Krall, K.M.; and Sparrow, E.M.: Turbulent Heat Transfer in the Separated Reattached and Redevelopment Regions of a Circular Tube. ASME Journal of Heat Transfer, vol. 83C, 1961, p. 131.

8. Runchal, A.K.: Mass Transfer Investigation in Turublent Flow Downstream of Sudden Enlangement of a Circular Pipe for Very High Schmidt Numbers. International Journal of Heat and Mass Transfer, vol. 14, 1971, pp. 781-792.

9. Sindir, M.M.: Numerical Study of Turbulent Flows in Backward-Facing Step Geometries: Comparison of Four Models of Turbulence. Ph.D. Thesis, University of California-Davis, June 1982.

10. Patankar, S.V.: Numerical Heat Transfer and Fluid Flow. McGraw-Hill, 1980.

11. Drewry, J.E.: Fluid Dynamic Characterization of Sudden-Expansion Ramjet Combustor Flowfields. AIAA Journal, vol. 16, no. 4, April 1978, pp. 313-319.

12. Chieng, C.C.; and Launder, B.E.: On the Calculation of Turbulent Heat Transport Downstream of an Abrupt Pipe Expansion. Numerical Heat Transfer, vol. 3, 1980, p. 189.

13. Edelman, R.B.; and Harsha, P.T.: Laminar and Turbulent Gas Dynamics in Combustors - Current Status. Prog. Energy Combust. Sci., vol. 4, 1978, pp. 1-62.

14. Drummond, J.P.; and Weidner, E.H.: Numerical Study of a Scramjet Engine Flowfield. AIAA Paper 81-0186, AIAA 19th Aerospace Sciences Meeting, January 1981.

15. Spalding, D.B.: Heat Transfer from Turbulent Separated Flow. J. Fluid Mechanics, vol. 27, 1967, pp. 97-109.

16. Pope, S.B.; and Whitelaw, J.H.: The Calculation of Near-Wake Flows. J. Fluid Mechanics, vol. 73, 1976, pp. 9-30.

17. Gibson, M.M.; and Launder, B.E.: On the Calculation of Horizontal Turbulent Free Shear Layer Flows Under Gravitational Influence. J. Heat Transfer, vol. 98C, 1976, pp. 81-87.

18. Bradshaw, P. (ed.): Turbulence - Topics in Applied Physics, 12, Springer-Verlag, 1978, pp. 231-287.

1. Report No.
NASA CR-172284

2. Government Accession No.

3. Recipient's Catalog No.

4. Title and Subtitle
Turbulent Transport Models
for Scramjet Flowfields

5. Report Date
February 1984

6. Performing Organization Code

7. Author(s)
M. M. Sindir and P. T. Harsha

8. Performing Organization Report No.

9. Performing Organization Name and Address
Science Applications, Inc.
Combustion Science and Advanced Technology Dept.
9760 Owensmouth Avenue
Chatsworth, California 91311

10. Work Unit No.

11. Contract or Grant No.
NASI-15988

12. Sponsoring Agency Name and Address
National Aeronautics and Space Administration
Washington, D.C. 20546

13. Type of Report and Period Covered
Contractor Report

14. Sponsoring Agency Code

15. Supplementary Notes
Langley Technical Monitor:
Final Report

16. Abstract

Turbulence modeling approaches were examined from the standpoint of their capability to predict the complex flowfield features observed in scramjet combustions. Thus, for example, the accuracy of each turbulence model, with respect to the prediction of recirculating flows, was examined. It was observed that for large diameter ratio axisymmetric sudden expansion flows, a choice of turbulence model was not critical because of the domination of their flowfields by pressure forces. For low diameter ratio axisymmetric sudden expansions and planar backward-facing step flows, where turbulent shear stresses are of greater significance, the algebraic Reynolds stress approach, modified to increase its sensitivity to streamline curvature, was found to provide the best results. Result of the study also showed that strongly swirling flows provide a stringent test of turbulence model assumptions. Thus, although flows with very high swirl are not of great practical interest, they are useful for turbulence model development. Finally, it was also noted that numerical flowfields solution techniques have a strong interrelation with turbulence models, particularly with the turbulent transport models which involve source-dominated transport equations. Numerical solution procedures must be capable of handling such transport equations if they are to be used for the prediction of turbulent flows.

17. Key Words (Suggested by Author(s))
Turbulence Modeling
Turbulent Mixing
Recirculating Flow
Swirling Flow
Numerical Solution Procedures

18. Distribution Statement
UNCLASSIFIED - UNLIMITED

19. Security Classif. (of this report)
UNCLASSIFIED

20. Security Classif. (of this page)
UNCLASSIFIED

21. No. of Pages
86 + v

22. Price

N-305

For sale by the National Technical Information Service, Springfield, Virginia 22161